Energy & Environmental Science

ROYAL SOCIETY OF CHEMISTRY

REVIEW

View Article Online
View Journal | View Issue

Cite this: *Energy Environ. Sci.*, 2025, **18**, 2050

Corrosion of metallic anodes in aqueous batteries

Xuejin Li,†*[a] Pengyun Liu,†[a] Cuiping Han,[b] Tonghui Cai,[a] Yongpeng Cui,[a] Wei Xing*[a] and Chunyi Zhi*[c]

Received 6th January 2025,
Accepted 28th January 2025

DOI: 10.1039/d5ee00075k

rsc.li/ees

Aqueous metal batteries offer high energy density and excellent compatibility with various cathode materials, and hence, they are attracting significant attention. However, the corrosion of metallic anodes seriously deteriorates the battery performance in terms of capacity loss, retarded reaction kinetics, and shortened cycling life. In this review, the fundamental corrosion mechanisms of metallic anodes in aqueous electrolytes and the key influencing factors are comprehensively discussed and summarized. Subsequently, recent achievements in corrosion inhibition are summarized and categorized to evaluate the advantages and disadvantages of various strategies. Furthermore, advanced characterization techniques used in corrosion mechanism analyses and protection assessments are elucidated. Finally, the current challenges in addressing the corrosion issue and potential developments in this field are presented.

Broader context

Metallic anodes, including Zn, Al, and Mg, are widely applied in aqueous batteries owing to their high energy density and excellent compatibility with various cathode materials. However, they typically suffer from severe corrosion in aqueous electrolytes, and their corrosion behaviors are complicated. Corrosion processes of metallic anodes are of different types owing to their various properties. Even for the same metal, the corrosion behaviors are distinct in different environments and can be affected by pH, electrolyte ions, and dissolved oxygen concentration. Understanding the corrosion mechanisms of metallic anodes in various electrolyte environments is crucial in achieving effective corrosion inhibition methods and obtaining the desired battery performance. Currently, almost no review has specifically addressed, analyzed, or summarized the corrosion issue of metallic anodes in aqueous metal batteries (AMBs). Presenting a review in this research frontier is very necessary to provide insights on recent advances and potential guidance for improving the overall performance of AMBs. This review comprehensively introduced the corrosion behaviors of various metallic anodes, a variety of corrosion prevention tactics, and sophisticated characterization methods. We also discussed the challenges and future perspectives of this field to offer insights into further development of AMBs.

1. Introduction

Aqueous metal batteries (AMBs), which directly adopt metals as anodes (such as Zn, Al, and Mg), exhibit superior advantages not only in the field of large-scale energy storage but also in wearable and biocompatible applications.[1,2] Electrochemistry on the anodic side is based on the reversible deposition-dissolution of metals (Fig. 1a). The employment of metallic anodes endow AMBs with higher energy densities than "rocking chair"-type metal-ion batteries that store metal ions in anode hosts.[3,4] In addition, metallic anodes provide more choices for matching cathode materials, such as air electrodes and sulfur electrodes, that have higher theoretical capacity than intercalation-type cathode materials.[5,6] However, they typically suffer from serious corrosion issues in aqueous electrolytes, which are normally accompanied by the production of hydrogen and inert corrosion products, resulting in capacity deterioration and unsatisfied lifespan.[7,8]

Electrochemical corrosion of metal is a redox reaction (Fig. 1b) and can be expressed by the following equation:

$$M + nY \rightarrow M^{n+} + nY^{-} \quad (1.1)$$

where M represents the anodic metal, Y is the cathodic reactant, and n is the electron transfer number during the corrosion process. On the anodic side metals are oxidized, while cathodic reactions vary in different battery systems. Reactants of cathodic reactions generally include cations (such as H^+, Cu^{2+} or Fe^{3+}), anions ($S_2O_8^{2-}$, NO_3^-, *etc.*), neutral molecules (O_2, Cl_2,

[a] State Key Laboratory of Heavy Oil Processing, Shandong Key Laboratory of Intelligent Energy Materials, School of Materials Science and Engineering, China University of Petroleum, Qingdao 266580, China. E-mail: lxjupc@upc.edu.cn, xingwei@upc.edu.cn
[b] Faculty of Materials Science and Energy Engineering/Institute of Technology for Carbon Neutrality, Shenzhen Institute of Advanced Technology, Chinese Academy of Sciences, Shenzhen, 518055, China
[c] Department of Materials Science and Engineering, City University of Hong Kong, Hong Kong 999077, P. R. China. E-mail: cy.zhi@cityu.edu.hk
† Xuejin Li and Pengyun Liu contribute equally to this review.

etc.), and some organic compounds.[9,10] Among these cathodic reactions, hydrogen evolution reaction (HER) and oxygen reduction reaction (ORR) are the most common parasitic reactions in AMBs. These reaction processes in different battery systems will be introduced in the following section.

The above-mentioned redox reactions are irreversible and result in continuous metal dissolution. Even worse, the energy produced *via* these process cannot be utilized for the battery.[11,12] Another problem is that the corrosion products, such as inert metal oxides/hydroxides and H_2, are critically detrimental to battery performance, resulting in capacity loss, retarded reaction kinetics, and short lifespan.[13] Moreover, the HER and ORR will fatally increase the pH of the electrolyte, which in turn may negatively influence the battery performance.

According to the corrosion morphology, corrosion can be divided into general corrosion and localized corrosion. General corrosion suggests that the corrosion proceeds in a relatively uniform manner over the entire surface of metal anodes (Fig. 1c). Damage to metals caused by general corrosion is unitary, and the derivative harm to metal is unlikely. However, in most cases, metallic anodes suffer from severe localized corrosion, which is more intense in some specific regions than in an adjacent area.[8,14,15] When active species in electrolytes, such as Cl^-, dissolved oxygen, or some oxidants, are selectively absorbed on the defective area of metals, corrosion on the area is more likely to happen and form the pitting nucleus. Under suitable potential, pitting corrosion is accelerated due to the enrichment of active species in the pits and develops to the inner side of metals (Fig. 1d). Corrosions are promoted in the pits due to the formation of oxygen-concentration cells and occluded cells. Corrosion may also occur along the grain boundaries because of the uneven electrochemical properties between grain crystals and grain boundaries (Fig. 1e). The boundaries have more defects and aggressive anions prefer to absorb on these regions, leading to more serious corrosion. If metallic impurities exist in the metal anode, a galvanic-type corrosion cell will be formed, and this results in galvanic corrosion of metals at the metal/impurities interface (Fig. 1f). It is demonstrated that the surface potentials between matrix metals and impurities or boundaries are different (Fig. 1e and f),[16,17] which will facilitate the corrosion at interfaces.

Xuejin Li

Xuejin Li is currently an Associate Professor in the Department of Materials Chemistry at the China University of Petroleum (East China). He received his PhD degree from the China University of Petroleum under the co-supervision of Prof. Zifeng Yan and Prof. Wei Xing. He then moved to the Institute of Physics-SongShan Lake Materials Laboratory as a Postdoctoral Fellow. His research interests focus on aqueous electrolyte batteries and hydrogen oxidation reaction electrocatalysis.

Pengyun Liu

Pengyun Liu is currently an Associate Professor in the Department of Materials Chemistry at the China University of Petroleum (East China). She received her PhD degree from the Curtin University under the co-supervision of Prof. Zongping Shao and Prof. Moses Tade. Her current research interests mainly focus on perovskite materials and devices, including perovskite photovoltaic devices and photo-rechargeable energy storage devices.

Wei Xing

Wei Xing received his PhD in chemical engineering from the China University of Petroleum in 2005 under the co-supervision of Prof. Zifeng Yan and Prof. G. Q. Max Lu. After seven years of research and teaching in Shandong University of Technology, he joined the China University of Petroleum as a Full Professor from December 2012. His research interests cover porous materials for energy storage, CO_2 capture, and heterogeneous catalysis.

Chunyi Zhi

Chunyi Zhi is currently a Professor in the Department of Materials Science and Engineering at the City University of Hong Kong. He received his PhD degree in Physics from the Institute of Physics, Chinese Academy of Sciences. He then moved to the National Institute for Materials Science (NIMS) in Japan as a Postdoctoral fellow, and he later became an ICYS Research Fellow, Researcher (faculty) and Senior Researcher (permanent). His research focuses on wearable/flexible energy storage devices and aqueous electrolyte batteries.

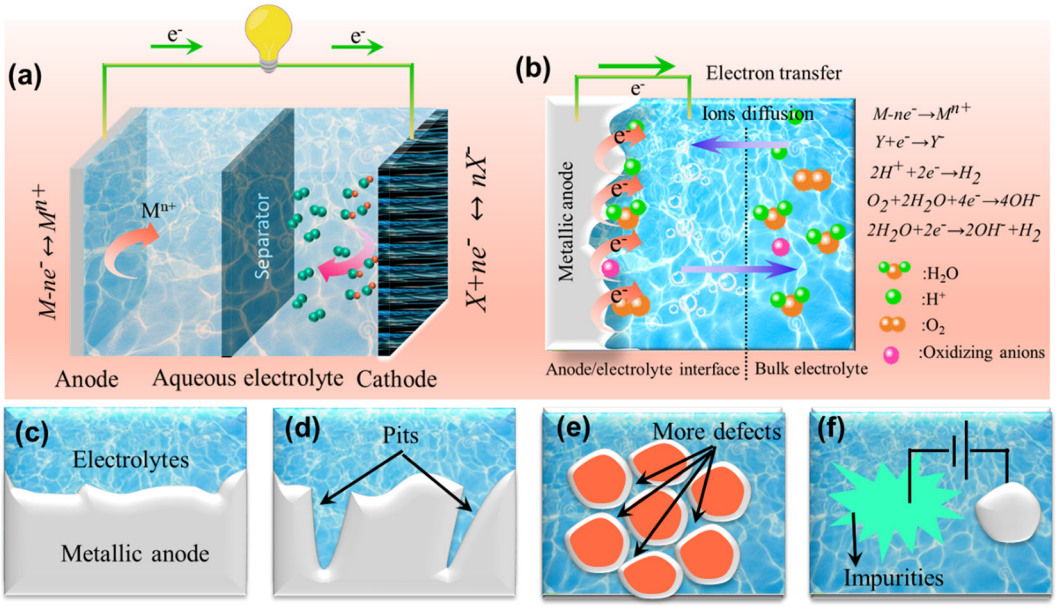

Fig. 1 (a) Illustration of the metal battery configuration in aqueous electrolytes; (b) illustration of metal corrosion in aqueous electrolytes; illustrations of (c) general corrosion, (d) pitting corrosion, (e) intergranular corrosion or crevice corrosion, and (f) galvanic corrosion with corresponding morphologies or potential demonstrations.

Damages to the metal electrode by localized corrosion are more serious than those that appear outwardly. Apart from the mass loss of metals, the current distribution on the metallic anode will be apparently affected by localized corrosion, resulting in uneven deposition and dissolution of metal during the charge–discharge process.[18] To this end, the corrosion inhibition of metallic anodes in aqueous electrolytes is particularly important for improving the efficiency and lifespan of AMBs.

Metallic anodes including Zn, Al, and Mg are widely applied in aqueous metal–air batteries, which typically select alkaline electrolytes. The self-corrosion issue of these anodes has recently gained great interest from industry and researchers. Strategies such as using corrosion inhibitors and protective coating on anodes have been proposed to solve the corrosion issue in metal–air batteries.[19–22] Compared with the process in metal–air batteries, less information is available on corrosion issues in other types of AMBs, which still requires great efforts in this intriguing area. Corrosion processes of metallic anodes are different due to their various properties. Even for the same metal, the corrosion behaviors are distinct under different environments and can be affected by pH, electrolyte ions, and dissolved oxygen concentration. Understanding the corrosion mechanisms of metallic anodes in various electrolyte environments is crucial in achieving effective corrosion inhibition methods and obtaining the desired battery performance.

Currently, almost no review has specifically addressed, analyzed, or summarized the corrosion issue of metallic anodes in AMBs. Although several reviews related to Zn anodes have been reported, they mainly focus on Zn dendrite issues.[3,23–25] A recent review related to Zn anode corrosion has been reported, which briefly introduced the corrosion mechanism, corrosion inhibition, and methods for Zn corrosion analyses.[26] However, the study and discussion of other metal anodes such as Al, Mg, and Fe are not included in this publication. The corrosion reaction process of metal anodes is complicated and variable in a complex electrochemical reaction environment, and an accurate understanding of the corrosion mechanism is still lacking. Presenting a review in this research frontier is very necessary to provide recent advances and potential guidance for improving the overall performance of AMBs. This review article first introduces the corrosion behaviors of various metallic anodes including Zn, Al, Mg, and Fe. The mechanisms and corrosion products in different electrolyte systems, as well as potential damages to the battery, will be discussed in this review. Following that, we will detail various strategies that inhibit corrosion, with corresponding advancements highlighted. Then, the review summarizes advanced characterization approaches as measurement criteria for the metallic anode corrosion issue. The final section discusses the challenges and perspectives of this field, so that it presents insights for further development of AMBs.

2. Corrosion mechanism

Corrosion behaviors including corrosion product, corrosion rates, and side reactions are different for various metal anodes such as Zn,[7,27,28] Al,[21,29,30] Mg,[31] and Fe[32] in aqueous electrolytes due to their respective characteristics. Even for the same metal, its corrosion behaviors vary with the environment it is in. This section will summarize and discuss the corrosion mechanisms, influencing factors, and corrosion products of Zn, Al, Mg, and Fe anodes.

2.1 Corrosion behavior of Zn anodes

Aqueous Zn batteries including Zn-ion, Zn–air, and alkaline Zn–Ni are promising candidate systems for next-generation

energy storage.[33–37] From a thermodynamic point of view, Zn has a lower standard electrode potential (−0.763 V *vs.* SHE) than HERs in all pH ranges (Fig. 2a), which can theoretically predict that Zn is intended to be corroded in aqueous electrolytes. Zn's corrosion behaviors will be discussed in this section.

2.1.1 Corrosion of Zn in acidic electrolytes. As shown in the Pourbaix diagram (Fig. 2a), the corrosion behavior of Zn is influenced by the pH of electrolytes. Corrosion products vary from Zn^{2+} to ZnO, $Zn(OH)_2$, and $Zn(OH)_4^{2-}$ with the gradual increase in pH value (Fig. 2b). Generally, Zn is dissolved into various species after losing two electrons. The electrons are consumed by H^+, H_2O, O_2, or other oxidants at the Zn/electrolyte interface (Fig. 2c), leading to Zn self-corrosion. The corrosion rate of Zn *vs.* pH plot resembles the shape of "U", with the corrosion rate being minimum in the pH range from 8.5 to 12.[40]

In acidic electrolyte environments, the corrosion process of Zn can be expressed by the following equations:

$$\text{Anodic reaction: } Zn - 2e^- \rightarrow Zn^{2+} \quad (2.1)$$

$$\text{Cathodic reaction: } H^+ + 2e^- \rightarrow H_2 \quad (2.2)$$

Thermodynamically, the most stable Zn species formed in an acidic environment is Zn^{2+} (Fig. 2a). Zn corrosion proceeds under the cathodic control and the corrosion rate is determined by the cathodic HER kinetics.[41] The chemical kinetics of HERs controls the overall corrosion rate of Zn, when the pH value is smaller than 4.[42] When the pH increases to the range of 3–5, the transport of H^+ is slow and the corrosion rate of Zn is controlled by H^+ diffusion or a mixed kinetic.[43] Corrosion behaviors in acidic environments are illustrated in Fig. 2d. It should be noted that local pH at the corrosion interface may increase with continuous corrosion reactions and give rise to a different corrosion mechanism.

2.1.2 Corrosion of Zn in neutral electrolytes. In mild acidic or neutral electrolytes, the rate-limiting step of Zn corrosion shifts from the HER to the ORR, and the cathodic reaction can be expressed as follows:[41]

$$\text{Cathodic reaction: } 2H_2O + 2e^- \rightarrow 2OH^- + H_2 \quad (2.3)$$

$$O_2 + 2H_2O + 4e^- \rightarrow 4OH^- \quad (2.4)$$

ORR kinetics are activation controlled and are also independent of the solution pH due to the high irreversibility of ORRs. Dissolved oxygen plays a vital role in the cathode depolarization process and will accelerate Zn corrosion. Anodic reactions are

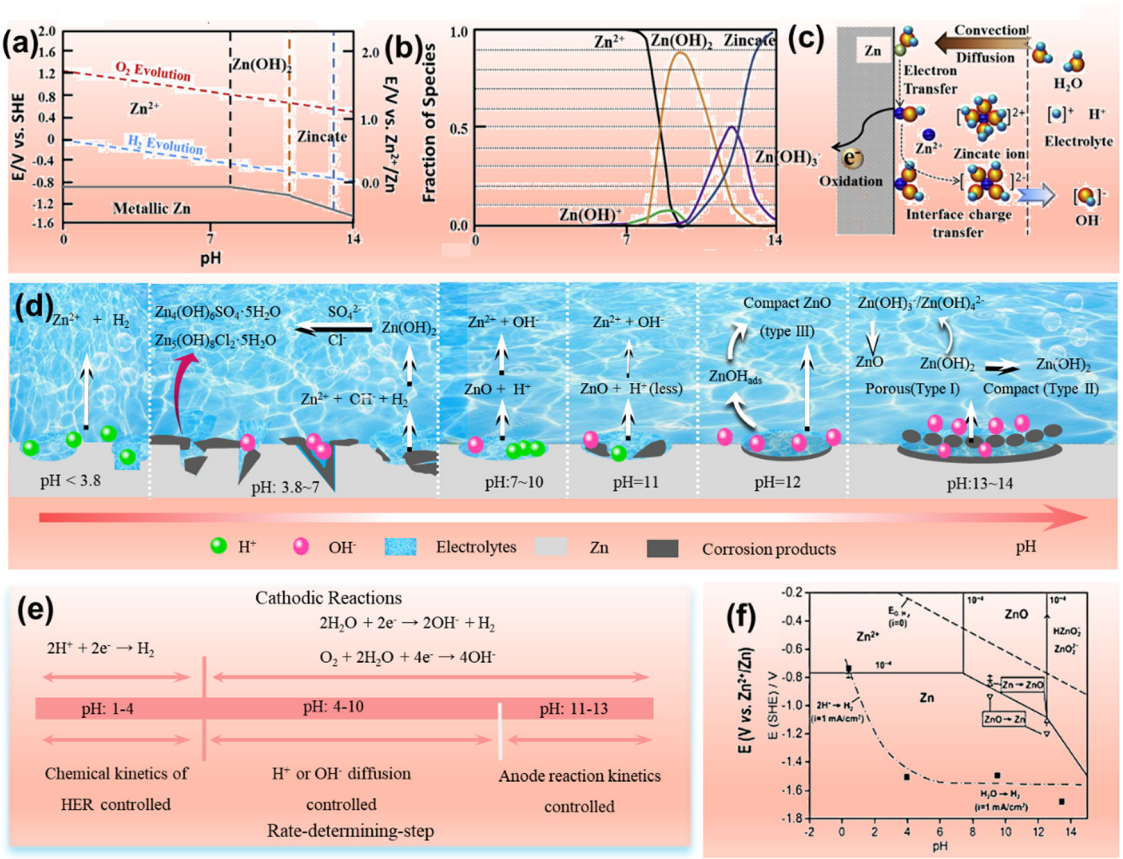

Fig. 2 (a) Pourbaix diagram of Zn–H_2O at 25 °C. (b) Fraction Zn species at different pH values. (c) Dissolution process illustration of Zn. Reproduced from ref. 38 with permission from Elsevier, copyright 2020. (d) Various Zn corrosion modes at different pH values. (e) Illustrations of cathodic reactions and rate-determining steps of Zn corrosion. (f) Pourbaix diagram with the consideration of kinetics factors for 10^{-4} mol L^{-1} Zn^{2+}. Reproduced from ref. 39 with permission from Elsevier, copyright 1991.

relatively complicated in this pH region, which can be expressed as follows:[41]

$$\text{Anodic reaction:}\quad Zn{-}2e^- \rightarrow Zn^{2+} \tag{2.1}$$

$$Zn^{2+} + 2OH^- \rightarrow Zn(OH)_2 \tag{2.5}$$

$$Zn(OH)_2 \rightarrow ZnO + H_2O \tag{2.6}$$

$$Zn(OH)_2 + 2OH^- \rightarrow Zn(OH)_4^{2-} \tag{2.7}$$

It is expected that Zn^{2+} will react with OH^- to form a $Zn(OH)_2$ precipitate (eqn (2.5)), parts of which can be dehydrated to form ZnO (eqn (2.6)). The local concentration of OH^- at very active corrosion sites may be high enough to form zincate ions (eqn (2.7)). Notably, the precipitate formed at this stage is porous and pseudo-passive, which will not reduce the corrosion rate (Fig. 2d). Anions including SO_4^{2-}, Cl^-, and ClO_4^- in the electrolytes may also participate in the corrosion reaction. Cl^- may react with Zn^{2+} or $Zn(OH)_2$ and form zinc chloride hydroxide according to the following reactions:[44]

$$5Zn^{2+} + 8OH^- + 2Cl^- + H_2O \rightarrow Zn_5(OH)_8Cl_2{\cdot}H_2O \tag{2.8}$$

or

$$5Zn(OH) + 2Cl^- + H_2O \rightarrow Zn_5(OH)_8Cl_2{\cdot}H_2O + 2OH^- \tag{2.9}$$

ClO_4^- ions can accelerate the dissolution of Zn due to their adsorption on the metal surface and subsequent participation in the active dissolution:

$$Zn + 2ClO_4^- \rightarrow Zn(ClO_4)_{2(aq)} + 2e^- \tag{2.10}$$

In the presence of SO_4^{2-}, a zinc hydroxide sulfate intermediate is formed and the intermediate is then hydrated through the following reaction:[45]

$$Zn(OH)_2 + 3Zn^{2+} + 4OH^- + SO_4^{2-} + 5H_2O \rightarrow Zn_4(OH)_6SO_4{\cdot}5H_2O \tag{2.11}$$

Compared with $Zn_4(OH)_6SO_4{\cdot}5H_2O$, $Zn_5(OH)_8Cl_2{\cdot}H_2O$ is more porous due to the aggressive nature of Cl^-. The tendency for these ions to be absorbed and to form ion pairs or complexes with dissolving Zn^{2+} ions follows the sequence of $ClO_4^- < SO_4^{2-} < Cl^-$.[46] Thus, the rate of active dissolution of Zn increases in the order of $ClO_4^- < SO_4^{2-} < Cl^-$. The electrolytes in zinc-ion batteries are typically mild acid or neutral (such as $ZnSO_4$, pH = 3–6), in which the corrosion of the Zn anode follows the mechanism discussed above.

2.1.3 Corrosion of Zn in alkaline electrolytes. In alkaline environments, the ORR is the main cathodic reaction (eqn (2.3) and (2.4)). When the pH is in the range between 7 and 10, Zn undergoes dissolution *via* two reactions as follows:

$$Zn + H_2O \rightarrow ZnO + 2H^+ + 2e^- \tag{2.12}$$

$$Zn + H_2O + H^+ \rightarrow Zn(OH)^+ + 2H^+ + 2e^- \tag{2.13}$$

Although ZnO is formed, it is pseudo-passive and cannot reduce the corrosion of Zn, which is similar to the condition in mild electrolytes. With continuous corrosion, a passive film is formed. However, the produced H^+ will simultaneously destabilize the passive film dynamically. The presence of the pseudo-passive layer is a net result of the passive layer formation and destabilization processes. Between pH 11 and 13, zinc oxides or zinc hydroxy complexes will be formed, and anode reaction kinetics will control the corrosion rate in this range. At pH 11, the metal hydrolysis reaction is limited, and as-produced H^+ is getting less. Thus, small domains of passivity are formed at pH 11. At pH 12, a compact ZnO passive film can be formed by an adsorption model or a nucleation-growth model, which can be expressed as follows:[47,48]

$$Zn + OH^- \rightarrow ZnOH_{ads} + e^- \tag{2.14}$$

$$ZnOH_{ads} \rightarrow ZnO + H^+ + e^- \tag{2.15}$$

$$Zn + 2OH^- \rightarrow ZnO + H_2O + 2e^- \tag{2.16}$$

This compact film is called type III oxide. It is thin but plays the most important role in inhibiting further corrosion. When the pH increases to 13–14, the $Zn(OH)_3^-$ complex will be generated *via* the following reactions:[41]

$$ZnOH_{ads} + OH^- \rightarrow Zn(OH)_2 + e^- \tag{2.17}$$

$$Zn(OH)_2 + OH^- \rightarrow Zn(OH)_3^- \tag{2.18}$$

With continuous corrosion, local supersaturation of these complexes will impede OH^- from transporting to the metal interface, thereby hindering further formation of the $Zn(OH)_3^-$ complex. Then, $Zn(OH)_2$ can gradually build upon the surface. Meanwhile, ZnO could also be formed by the dissolution of $Zn(OH)_3^-$ or $Zn(OH)_4^{2-}$ as follows:[41,47]

$$Zn(OH)_3^- + H^+ \rightarrow ZnO + H_2O \tag{2.19}$$

$$Zn(OH)_4^{2-} \rightarrow ZnO + H_2O + 2OH^- \tag{2.20}$$

As a result, a porous passivation film is produced and is called type I oxide. During this process, the dissolution of $Zn(OH)_2$ is the rate-determining step, and further corrosion reaction must occur across a porous layer. Once the local OH^- concentration drops to an extent, the dissolution of $Zn(OH)_2$ to zinc hydroxy complexes is stopped, and a well-defined passive layer is formed between the metal surface and the type I layer, which is described as type II oxide. Although type III oxide is produced in much smaller quantities than type I or II, it plays a more important role in making Zn transit to the passive state.[47] The Zn corrosion process in alkaline electrolytes is summarized and illustrated in Fig. 2d. The alkaline zinc batteries or zinc–air batteries typically select a high-concentration KOH solution as an electrolyte (pH > 13), suggesting that the Zn corrosion in these battery systems follows eqn (2.17)–(2.20).

The cathodic reactions and rate-determining steps are summarized and displayed in Fig. 2e. The HER is the only cathodic reaction in acidic electrolytes, and its chemical kinetics determine the overall corrosion rate. With the increase in pH to 4–6, H^+ ion diffusion or mixed kinetics control the corrosion rate. The ORR may also proceed due to the local drop of H^+ concentration.

In the pH range of 7–10, the ORR is the main cathodic reaction, which is also diffusion-controlled and independent of pH. Thus, the corrosion rates do not vary significantly in this range. With the further increase in pH, the passive film is gradually formed, and the corrosion rate is determined by the anode reaction kinetics. Taking the kinetic factors into consideration, the Pourbaix diagram can be expressed in Fig. 2f.

2.1.4 Other corrosion behaviors. In addition, some active species from cathodes, such as I_3^-, Br_3^-, and Br_2, will diffuse to the Zn anode and cause chemical corrosion of Zn. Hydrogen and oxygen evolution exists in Zn–I_2 cells and will become apparent with the accomplice of triiodide. While HER comes from the decomposition of water on the Zn anode surface, the oxygen evolution reaction (OER) might be ascribed to the redox reaction of iodine species with $Zn(OH)_2$.[49] However, there has still not been a definite description of the OER process. The cross-diffusion of Br_2/Br_3^- species generally exists in Zn–Br_2 batteries, which will cause the chemical corrosion of the Zn anode and result in self-discharge of the battery.[50–52]

Pitting corrosion is one of the most common corrosion types in Zn batteries. It will not occur in acidic electrolytes due to the clear surface of Zn. One important precondition for pitting corrosion is the presence of passivation films. Some researchers hold the view that pitting corrosion is caused by the specific absorption of aggressive halide ions (Cl^-, Br^-, and I^-) on the surface of the passivation film.[53,54] Once the halide ions penetrate the passivation film under pitting potential, corrosion pits emerge and local corrosion occurs. Local acidification theory is also widely accepted for interpreting the pitting behavior.[54,55] Zn hydrolysis (eqn (2.12) and (2.15)) increases the H^+ concentration locally and destabilizes the passivation film, paving the way for pitting corrosion. Besides, pitting corrosion easily takes place in the Zn/electrolyte/air triple-phase boundary due to the large amount of dissolved oxygen. Corrosion rates and corrosion potentials in pits and surrounding pseudo-passive regions are different. Once there exists the corrosion potential difference, a galvanic corrosion cell may be formed, in which Zn in pits acts as the anode and Zn under the pseudo-passivation film as the cathode. The formation of galvanic corrosion will accelerate the corrosion rate in the anode side.

2.2 Corrosion behavior of the Al anode

Aqueous Al batteries mainly include primary Al–air batteries and recently emerging aqueous Al-ion batteries, which normally employ highly alkaline or acidic electrolytes.[56–59] It is known that Al is amphoteric and is reactive in both acidic and alkaline environments. As illustrated in the Pourbaix diagram of Al–H_2O (Fig. 3a), the stable domain of Al is far below that of water, implying that Al strongly tends to be corroded with the decomposition of water. Based on the pH values, the dissolving species varies from Al^{3+} ions to Al_2O_3 and AlO_2^-. In this section, Al's corrosion mechanisms will be summarized and discussed.

2.2.1 Corrosion mechanisms in acidic electrolytes. A thin and compact oxide layer is covered on the surface due to Al's active nature. Without regard to the affection of anion ions, this oxide layer is soluble in acidic environments. An induction period can be observed before an apparent corrosion process, which should be ascribed to the dissolution of the oxide film. It is reported that the dissolution process of the Al_2O_3 film can be described as a chemical process or field-assisted process as follows:[60,61]

$$Al_2O_3 + 6H^+ \rightarrow 2Al^{3+} + 3H_2O \quad (2.21)$$

$$Al_{OX} \rightarrow Al_{aq}^{3+} + V_{Al(OX)}^{3-} \quad (2.22)$$

where Al_{OX} refers to aluminum atoms in the oxide film, Al_{aq}^{3+} refers to aluminum ions in aqueous solutions, and $V_{Al(OX)}^{3-}$ represents the formed aluminum vacancy in the oxide film. H^+ ions from the electrolyte migrate into the film and combine with O^{2-} remaining in the oxide lattice to form H_2O. Together with the removal of lattice O^{2+}, the ejection of Al^{3+} from the oxide lattice into the solutions leads to a dissolution of Al_2O_3 film (Fig. 3b). The migration of Al^{3+} from Al metal to the aluminum vacancies occurs simultaneously, accompanied by hydrogen evolution at the Al metal/Al_2O_3 interface, resulting in the pitting corrosions on the Al metal surface. After the total removal of the oxide film, bare Al is easily attacked by H^+ and gives rise to a rapid corrosion process as follows:

$$Al + 3H^+ \rightarrow Al^{3+} + 3/2H_2 \quad (2.23)$$

In the presence of anions such as Cl^-, SO_4^{2-}, and NO_3^-, the corrosion process gets more complicated due to the participation of these anions. Compared with other anions, Cl^- ions are more aggressive and can accelerate the corrosion rate remarkably. On the one hand, Cl^- ions assist in the dissolution of Al_2O_3 films initially and reduce the induction period. The absorbed Cl^- ions react with Al_2O_3 as follows:[61]

$$Al^{3+}(\text{in } Al_2O_3) + 4Cl^- \rightarrow AlCl_4^- \quad (2.24)$$

On the other hand, Cl^- ions can directly participate in the dissolution reaction of Al. In the induction period, Cl^- ions penetrate the oxide layer and form complexes, which leads to pitting corrosion and destroys the oxide film repair kinetics. The reaction can be described as follows:[61,62]

$$Al + nCl^- \rightarrow AlCl^{(n-3)-} + 3e^- \quad (2.25)$$

After total removal of the oxide film, Cl^- ions are specifically adsorbed onto the metal surface and replace the adsorption of water molecules, facilitating the transfer of Al from the metallic phase to the solutions in the form of a complex with Cl^- (as described in eqn (2.25)). The corrosion reactions of the Al anode in the recently developed aqueous Al-ion batteries, which typically use $AlCl_3$ as the electrolyte, can be explained by eqn (2.23)–(2.25).

Al corrosion in the acidic electrolytes containing SO_4^{2-} and NO_3^- is much slower and the corrosion mechanism is somewhat uncertain. The reduced corrosion rate in SO_4^{2-}-containing solutions may be caused by the less aggressiveness of SO_4^{2-} than that of Cl^-. It is also reported that the presence of SO_4^{2-} ions in Cl^--containing electrolytes can retard the corrosion reactions due to the stronger absorptive affinity of SO_4^{2-}.[63,64] However, at higher concentrations, SO_4^{2-} ions can attack the

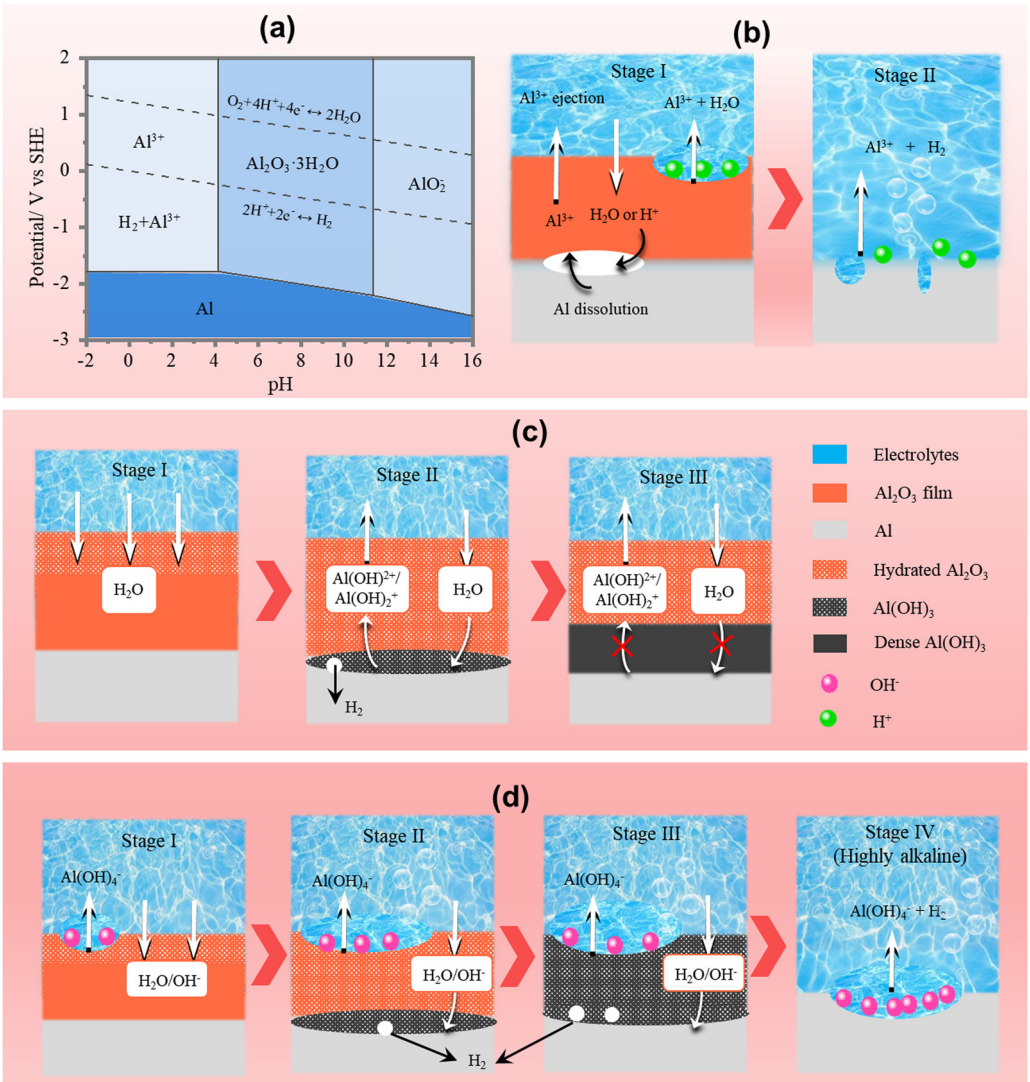

Fig. 3 (a) Pourbaix diagram of Al–H_2O at 25 °C. Illustration of the corrosion mechanism of the Al anode in (b) acidic electrolytes, (c) neutral electrolytes, and (d) alkaline electrolytes.

bare metal surface at the pre-existing pit bottoms. Another point of view suggests that a passive film containing $Al(OH)SO_4$ and $Al_2(SO_4)_3{\cdot}18H_2O$ is formed during exposure to a sulfate-containing environment.[65] This kind of passivation film might contribute to the low corrosion rate in electrolytes containing SO_4^{2-}.

It is generally believed that NO_3^- ions play an inverse role with H^+ and help develop and sustain a passive film, thus decreasing the corrosion rate. However, the reaction pathways are still not clear as numerous species have been found to be possible products, including $Al(NO_3)_3$, NO, NH_3, N_2, and NO_2^-.[66–69] Some researchers also argue that an increase in HNO_3 concentration would promote Al dissolution. The researchers stated that soluble complex ions were formed by complexation reactions between NO_3^- ions and hydrated Al^{3+} ions and, thus, increased the Al dissolution rate.[61,70] From the above discussions, it is speculated that the Al dissolution behavior is more likely affected by the nature of anions rather than by the pH value.

2.2.2 Corrosion mechanisms in neutral electrolytes. Al_2O_3 is insoluble in a neutral environment that can protect metal Al from rapid corrosion. Al corrosion in neutral solutions initiates with the hydrolysis of Al_2O_3 films, by which Al–O–Al bonds are disrupted to form Al–OH species.[71,72] With continuous hydrolysis, the amorphous Al_2O_3 transforms into a porous and poorly crystallized pseudo-boehmite (AlOOH) layer through which the water molecules can migrate to the Al/AlOOH interface. At this stage, the hydrolysis process controls the corrosion rate. Once the hydration front reaches the Al substrate, the Al corrosion reaction immediately occurs, and hydrogen evolution is accompanied.[73] Al^{3+} ions generated by anodic corrosion can react with OH^- ions that are formed by water reduction (eqn (2.3)), which can be expressed as follows:[62]

$$Al^{3+} + OH^- \rightarrow Al(OH)^{2+} \quad (2.26)$$

$$Al^{3+} + 2OH^- \rightarrow Al(OH)_2^+ \quad (2.27)$$

$$Al^{3+} + 3OH^- \rightarrow Al(OH)_3 \quad (2.28)$$

At this stage, the corrosion rate is determined by the nucleation and growth of aluminum hydroxide. The soluble $Al(OH)^{2+}$ and $Al(OH)_2^+$ species diffuse outward to electrolyte solutions and water penetrates to the $Al/Al(OH)_3$ interface, respectively. As the reactions continue, the hydroxide layer thickens and densifies gradually, playing a passivating effect on the corrosion process and slowing down the corrosion rate. Finally, the transport of these soluble species is the rate-determining step. Corrosion mechanisms of Al in mild electrolytes are illustrated in Fig. 3c.

Hydrogen produced from water reduction can diffuse through both Al and Al_2O_3 films. Once the generation rate of H_2 is higher than the diffusion rate, the hydrogen will nucleate and grow gas bubbles at the Al/Al_2O_3 interface. Eventually, the bubbles can generate sufficient pressure to blow holes through the passivation film and initiate pitting corrosion.[71]

2.2.3 Corrosion mechanisms in alkaline electrolytes. The corrosion mechanism of alkaline electrolytes is depicted in Fig. 3d. In weakly alkaline environments, the hydrolysis process is similar to that in neutral electrolytes, leading to a phase transformation from Al_2O_3 to AlOOH or $Al(OH)_3$. Water molecules or OH^- ions penetrate through this porous film to corrode Al, as described in eqn (2.3) and (2.28). With the precipitation of aluminum hydroxide at the Al/film interface, the dissolution of film by OH^- attacking occurs simultaneously at the film/electrolyte interface *via* the following reactions:

$$Al(OH)_3 + OH^- \rightarrow Al(OH)_4^- \quad (2.29)$$

The diffusion of OH^- ions and $Al(OH)_4^-$ to/away from the film/electrolyte interface is the rate-controlling step.[74] It should be noted that the direct ejection of Al^{3+} ions from oxide film to electrolyte can never occur in alkaline electrolytes due to the thermodynamic instability of Al^{3+} ions in alkaline solutions. Meanwhile, the dissolution of the Al_2O_3 film occurs at the film/electrolyte interface according to the following equation:

$$Al_2O_3 + OH^- + H_2O \rightarrow Al(OH)_4^- \quad (2.30)$$

In highly alkaline electrolytes, the oxide film on the surface of Al is totally dissolved and OH^- from electrolytes can directly attack the bare Al surface according to the following reaction:

$$Al + 4OH^- \rightarrow Al(OH)_4^- \quad (2.31)$$

Meanwhile, the influences of OH^- and $Al(OH)_4^-$ ion diffusions on the corrosion rate are not significant in highly alkaline environments due to the high concentration of OH^- and large solubility of $Al(OH)_4^-$ ions. Eqn (2.31) clearly defines the corrosion of the Al anode in the Al–air battery as a result of the electrolyte's excessive alkalinity.

2.2.4 Galvanic corrosion. Impurities or alloying elements that existed in the Al matrix would result in compositional heterogeneities. Intermetallic particles might be formed between alloying elements and aluminum, which presents different electrochemical potentials with aluminum matrix in the electrolytes. Galvanic cells will thus be formed between the aluminum matrix and the intermetallic particles. These solid solutions (such as Al_3Fe, Mg_2Si, Al_3Mg_2, and In–Sn inclusions[20,65,75,76]) typically present more noble electrochemical potentials than aluminum matrix and act as cathodes, leading to the local dissolutions of aluminum matrix adjacent to the intermetallic particles. In this galvanic cell, galvanic current goes from intermetallic particles with a higher corrosion potential to the aluminum matrix with a lower corrosion potential, resulting in the anodic polarization of the aluminum matrix and cathodic polarization of intermetallic particles. As a result, the aluminum matrix will be corroded with a promoted corrosion rate, leading to pitting corrosion.

2.3 Corrosion behavior of the Mg anode

Mg metal aqueous batteries mainly refer to primary Mg–MnO_2 and Mg–air batteries with neutral electrolytes. Rechargeable Mg–air batteries are still far from being practical because of the low energy conversion efficiency and low high-rate stability of Mg. Mg anode suffers from more severe self-corrosion than Al and Zn due to its more reactive nature. As illustrated in the Mg–H_2O Pourbaix diagram (Fig. 4a–c), Mg's almost no stable domain in aqueous electrolytes in the whole pH range due to its much lower equilibrium potential than hydrogen evolution potential. Compared with those of Al and Zn, the corrosion behaviors of Mg in aqueous electrolytes are more complicated. This section will discuss and summarize the corrosion mechanisms of Mg and their influencing factors.

2.3.1 Mechanisms containing MgH_2 or Mg^+. Before beginning, several special and unusual phenomena in the Mg corrosion electrochemistry should be aware of. The first and foremost is the negative difference effect (NDE), which represents the hydrogen evolution rate on a dissolving Mg surface increasing during anodic polarization.[77] Second, the self-corrosion potential of Mg is much more positive than the equilibrium potential, though Mg is very inclined to be corroded in aqueous electrolytes.[78,79] The last one is that a dissolution hysteresis phenomenon generally exists under corrosion potential or weak polarization in neutral and alkaline environments.[80] The above-mentioned phenomena are experimentally observed and should be interpreted by a precise corrosion mechanism.

Until now, several corrosion mechanism hypotheses have been proposed, including the magnesium hydride intermediate model, univalent Mg-based model, film-based model, and metal spalling model. However, these models are controversial and cannot individually interpret all the corrosion behaviors. The magnesium hydride intermediate model suggests that MgH_2 exists on the Mg surface (Fig. 4b) and plays a vital role in the corrosion process.[81,82] Mg is first reduced to MgH_2, which can be further oxidized to $Mg(OH)_2$ (in neutral or alkaline environments) or Mg^{2+} (in acidic environments). These processes can be expressed as follows:

$$Mg + 2H^+ + 2e^- \rightarrow MgH_2 \quad (2.32)$$

$$MgH_2 + 2H_2O \rightarrow Mg(OH)_2 + 2H_2 \quad (2.33)$$

$$MgH_2 + 2H^+ \rightarrow Mg^{2+} + 2H_2 \quad (2.34)$$

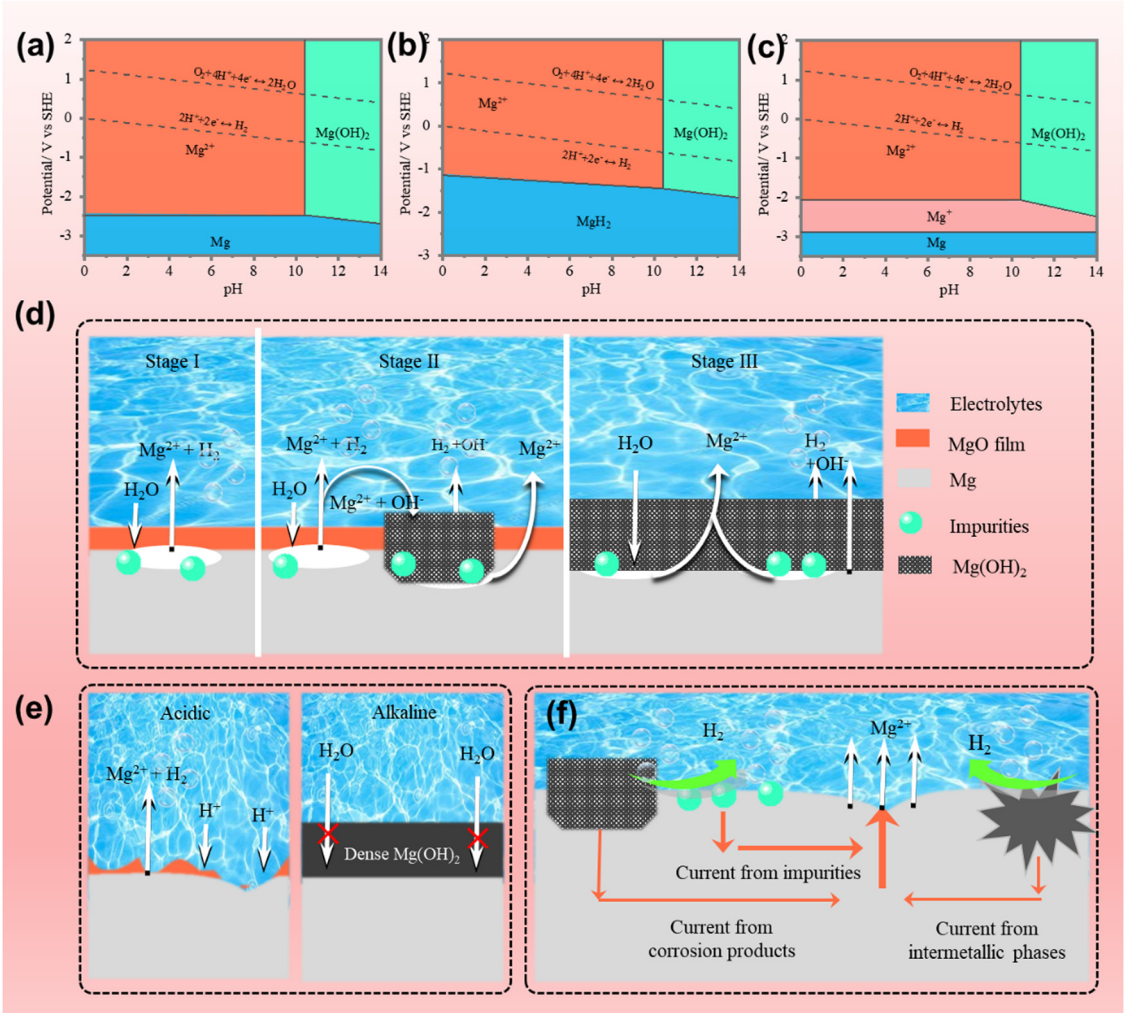

Fig. 4 Pourbaix diagrams of Mg–H_2O at 25 °C (a) without Mg^+ and MgH_2, (b) in the presence of MgH_2, and (c) in the presence of Mg^+. Corrosion mechanism of Mg (d) in neutral electrolytes, and (e) in acidic and alkaline electrolytes. (f) Galvanic corrosion mechanism of Mg.

Mg can also be dissolved directly in the uncovered regions by the following reaction:

$$Mg - 2e^- \rightarrow Mg^{2+} \quad (2.35)$$

The formation of MgH_2 is a cathodic reaction, so the NDE cannot be reasonably explained. The univalent Mg-based model indicated that the dissolution of Mg initiates with the formation of Mg^+ (Fig. 4c) as follows:[83,84]

$$Mg - e^- \rightarrow Mg^+ \quad (2.36)$$

Mg^+ ions are not stable and will be further oxidized to Mg^{2+} *via* the following reactions:

$$2Mg + 2H^+ \rightarrow 2Mg^{2+} + H_2 \quad (2.37)$$

$$2Mg^+ + 2H_2O \rightarrow 2Mg^{2+} + 2OH^- + H_2 \quad (2.38)$$

The NDE can be understood *via* the above-mentioned oxidization processes. However, this mechanism cannot interpret the dissolution hysteresis phenomenon in neutral or alkaline environments. Besides, Mg^+ species have never been experimentally detected, suggesting the irrationality of this mechanism.

2.3.2 Film-based mechanism and spalling mechanisms. The film-based model implies that the protective film composed of MgO/$Mg(OH)_2$ is easily formed due to the reactive nature of Mg, and can be generated even under cathodic polarization. During continuous anodic polarization, the film is gradually broken, and the bare Mg surface increases, accelerating Mg dissolution and hydrogen evolution.[85,86] This model can explain the dissolution hysteresis phenomenon and NDE in neutral or alkaline environments. However, it does not explain the NDE in acidic environments, as the film is unstable in an acidic medium.

Due to the uneven corrosion behaviors, the spalling mechanism infers that Mg dissolves as minute particles or flakes to spall off.[87] Further corrosion of these metallic Mg particles would result in the generation of H_2 with no current flow. Though this mechanism can explain the NDE, Mg's relatively positive corrosion potential cannot still be thoroughly explained.

2.3.3 Comprehensively phenomenological mechanism. According to the up-to-date research results, two facts have

been announced: Mg^+ ions and deciduous Mg particles do not participate in the corrosion process.[88–91] A more comprehensive phenomenological model is then proposed. It demonstrates that Mg corrosion is initiated with the local breakdown of MgO film, and the NDE is ascribed to the formation of the $Mg(OH)_2$ product.[80] Localized breakdown of the MgO film starts at certain susceptible sites, even under the cathodic polarization process, especially in the presence of aggressive ions.[92] Mg is dissolved in these breakdown regions according to eqn (2.35). The presence of impure elements such as Fe, Cu, and Ni can enhance the dissolution of Mg around these impurities. Local alkalinization is simultaneously achieved in the corrosion regions due to water reduction.[93] Partial dissolved Mg^{2+} ions diffuse to the electrolyte, while the others precipitate with OH^- ions to form $Mg(OH)_2$ on the surface. The formed $Mg(OH)_2$ plays an acceleration role in Mg dissolution and hydrogen evolution. The dissolution of Mg occurs at the MgO/$Mg(OH)_2$ interface with $Mg(OH)_2$ as the cathode.[93,94] Partial electrons that occurred on $Mg(OH)_2$ are consumed by HERs and cannot be detected by the measurement system, resulting in the NDE.[92] With continuous anodic polarization, $Mg(OH)_2$ gradually increases, leading to more hydrogen evolution and Mg dissolutions. Meanwhile, an enrichment of impurities is observed in the $Mg(OH)_2$ matrix, which would further enhance the hydrogen evolution and Mg dissolutions.[89,95] The above-mentioned results imply that the NDE is determined by $Mg(OH)_2$ and entrapped noble impurities. It should be noted that the corrosion attack progresses horizontally rather than perpendicularly until $Mg(OH)_2$ is propagated all over the MgO surface. With persistent local alkalinization, the early formation of $Mg(OH)_2$ passivates and cathodic activity on it is reduced until a dynamic equilibrium is attained.[93] This mechanism is more rational to describe the Mg corrosion behaviors and is summarized in Fig. 4d. The overall corrosion of Mg in a neutral environment can be described as follows:

$$Mg + H_2O \rightarrow Mg^{2+} + 2OH^- + H_2 \quad (2.39)$$

Since Mg–MnO_2 or Mg–air batteries typically use a neutral NaCl electrolyte, the corrosion reaction mechanism of the Mg anode can be described by eqn (2.39).

$Mg(OH)_2$ is stable in aqueous electrolytes at a pH higher than 10.5 and serves as a protective barrier to further corrosion (Fig. 4e). In acidic environments, the MgO/$Mg(OH)_2$ film is highly soluble, giving rise to a rapid corrosion reaction as follows:[96,97]

$$MgO + 2H^+ \rightarrow Mg^{2+} + H_2O \quad (2.40)$$

$$Mg + 2H^+ \rightarrow Mg^{2+} + H_2 \quad (2.41)$$

The Mg matrix in Mg alloys exhibits an analogous corrosion mechanism with pure Mg. The HER is the main cathodic reaction of Mg corrosion due to its much higher equilibrium potential than that of Mg/Mg^{2+}. Though dissolved oxygen influences corrosion behavior, the effect is quite weak, which is not typically considered.

2.3.4 Galvanic corrosion mechanism. Galvanic corrosion accounts for a large part of Mg corrosion, which is illustrated in Fig. 4f. Impurities in Mg metal mainly include Fe, Cu, and Ni, which all present more noble corrosion potentials than Mg. Thus, galvanic cells are formed with these impurities as cathodes, leading to an accelerated dissolution of Mg around the impurities. The α-Mg phase is relatively active in Mg alloys and exhibits a higher corrosion tendency than all other phases, implying that galvanic cells exist in all Mg alloys with α-Mg phase as an anode.[98,99] Galvanic cells can even be formed inside the α-Mg phase due to the uneven distribution of alloying elements. As discussed in the last section, the local corrosion of Mg is also a type of galvanic corrosion in which the corrosion product acts as the cathode.

2.4 Corrosion behaviors of Fe and other metallic anodes

Fe-based aqueous batteries mainly include alkaline Fe–Ni batteries,[100] Fe–air batteries,[101] and recently reported Fe–S batteries, Fe–I_2 batteries, as well as Fe-ion batteries with weakly acidic $FeSO_4$ electrolytes.[102–104] The Fe anode is prone to be corroded in acidic electrolytes due to its lower equilibrium potential than hydrogen evolution potentials, which can be described as follows with the HER as a cathodic reaction:[105]

$$Fe + 2H^+ \rightarrow Fe^{2+} + H_2 \quad (2.42)$$

In the presence of dissolved oxygen, the corrosion process can also proceed through the following reaction with ORR as a cathodic reaction:

$$Fe + 2H^+ + O_2 \rightarrow Fe^{2+} + H_2O \quad (2.43)$$

When the pH value of electrolytes is higher than 6, the ORR is the main cathodic reaction. In the absence of dissolved oxygen, the Fe corrosion rate is relatively low. The corrosion reaction is accompanied by water reduction and hydrogen evolution, which can be described as follows:

$$Fe + 2H_2O \rightarrow Fe^{2+} + 2OH^- + H_2 \quad (2.44)$$

Fe^{2+} ions are soluble in neutral electrolytes and $Fe(OH)_2$ may be formed on the surface locally due to the increase in OH^- concentrations in the corrosion area. In alkaline electrolytes, the Fe^{2+} ions generated from corrosion precipitate on the surface with OH^- from electrolytes, which results in the passivation of Fe and protects Fe from further corrosion. It should be noted that the passive film is hardly formed in the presence of aggressive ions (such as Cl^- and Br^-).

From the above-mentioned discussions, Fe corrosion is mainly affected by the pH of electrolytes, dissolved oxygen, and anions in the electrolytes. Besides, the charge/discharge states of alkaline Fe-based batteries may influence corrosion behaviors. Fe is known to be transformed into $Fe(OH)_2$, Fe_3O_4, and $Fe(OH)_3$ during the discharge process. These discharge products have inhibition on the corrosion of Fe. However, this passivation would also result in a decrease in battery kinetics.

Metallic Li and Na are so reactive with water that they cannot be utilized directly as anodes in aqueous electrolytes. The reactions are described as follows:

$$2Li + H_2O \rightarrow 2LiOH + H_2 \quad (2.45)$$

$$2Na + 2H_2O \rightarrow 2NaOH + H_2 \quad (2.46)$$

Li and Na metals must be protected with coating layers to prevent them from corrosion by water in aqueous Li metal and Na metal batteries.

2.5 Influencing factors and derived problems

2.5.1 Influencing factors. Generally, metallic anode corrosion can be affected by electrolytes, working conditions, and the metallic anode itself (Fig. 5). As to the electrolytes, the pH values play a crucial role in affecting the corrosion behaviors of metallic anodes. On the one hand, the corrosion reaction pathways at different pH values are different, as discussed in the previous sections. On the other hand, the stabilities of passivation film on the metal surface are different under various pH environments, which has much influence on the corrosion rates. Types and concentrations of anions have been proven to significantly affect the corrosion behaviors of metallic anodes due to the diverse properties of the as-formed complexes. Typically, aggregative ions including Cl^-, Br^-, I^-, and ClO_4^{2-} can accelerate the corrosion rate due to their high penetrability across the passivation film, preferable absorption on metal surface, or high oxidizability. Other anions such as CrO_4^{2-} and CO_3^{2-}, which can form protective complexes with metals, play an inhibitory role in corrosion reactions.[54] Taking Al as an example, its corrosion rate in the presence of anions increases in the order of $Cl^- > ClO_4^- > SO_4^{2-} > NO_3^-$.[61,106] It is also reported that aggressive ions including Cl^-, Br^-, and ClO_4^- can accelerate the pitting corrosion of Mg, while other passivated ions such as F^-, CrO_4^{2-}, and CO_3^{2-} will inhibit the Mg corrosion due to the formation of passivation films.[107–109] Besides, dissolved oxygen will accelerate the corrosion reaction that is accompanied by the cathodic ORR. However, dissolved oxygen has little influence on Mg corrosion due to the much higher HER rates. Additives in the electrolytes can also make big differences in the corrosion behaviors, which may generate a protective film on the metal face or competitively absorb onto the active sites to reduce cathodic reactions.

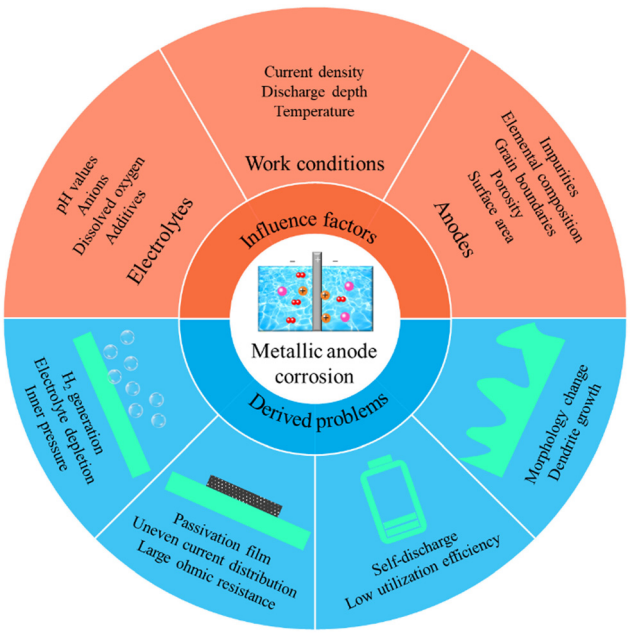

Fig. 5 Influencing factors and derived problems of metallic anode corrosion.

Corrosion behaviors under various working conditions including temperature, charge/discharge states, and charge/discharge rates are different. For example, at low current densities, OH^- can efficiently transport across the porous type I ZnO passivation layer and inhibit the formation of the compact type II ZnO layer.[7] Besides, the morphology and surface products will change with continuous charge/discharge process, leading to a variation in corrosion behaviors. Higher operating temperatures are reported to promote the corrosion rate except in the electrolytes with sulfates and nitrates.[61,73]

The properties of metallic anodes such as specific surface area, porosity, and particle size also influence corrosion behaviors. Anodes with sufficient porosity and high specific surface area will cause enhanced corrosion susceptibility due to the difficult formation of a passivation layer and improved corrosion interface.[7,110] Pitting corrosions or galvanic corrosions prefer to occur at grain boundaries or cracks due to the microstructural or compositional differences,[76,111] suggesting that a more uniform surface or phase structure is preferable for corrosion inhibition. The elemental composition of metallic anodes also affects the corrosion process. Elements with a higher HER overpotential in the anodes, such as In, Sn, and Bi, will hinder the parasitic HER and, thus, reduce the corrosion rates. Moreover, the intermetallic phases in the anodes formed in the alloying process will also influence the corrosion process. Especially for Mg alloys, the second phase can serve as a cathode and enhance the dissolution of Mg at the α-Mg phase/secondary phase interface due to its more noble electrochemical activity than the Mg matrix.[112] However, the continuous distribution of the second phase can suppress further Mg corrosion propagation. In addition, impurities in the metallic anodes may promote metal dissolutions around the impurities through the galvanic corrosion process.

Thus, the effects of the electrolyte composition and the metal anode itself on the battery's electrochemical performance and corrosion of the metal anode must be thoroughly taken into account when manufacturing aqueous metal batteries. Some factors need particular consideration. The starting point is to choose a metal anode that has a low specific surface area, good structural uniformity, and minimal impurities. The anode's processing technology must meet strict specifications to guarantee that there are as few defects and grain boundaries as feasible. It is necessary to eliminate contaminants from the metal anode, particularly those that contain metal elements with a lower hydrogen evolution overpotential. Furthermore, choosing the right electrolyte is crucial. On the premise of ensuring that electrochemistry can operate, neutral or weakly acidic and weakly alkaline electrolytes should be selected as far as possible. In addition, electrolyte salts that include caustic anions should be avoided when choosing electrolyte salts. Ultimately, the oxygen content should be minimized during battery assembly; for instance, the electrolyte's dissolved oxygen can be evacuated through an inert environment.

2.5.2 Derived problems. A series of problems come with the corrosion reactions of metallic anodes (Fig. 5). In the first place, the HER is the simultaneous reaction of corrosion and produces rather copious hydrogen, which will not only be detrimental to the sealed battery structure but also cause electrolyte depletion. Batteries would fail to work due to the leakage of electrolytes at high internal pressures.[113] Moreover, continuous water reduction will cause electrolyte depletion and result in the performance degradation of the batteries. Second, metallic anode corrosion in mild or alkaline electrolytes would produce non-conductive byproducts or passivation layers. These corrosion products would reduce the stripping/plating efficiency of anodes and result in non-uniform current density distribution. Besides, high ohmic resistance aroused from the corrosion product leads to a severe delay in the practical operating voltage and poor rate performance of the batteries. Another problem is that metallic anode corrosion results in serious battery self-discharge and reduces anodes' utilization efficiency. Lastly, the morphology of the anode will be changed during cycling. For example, the non-uniform current distribution and concentration gradients caused by localized corrosion may lead to uneven redistribution of Zn active materials on the electrode surface, promoting the Zn dendrite growth.[3,110] In summary, corrosion of metallic anodes is deleterious to the battery performance in terms of kinetics, capacity, and cycling stability. While extensive efforts have been made in the design of cathode materials, researchers should also pay more attention to the corrosion issue of anodes.

3. Corrosion inhibition

3.1 Artificial interface engineering

The artificial interface on the metallic anode surface plays an essential role in corrosion inhibition by protecting the metallic anode from direct exposure to the aqueous electrolytes. A stable metal/electrolyte interface can be established, thereby increasing the cycling stability of metallic anodes. Typically, this interface serves as a physical barrier and confines the transport of OH^-, H^+, H_2O, and other aggressive anions to metal surfaces (Fig. 6a). Surface chemistry at the interface such as charge

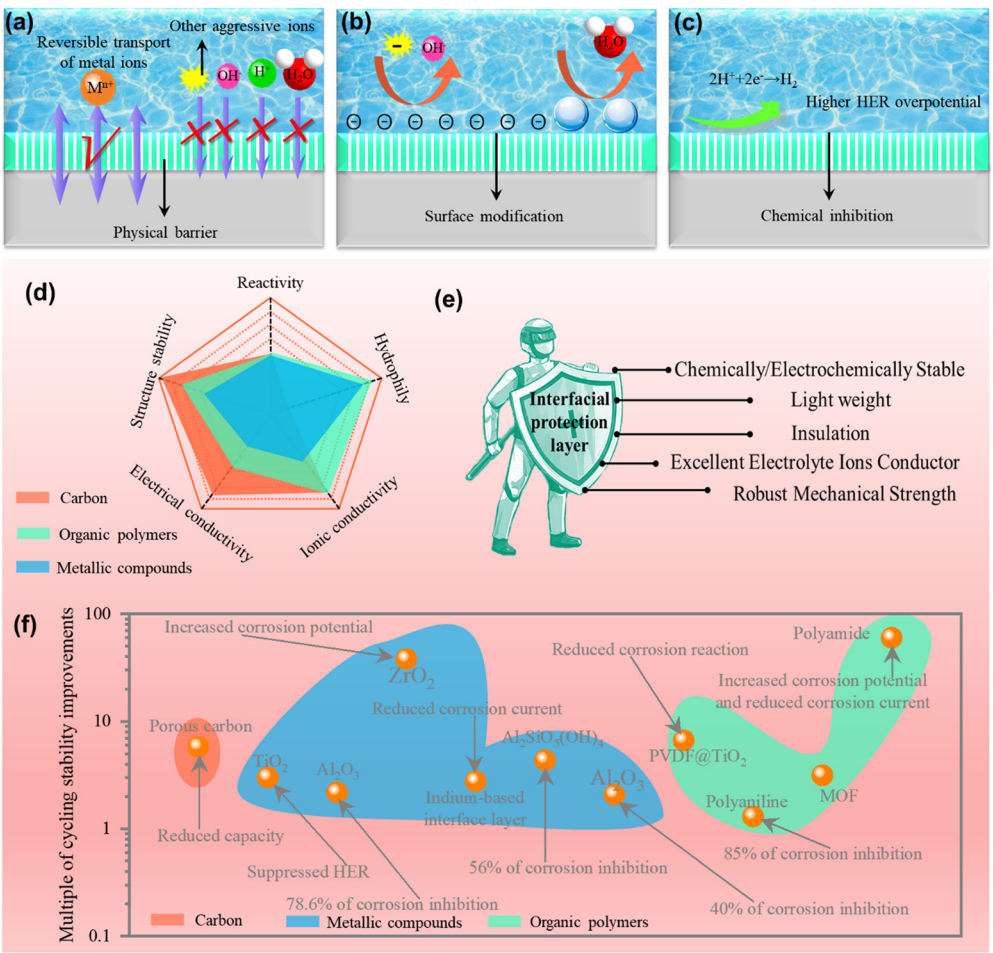

Fig. 6 Schematic of corrosion inhibition mechanisms for interface engineering: (a) physical barrier, (b) surface modification, and (c) chemical inhibition. (d) Properties of carbon coating layers, metallic compounds, and organic polymers. (e) Requirements for an ideal interfacial protection layer. (f) Corrosion inhibition performance for various artificial interfaces. Reproduced from ref. 49 and 115–124 with permission from John Wiley & Sons, Elsevier, and the Royal Society of Chemistry.

property and hydrophobicity may also be changed and prohibit the accessibility of specific ions and water molecules (Fig. 6b).[114] Besides, introducing metallic-based interfaces with higher HER overpotentials would suppress the HER at the interface (Fig. 6c). According to the above-discussed corrosion mechanism, five crucial factors, namely reactivity, structural stability, electrical conductivity, ionic conductivity, and hydrophilicity, should be taken into consideration to construct robust interfaces (Fig. 6d). A more reactive property than the metallic anode is preferred for reactivity if the protective layer is conductive. Otherwise, a galvanic cell will be formed with the layer as a cathode, accelerating metallic anode corrosion. As for the structural stability, the coating layer should be robust in the electrolytes and keep working during the battery cycling process. From the aspect of electrical conductivity, a semiconductor or insulator is desirable because it will not form a galvanic cell with the sheltered metal anode. Besides, the metal ions will not plate on the outer protective film surface.[3] For ionic conductivity and hydrophilicity, a good metal ion conductor with superior hydrophilicity is beneficial for the metal ion transport during the charge/discharge process, which enhances the reaction kinetics.[38] In conclusion, there are several requirements that the perfect artificial interface layer should fulfill (Fig. 6e). It should be light and not drastically lower the energy density of the battery. Excellent chemical and electrochemical stability is another requirement for the perfect interface coating to guarantee its continued functionality throughout the battery's extended charge and discharge cycles. To guarantee that the electrolyte ions may penetrate the interface layer and uniformly deposit on the metal negative electrode's surface, it should also possess superior ion conductivity and insulation. Furthermore, it must have strong mechanical properties to prevent breaking or falling off while the battery is operating. Recent advancements in corrosion inhibition by various artificial interfaces are summarized in Fig. 6f and Table 1.

3.1.1 Carbonaceous interface. The carbonaceous layer is advantageous as it is lightweight, easy to assemble, and hydrophobic with diverse properties (Fig. 6d). Its lightweight nature endows the batteries with high energy density, which is superior to metallic compound coating layers. The carbon layer can be coated onto a metallic powder anode or plate with tunable morphology and porosity. It is reported that a Zn@C core–shell structure can protect the Zn particles present inside from electrolyte leaching (Fig. 7a), giving rise to a relatively homogeneous electric field distribution and less amounts of byproducts.[135] The layers' uniformity, thickness, and porosity play a vital role in the corrosion protection effect.[136] A nonuniform or heavily porous coating layer cannot effectively restrain the water molecules from passing through. Though a thicker layer provides better corrosion resistance, it would suppress the ion transport, resulting in more sluggish kinetics of the batteries. In this aspect, a uniform ion-sieving carbon shell with a controllable thickness and pore size was proposed, through which the Zn passivation problem was well resolved in alkaline electrolytes.[137] A hydrogen-substituted graphdiyne (HsGDY), with sub-ångström level ion tunnels and robust chemical stability, was also designed (Fig. 7b). By tailoring the pore size, Zn ions with smaller sizes could freely pass through the layer and Zn^{2+} reached a uniform distribution along the rough surface of the Zn electrode.[137,138] As a result, the protected anode outperformed bare ZnO and Zn foils with a much-improved cycling life.

Table 1 Corrosion inhibition performances of various coating layers

	Anode	Electrolyte	Coating layer	Corrosion inhibition efficiency	Battery performance	Ref.
1	Zn	3 M $Zn(SO_3CF_3)_2$	TiO_2	Suppressed HER	Enhanced cycling stability	115
2	Zn	9 M KOH	Al_2O_3	78.6%	Enhanced cycling stability	116
3	Zn	6 M KOH	Porous carbon	—	Reduced capacity but enhanced stability	117
4	Zn	7 M KOH	Polyaniline	85%	Enhanced stability	118
5	Zn	6 M KOH	SiO_2	40%	—	125
6	Zn	2 M $ZnSO_4$	MOF	—	Enhanced cycling stability	49
7	Zn	2 M $ZnSO_4$	ZrO_2	Higher E_{corr}	Enhanced cycling stability	119
8	Zn	2 M $ZnSO_4$	Indium-based interface layer	Lower I_{corr}	Enhanced cycling stability	120
9	Zn	2 M $ZnSO_4$/ 0.1 M $MnSO_4$	$Al_2Si_2O_5(OH)_4$,	56%	Enhanced cycling stability	121
10	Zn	2 M $ZnSO_4$	PVDF@TiO_2	Reduced corrosion reaction	Reduced capacity but enhanced stability	122
11	Zn	2 M $ZnSO_4$/ 0.1 M $MnSO_4$	Polyamide	Higher E_{corr} and lower I_{corr}	60-fold enhancement in running lifetime	123
12	Zn	3 M $Zn(SO_3CF_3)_2$	Al_2O_3	40%	Enhanced cycling stability	124
13	Zn	6 M KOH	Neodymium film	90.9%	—	126
14	Zn	2 M $ZnSO_4$	Zn_2SiO_4/CNT	lower I_{corr} and more positive E_{corr}	Extended lifespan	127
15	Zn	2 M $ZnSO_4$	ZnSn alloy interphase	Lower I_{corr}	250% improvement in cycling life	128
16	Zn	2 M $ZnSO_4$	Graphene acid/carbon nanofiber	Lower I_{corr}	Ultra-low self-discharge behavior	129
17	Zn	2 M $ZnSO_4$	Hydroxyapatite	Higher E_{corr} and lower I_{corr}	10 times longer lifespan	130
18	Zn	2 M $ZnSO_4$	Cellulose	61.9%	Improved ICE and cycling stability	131
19	Zn	2 M $ZnSO_4$	Dopamine-functionalized polypyrrole	Higher corrosion voltage and reduced H_2 generation	5 and 2.5 times higher capacity retentions	132
20	Zn	2 M $ZnSO_4$	$ZnNb_2O^6$	Lower I_{corr}	Longer-term stable cycling	133
21	Al	PAA–KOH	Prussian blue	81.2%	Increased anode efficiency and energy density	134
22	Al	4 M KOH	LDH-PVA-acetal	81.0%	Improved capacity and cycling stability	30

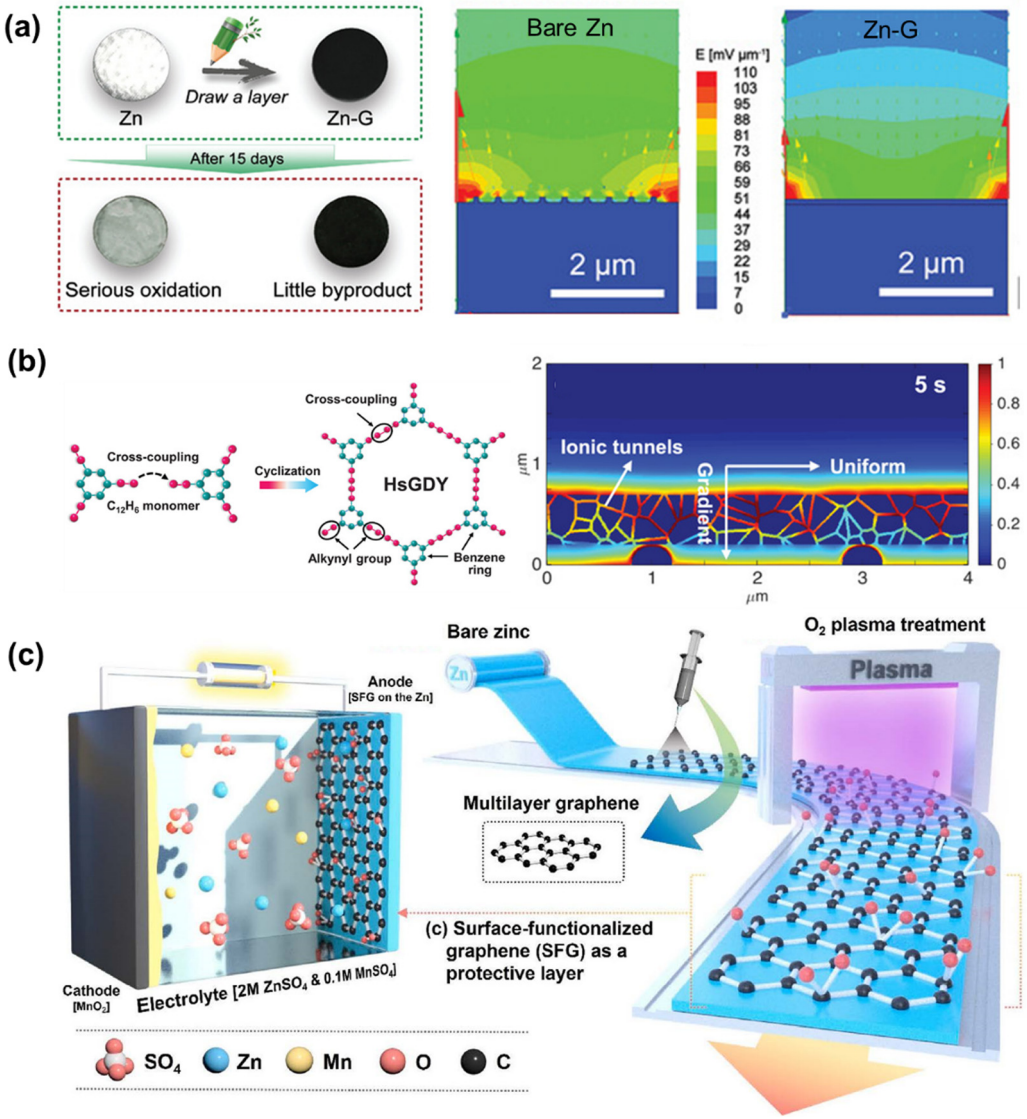

Fig. 7 (a) Diagram of the modification route and the electric field distributions of zinc and Zn–G anodes. Reproduced from ref. 135 with permission from John Wiley & Sons, copyright 2021. (b) Schematic of the synthesis of HsGDY and concentration field simulation after a constant diffusion duration of 5 s for Zn@HsGDY symmetric cell. Reproduced from ref. 138 with permission from John Wiley & Sons, copyright 2020. (c) Preparation diagram of zinc anode coated with a surface functional graphene layer. Reproduced from ref. 139 with permission from Elsevier, copyright 2023.

The hydrophobicity of the carbon layer should be taken into consideration. Carbon is advantageous in blocking water molecules due to its inherent hydrophobicity. Superhydrophobic surfaces have been proven to be qualified for corrosion inhibition of metals.[140,141] A superhydrophobic carbon black film prepared by electrospray is reported to protect stainless steel from corrosion in a sulfuric acid solution, exhibiting positive corrosion inhibition.[142] This work suggests that the hydrophobicity depends on the thickness of the carbon layer, and the porous carbon layers gradually lose the hydrophobicity in aqueous electrolytes because of the distant interaction of water vapor with the metal surface. Notwithstanding the effective protectivity, the hydrophobic surface would suppress the ion transport across the electrode/electrolyte interface, resulting in an inferior battery performance.

Apart from the role of the carbon layer as a physical barrier, the chemical properties of carbon influence corrosion protection. Functional groups decorated on the carbon can tune the accessibility of ions from electrolytes. A graphene film with abundant oxygen-containing groups was selected to protect Zn from corrosion (Fig. 7c), by which the aggressive anionic species were prohibited from accessing the metal surface.[139] Chemical modification of the carbon layer should have advantages in inhibiting specific ions from electrolytes, but related research is still limited.

Although the carbon layer has been proven effective in corrosion inhibition, several drawbacks remain. Carbon is typically electrically conductive and may cause metal ion plating or hydrogen evolution outside the layer. Moreover, the hydrophobic nature of carbon will enlarge the ion interface transport resistance and thus increase the overpotential or

voltage polarization of the metallic anode. A trade-off between corrosion protection and battery kinetic should be taken into account under this condition.

3.1.2 Metallic compound-based interfaces. Metallic compounds including Al_2O_3, TiO_2, Zn_2SiO_4, Si_3N_4, indium-based compounds, SiO_2, ZrO_2, $CaCO_3$, and kaolin layer manifest the merits of high mechanical strength and the variety of types.[119–121,125,143–145] They can serve as physical barriers to prevent the matrix metal anode from strong contact with aqueous electrolytes, thereby reducing the corrosion reactions (Fig. 8). In this sense, the corrosion inhibition depends on the uniformity and thickness of the coating layer. An increase in coating thickness leads to more complete coverage and a better prohibition of water penetration.[115,116] However, thick coating layers would cause inferior ions to transport kinetics over the electrode/electrolyte interface, thereby increasing the overpotential or voltage polarization.

Preparing thin and compact layers with good protectivity and ion conductivity may help break the confrontation. In contrast with the conventional doctor blade coating method, sol–gel method, and other solution methods, atomic layer deposition (ALD) is a promising thin-film deposition technique, which enables precise control of the thickness of the film with good protectivity. For instance, an ultrathin ALD TiO_x layer (Fig. 9a) has been reported to suppress the corrosion of the Al current collector.[154] The ALD TiO_x thickness can be precisely controlled (from a deposition rate of $\sim$0.02–0.04 nm cycle^{-1}) and the Ti-oxidation state was easily tuned by adjusting the $TiCl_4$ and H_2O precursor pulse lengths. As a result, the corrosion resistance of Al was improved by orders of magnitude. ALD Al_2O_3 was also reported to increase the corrosion resistance of the Zn anode.[115,116,124] Although the ALD Al_2O_3-protected Zn anode exhibited a higher overpotential initially due to the insulating nature of Al_2O_3, it outperformed bare Zn during the long-term cycling process in terms of lower resistance and smoother surface. Moreover, ALD Al_2O_3 layers gave rise to improved surface wettability, suggesting that this strategy enables both promising corrosion inhibition and fast reaction kinetics.

Beyond the ALD method, the *in situ* formation of the artificial interface on the metal surface is another effective strategy to control surface chemistry. A precisely controllable ZnS interface can be formed by treating Zn anodes with sulfur vapor (Fig. 9c), which serves as a physical barrier to inhibit corrosion and modifies the charge distribution at the interface.[155] The unbalanced charge distribution improved Zn^{2+} diffusion at the interface and adhesion of the ZnS layer to the metal surface, leading to both superior corrosion inhibition and fast ion transport kinetics. An "etching-nucleation-growth" strategy was also developed to generate a tightly arranged ultrathin $ZnSiO_3$ nanosheet array. The $ZnSiO_3$ is nucleated in the holes generated by the initial etching of Zn^{2+} ions, which gives the *in situ*-formed $ZnSiO_3$ strong adhesion to the Zn anode. The porosity and morphology of the protective layer can be regulated effectively by the pH and reaction time.

Some specific metal compounds such as indium-based species, Al_2O_3, and Bi_2O_3 serve as not merely physical barriers

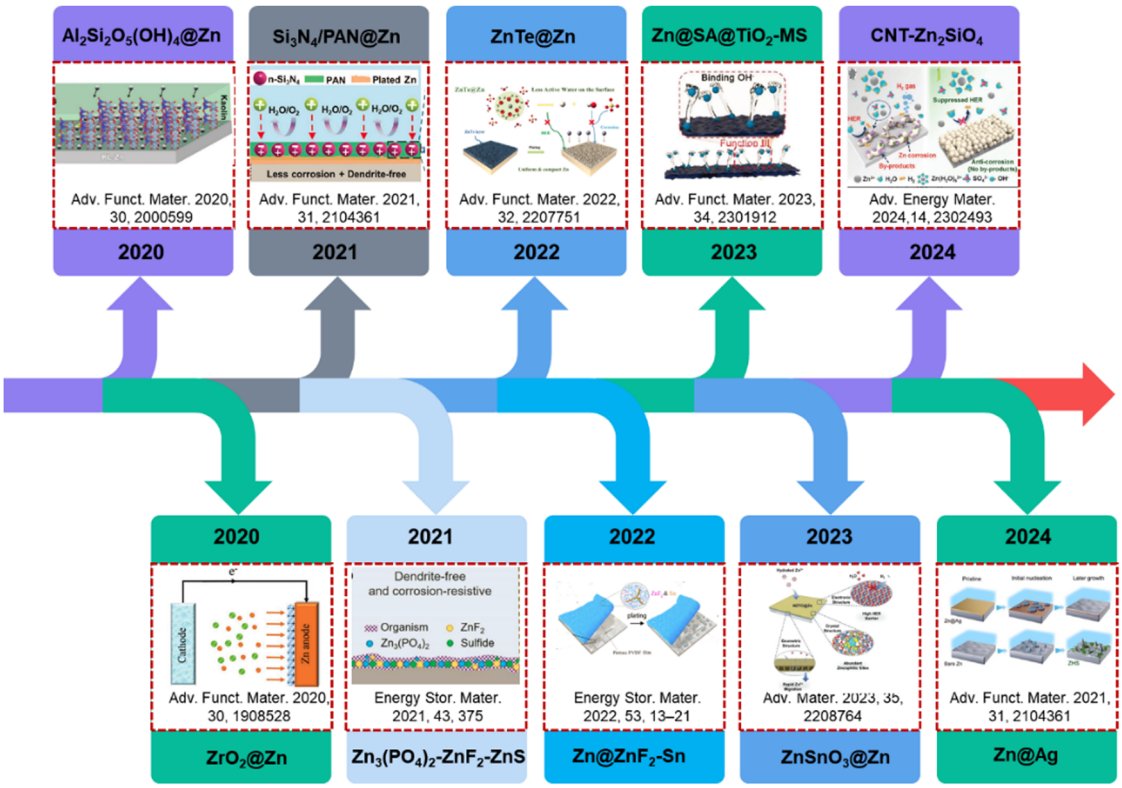

Fig. 8 Timeline of metallic compound-based interfacial layer strategies for metallic anode protection from 2020 to 2024. All insets were obtained from the literature.[119,127,146–153]

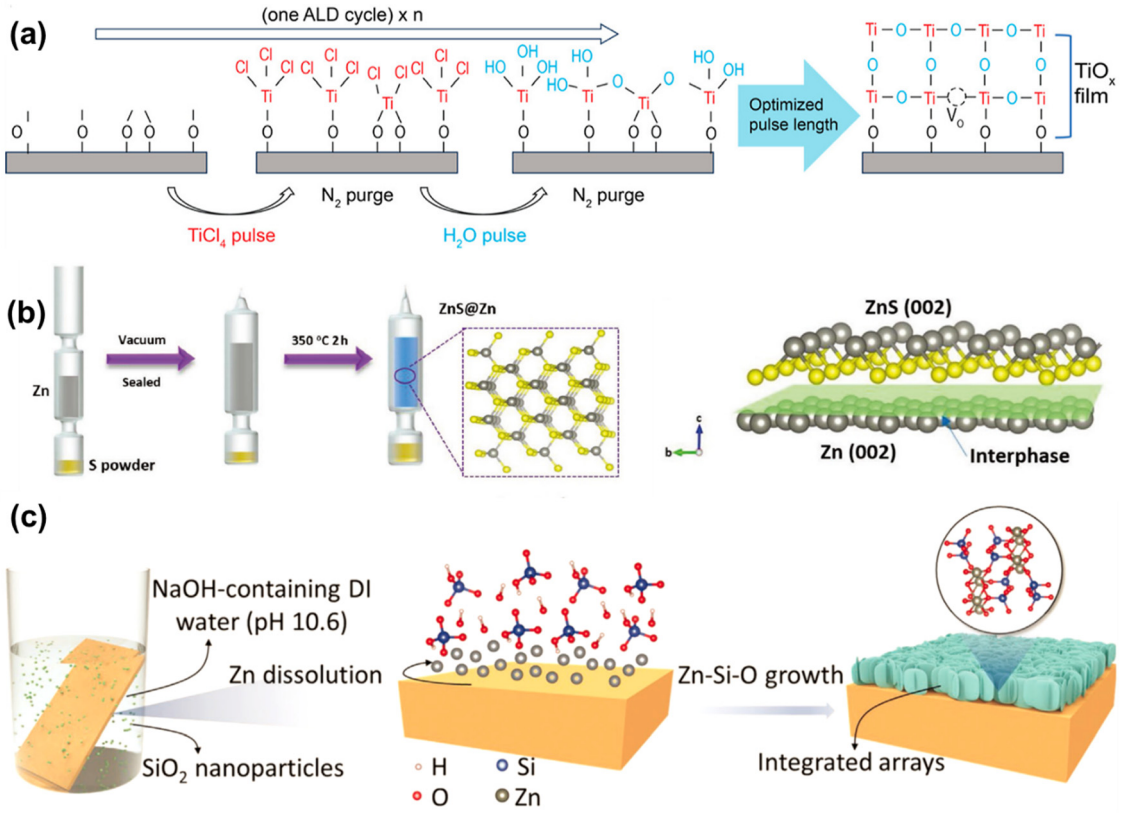

Fig. 9 (a) Illustration of a single ALD cycle with a TiO_x coating of thickness of ~0.04 nm. Reproduced from ref. 154 with permission from the American Chemical Society, copyright 2024. (b) Schematic of the artificial ZnS layer preparation. Reproduced from ref. 155 with permission from John Wiley & Sons, copyright 2020. (c) Schematic of the procedure for fabricating the Zn@ZSO composite foil. Reproduced from ref. 156 with permission from John Wiley & Sons, copyright 2022.

but also chemical corrosion inhibitors owing to their higher hydrogen evolution overpotential. Among various metal compounds, indium-based species such as In, In_2O_3, and $In(OH)_3$ manifest the best effect on suppressing hydrogen evolution because of the good chemical inactivity of indium.[28,120,143,157,158] A metallic indium layer will suppress HERs and by-product formation, give rise to uniform nucleation of Zn, and reduce Zn dendrites (Fig. 10). Benefiting from the promising corrosion inhibition effect, the cell performed well in long-term cycling without swelling.[143] Even in alkaline electrolytes, this strategy is proven to be effective. In_2O_3 and $In(OH)_3$ may be formed in alkaline electrolytes, which are insulative and can promote metal plating underneath the coating film.[120]

As to metallic compound-based protective layers, lower thickness, compact structure, and good ionic conductivity are preferred to provide desirable protection and avoid sacrificing the battery performance. While they are advantageous in mechanical strength and insulation (Fig. 6d), cracks may be formed during long-term cycling. Besides, their chemical stability in various electrolytes should be taken into consideration.

3.1.3 Organic polymer-based interfaces. The organic polymer coating layer is typically an all-in-one film originating from the robust covalent cross-linking network, which demonstrates outstanding structural stability and mechanical flexibility (Fig. 6d). Besides, interfacial ion transport can be regulated by sophisticated surface chemistry. Various organic layers have been employed to protect metal anodes from corrosion in aqueous electrolytes.[159–162] For example, an artificial polyamide (PA) layer was reported to protect Zn from corrosion in $ZnSO_4$. The interaction between Zn^{2+} and the PA chains enhances the adhesion of PA films on the Zn surface. The layer exhibited relatively low permeabilities towards water and oxygen even with a thickness of 40 μm, implying that the corrosion reactions on the Zn surface were effectively hindered (Fig. 11a).[123] An ethylenediamine tetramethylenephosphonic acid–Zn complex layer (EDTMP15-Zn) was also constructed on a Zn foil to suppress its corrosion (Fig. 11b).[163] The phosphate groups exhibited desirable zincophilicity and hydrophobicity, while the 3D network structure acts as smooth ion migration channels. The unique physicochemical properties of the EDTMP15-Zn film induce uniform Zn deposition and ensure good corrosion resistance. In addition to water and dissolved oxygen, corrosive species such as iodine species in the electrolytes can also be restrained by an organic layer (Fig. 11c and d).[49] Combining a physically protective polymer and chemically inactive metal oxides would be more efficient in corrosion inhibition.[30,122,146,149,164–166] An artificial protective layer containing a polyvinylidene fluoride (PVDF) matrix and decorated TiO_2 nanoparticles was proposed, which protected Zn from corrosion in long-term cycling and exhibited superior performance than pristine PVDF layers (Fig. 11e and f).[122] Other

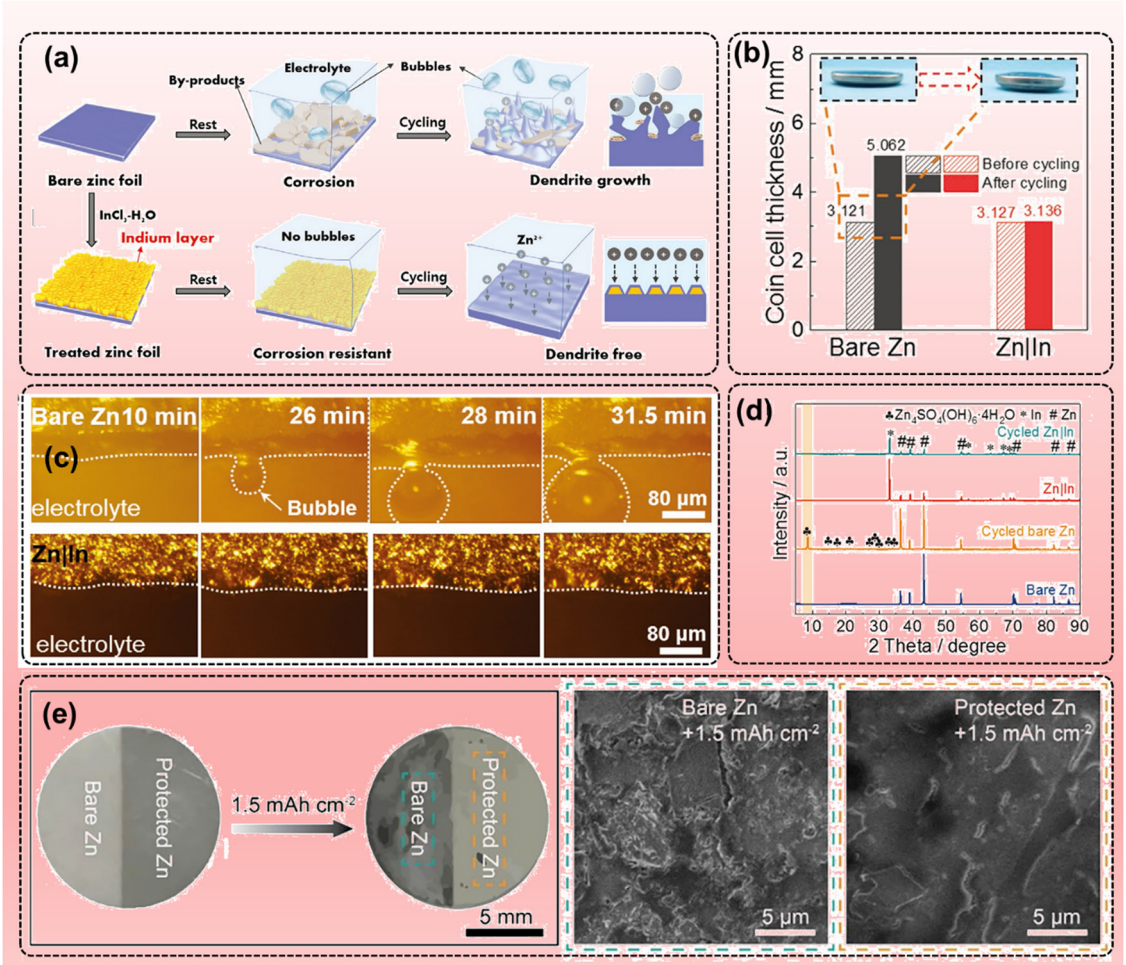

Fig. 10 (a) Schematic of the stripping/plating behaviors of bare Zn and Zn/In anodes. (b) Thickness change of the symmetric cells. (c) Gas evolution characterizations of bare Zn and Zn/In anodes in $ZnSO_4$ electrolytes. (d) XRD patterns of the bare Zn and Zn/In anodes before and after cycling. Reproduced from ref. 143 with permission from John Wiley & Sons, copyright 2020. (e) Digital images and SEM images of Zn anodes with/without an indium layer before and after plating. Reproduced from ref. 120 with permission from Elsevier, copyright 2020.

organic layers that have been previously employed to suppress dendrite growth such as poly(ethylene glycol),[167] polyacrylonitrile,[168] polyanthraquinone,[161] and *in situ* formed quasi-solid electrolyte interface[160,163,169,170] are anticipated to behave well in corrosion inhibition as well. Despite the advantages, the organic coating layer generally presents a large thickness in the range of 30–500 μm, which would reduce the whole volume energy density of the batteries.

3.2 Alloying engineering

Alloying is an exceedingly employed strategy to tune the physicochemical properties such as mechanical strength and corrosion resistance. A multitude of Zn-, Al-, and Mg-based alloys have been reported and great advancements in corrosion inhibition have already been achieved.[112,128,171–180] The corrosion inhibition effect significantly depends on the type and doping amount of alloying elements. This section will summarize and discuss the corrosion inhibition effects and mechanisms of various alloying elements.

Generally, the HER is suppressed on metals such as Pb, Cd, In, Hg, Bi, and Sn. It is anticipated that introducing these metallic elements into the base metal may give rise to increased HER overpotentials, thereby reducing the corrosion rates (Fig. 12a). For instance, Zn–Bi alloys were proven to present a much lower corrosion rate than pure Zn anode in KOH electrolytes.[181,182] It is also reported that Al–Zn, Al–In, and Al–Sn alloys exhibit a lower corrosion potential than the pure Al anode in alkaline electrolytes due to their higher HER overpotentials.[177,183,184] Nonetheless, the superfluous addition of these alloying elements will accelerate the corrosion reactions of the matrix metals. Once the content of alloying elements exceeds its solubility in parent metals, the segregative phases will be formed, which may act as the cathodic sides and accelerate the corrosion reactions at the grain boundaries.[185]

Some more chemically reactive elements were also employed as sacrificial agents to protect parent metals from corrosion (Fig. 12b). In this aspect, a galvanic cell will be assembled with an alloying agent as the anode, by which the base metals are protected.[172] Take Mg as an example: a small amount of Mg can protect the Al matrix from corrosion due to both the increased

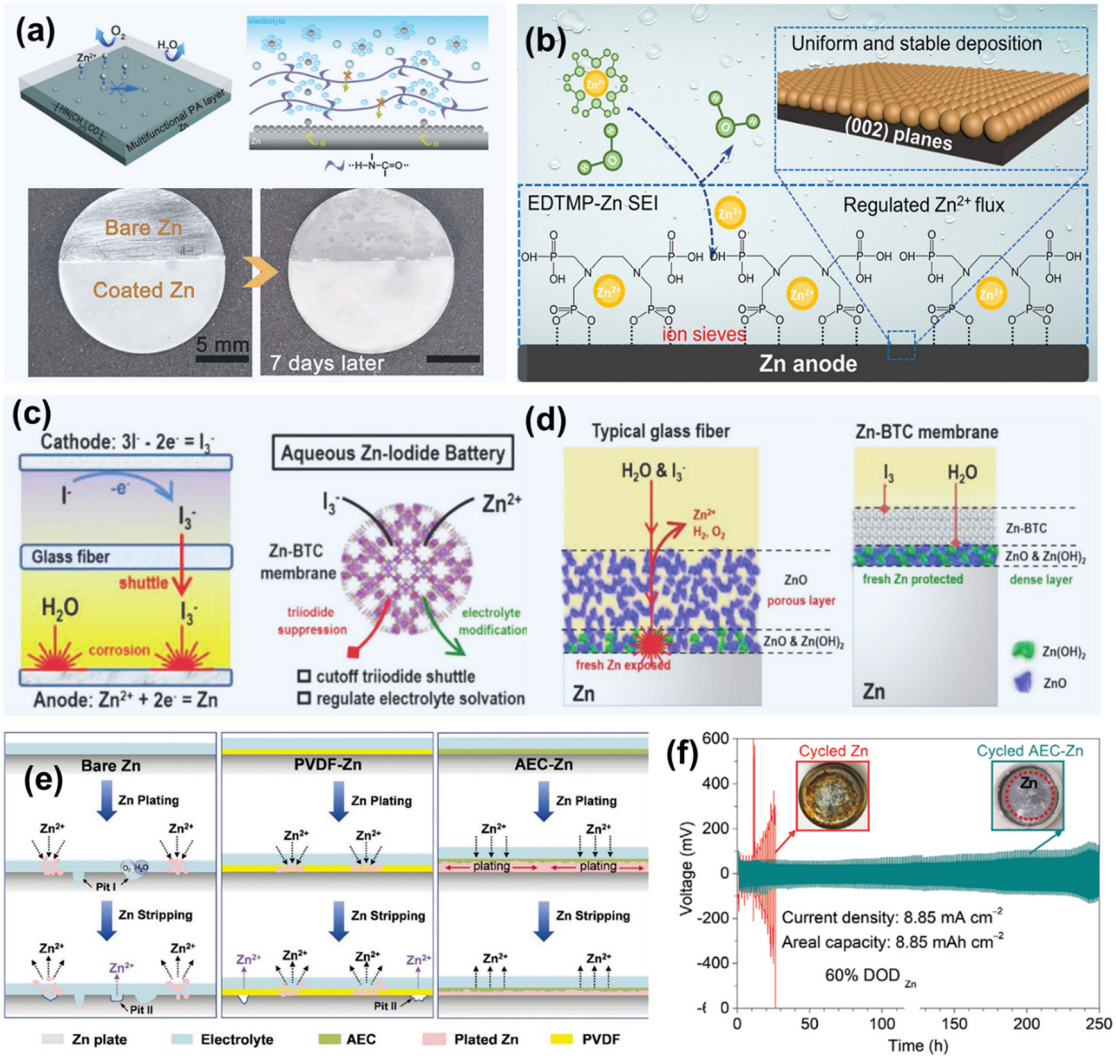

Fig. 11 (a) Schematic of a PA layer for corrosion inhibition, and optical images of Zn electrodes with/without the PA layer. Reproduced from ref. 123 with permission from the Royal Society of Chemistry, copyright 2019. (b) Schematic illustration of the Zn deposition behavior on EDTMP15-Zn@Zn. Reproduced from ref. 163 with permission from John Wiley & Sons, copyright 2024. (c) Schematic of Zn–I_2 batteries with a glass fiber separator and a MOF-based separator. (d) Component illustration at the electrolyte/electrode interfaces after corrosion process. Reproduced from ref. 49 with permission from John Wiley & Sons, copyright 2020. (e) Schematic of Zn plating/stripping processes for bare Zn, PVDF-Zn, and anti-corrosion elastic constraint-protected Zn electrode. (f) Comparison of the cycling stability and optical images of the cells after cycling. Reproduced from ref. 122 with permission from John Wiley & Sons, copyright 2020.

HER overpotential and sacrificial anodic protection.[172] However, this strategy is not suitable for Mg metals due to its relatively reactive nature and low equilibrium potential.

In addition, the alloying elements may influence the corrosion products and affect the formation of passivation films (Fig. 12c). According to reports, the Zn addition to Al anode promoted the formation of two-type Zn oxidation films, including a porous $Zn(OH)_2$ layer and a protective ZnO layer.[191] These layers were more protective than the $Al(OH)_3$ layer in alkaline electrolytes and suppressed the Al corrosion. However, this protective layer will also reduce the charge/discharge efficiency due to its passivation effect. Adding Al into the Mg anode led to the formation of $Mg_xAl(OH)_{2x+2}Cl$ in the NaCl electrolyte, promoting the peel-off of $Mg(OH)_2$ products and thereby reducing the NDE.[192] A low concentration of alloying agents cannot affect the passivation film. In contrast, a large amount of alloying agents will promote the formation of the secondary phase and accelerate the corrosion reactions.

Fig. 12d exhibits the most reported single-atom catalysts for HERs, suggesting that these elements have lower HER overpotentials. Therefore, the other metallic elements such as Bi, Hg, and In in the periodic table can potentially suppress the HER and can be alloyed into metallic anodes for corrosion inhibition. Although these elements have already been confirmed to be effective in corrosion inhibitions (Fig. 12e), there is no criterion for the amount of alloying elements. The effects of alloying elements vary a lot in different research studies. A standard evaluation methodology should be established to examine the corrosion inhibition efficiency of various alloying elements accurately.

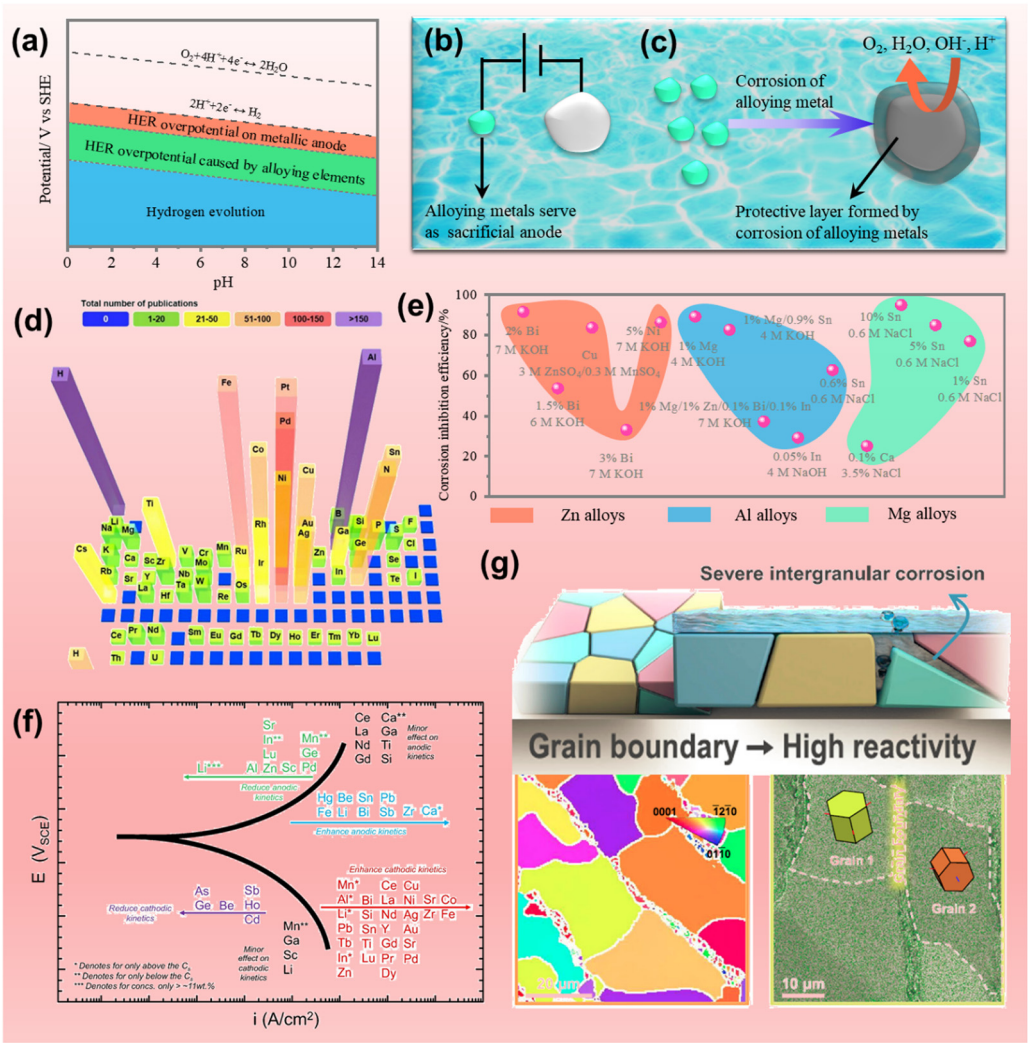

Fig. 12 Schematic of corrosion inhibition mechanisms of alloying elements: (a) increasing HER overpotential, (b) sacrificial anode protection, and (c) formation of the protective layer. (d) Exhibition of mostly reported HER catalysts in the periodic table. Reproduced from ref. 186 with permission from the American Chemical Society, copyright 2020. (e) Corrosion inhibition efficiency of common alloying elements in Zn-, Al-, and Mg-alloys. Reproduced from ref. 8, 171, 172, 185 and 187–189. (f) Schematic of the electrochemical impacts of alloying elements in Mg alloys; Cs refers to solid solubility. Reproduced from ref. 190 with permission from Elsevier, copyright 2017. (g) Schematic of the grain boundary engineering, EBSD IPF mapping of Zn–Ti alloy, and SEM-EDS mapping of Zn–Ti alloy. Reproduced from ref. 177 with permission from Nature Publishing Group, copyright 2023.

Notably, the alloying engineering in Mg anodes is more complicated due to the reactive nature of Mg. Most of the elements manifest limited solubility in crystalline Mg and give rather minimal changes to the corrosion potential of Mg alloys. On the one hand, alloying elements with a higher HER overpotential may be beneficial in slowing down Mg corrosion. On the other hand, the presence of a secondary phase will accelerate the dissolution of neighboring Mg. Nearly all intermetallic particles, except Mg_2Ca, are thought to have more noble corrosive potentials than pure Mg, suggesting that they will act as cathodic sides of the galvanic cells and promote Mg dissolution.[193] The effect of alloying engineering on Mg anode is the net result of the above-mentioned aspects, which the polarization curves can illustrate. From the dynamic polarization curves of various binary Mg-alloys, the E_{corr} value shifts to more positive values and the cathodic current densities increase for all alloys.[194] The electrochemical impacts of alloying elements in Mg have been summarized in a previous report (Fig. 12f).[190] Alloying metal impurities will enrich the surface of the Mg matrix during the corrosion process, acting as a local cathode and enhancing the cathodic HER kinetics. Though some reports state that alloying elements such as Al, Zn, Ca, and In positively affect Mg corrosion inhibition, the improvements should be ascribed to the refined grain or secondary phase morphologies rather than to the chemistry effect.[98,190,195] Fig. 12f also demonstrates that only specific elements such as As, Sb, and Ge from groups 14 and 15 can reduce the cathodic reaction kinetics due to their electrocatalytic poisoning effect toward the HER.[196,197]

The secondary phase formed by alloying elements and base metals plays a vital role in corrosion inhibition. Grain boundaries (GBs) are important structural elements that link grains in

polycrystalline metals and are more reactive than crystallographic planes respectively. As a result, significant intergranular corrosion sometimes results from localized corrosion that starts at GBs with high corrosion susceptibility and subsequently spreads to the deep or inside grains. Take Mg–Ca alloy as an example: corrosion preferentially occurred along the GBs due to the presence of Mg_2Ca.[98] As the secondary Mg_2Ca is not continuous, the dissolution of Mg developed to the interiors of the Mg matrix, leading to shallow but spacious cracks. Once the cracks connect, the Mg grains detach from the bulk anode, resulting in low utilization. Tuning the grain boundary property or the bulk phase structure is an effective strategy to reduce corrosion.[177,198–200] For example, constructing a Zn–Ti dual-phase alloy can alter the GBs of metallic Zn by forming Ti-containing intermetallic compounds that are thermodynamically stabilized at GBs (Fig. 12g). The HER-induced corrosion was efficiently suppressed regardless of aging or extended cycling. Larger grain sizes and fewer grain boundaries in the metallic electrode typically present better corrosion resistance.[199] Through aging treatment or rolling processing, the separated phase distribution, grain boundary, and grain size can be modified.[76,111,177,199]

Alloying engineering has been proven to be an effective strategy for suppressing the corrosion of metals, and recent achievements in alloying engineering of metallic anodes are summarized in Table 2. The proportion of alloying elements is determinative of the corrosion inhibition efficiency. Though great advances have been achieved, insights into the mechanistic aspect of corrosion inhibition require more research, especially in the presence of multiple alloying elements. A standard evolution methodology should be established to examine the corrosion inhibition efficiency of various alloying elements accurately.

3.3 Electrolyte engineering

Electrolyte engineering refers to employing additives, designing gel or solid-state electrolytes, and developing hybrid electrolytes, which aim to suppress the cathodic HER. These approaches give rise to reduced HER active centers or sluggish HER kinetics, thereby decreasing the self-corrosion of metallic anodes.

3.3.1 Corrosion inhibitor. Corrosion inhibitors are widely used to prevent the metallic anode from corrosion in aqueous electrolytes. Broadly speaking, corrosion inhibitors can be divided into interface and inter-phase types. Interface-type corrosion inhibitors refer to those that can be absorbed on the metal surface to suppress the corrosion reactions. Inter-phase-type corrosion inhibitors can react with metal ions or corrosion products on the surface and generate a protective layer.[11] For instance, NaF or Na_2SiO_3 additives can react with Mg^{2+} and produce passive MgF_2 and $MgSiO_3$ layers on the Mg surface.[109,208] Upon formation, the passivation layer will serve as a protective layer, preventing corrosion of the anode. The battery kinetics would be constrained, however, if this passivation layer were not a good ionic conductor. Pitting corrosion may also occur when the passivation film is not intact. Interface-type corrosion inhibitors are more frequently employed in AMBs. This kind of corrosion inhibitor is typically an organic compound that can be absorbed onto the metal surface. The effectiveness of the organic inhibitors depends on their adsorption rates and covering capabilities on metal surfaces. Consequently, a lot of organic compounds with suitable structures containing heteroatoms such as P, S, N, or O have been widely used as corrosion inhibitors (Fig. 13a),[209,210] which are absorbed onto the surface by a lone pair of electrons from the heteroatoms.[211] Together with the heteroatoms, aromatic rings, heterocyclic rings, or alkyl groups in the compounds may also

Table 2 Corrosion inhibition performances of various alloying elements

	Anode	Electrolyte	Alloying elements	Corrosion inhibition efficiency	Battery performance	Ref.
1	Zn	7 M KOH	2% Bi	91.5%	Slightly reduced capacity	187
2	Zn	6 M KOH	1.5% Bi	53.8%	Lower cut-off voltage, enhanced capacity	171
3	Zn	3 M $ZnSO_4$/ 0.3 M $MnSO_4$	Cu	83.7%	Prolonged cycling life	8
4	Zn	7 M KOH	3% Bi	33.2%	—	201
5	Zn	7 M KOH	5% Ni	86.3%	—	202
6	Al	4 M KOH	1% Mg	89.2%	Enhanced Al utilization and capacity	172
7	Al	4 M KOH	1% Mg/0.9% Sn	82.7%	Enhanced Al utilization and capacity	172
8	Al	7 M KOH	1% Mg/1% Zn/ 0.1% Bi/0.1% In	37.3%	Higher cell potential and Al utilization	203
9	Al	4 M NaOH	0.05% In	29.2%	Enhanced capacity and anodic efficiency	204
10	Al	0.6 M NaCl	0.6% Sn	62.7%	—	188
11	Al	1 M NaOH	Cu	Higher corrosion resistance	Higher discharge potential and Al efficiency	205
12	Mg	3.5% NaCl	9% Al/2.5% Pb	Higher E_{corr} and lower I_{corr}	Enhanced discharge potential and Al utilization efficiency	192
13	Mg	0.1 M NaCl	1% Zn	More serve corrosion	—	112
14	Mg	0.1 M NaCl	0.3% Ge	Suppress HER	—	112
15	Mg	0.1 M NaCl	Bi, Ge, Pb, Sb, Sn	Improved corrosion resistance	—	196
16	Mg	3.5% NaCl	0.1% Ca	25.1%	Higher cell voltage and energy density	185
17	Mg	0.6 M NaCl	3–9% Al	Decreased self-corrosion	Higher operating voltage and capacity	206
18	Mg	0.6 M NaCl	3–9% Al	Lower I_{corr}	Higher Mg utilization	195
19	Mg	0.1 M NaCl	0.37% As	An order of magnitude lower H_2 evolution	—	197
20	Mg	3.5% NaCl	1–3% Sn	Reduced I_{corr} and H_2 evolution	—	207
21	Mg	0.6 M NaCl	1%, 5%, 10% Sn	77%, 85%, 95%	—	189

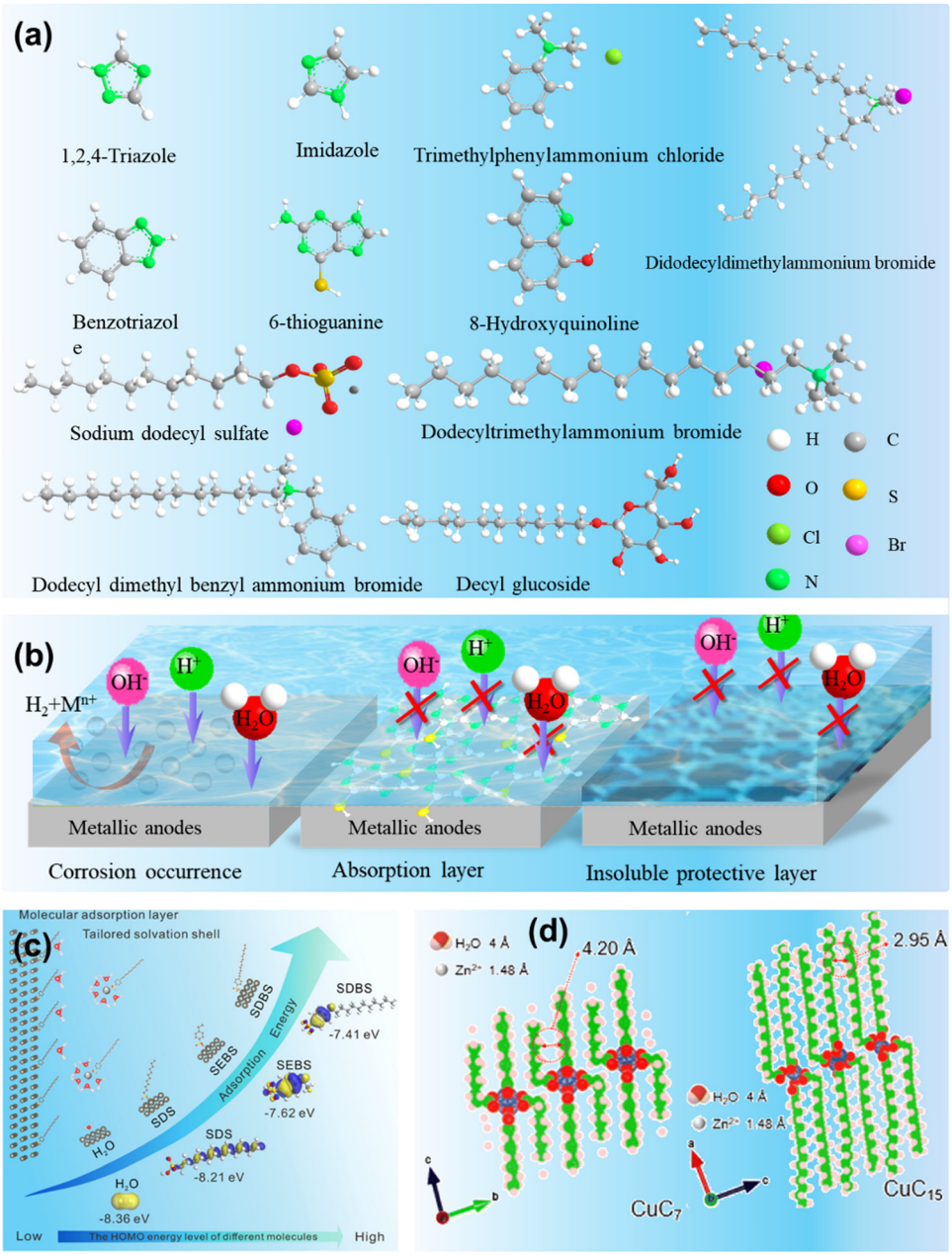

Fig. 13 (a) Molecular structures of commonly used organic inhibitors. (b) Schematic of the corrosion inhibition mechanism of organic inhibitors. (c) HOMO energy level of different molecules. Reproduced from ref. 212 with permission from Elsevier, copyright 2024. (d) Channel size illustration of CuC_7 and CuC_{15} with different alkyl chain lengths. Reproduced from ref. 213 with permission from the Royal Society of Chemistry, copyright 2024.

enhance the adsorption.[209,211] The standard free energy of adsorption (ΔG_{ads}) can be calculated as follows:

$$\Delta G_{ads} = -RT\ln(55.5K_{ads}) \quad (3.1)$$

where 55.5 mol L^{-1} is the molar concentration of water, R is the universal gas constant, T is the absolute temperature, and K_{ads} is the equilibrium constant for the adsorption process. If the ΔG_{ads} value is in the range from 0 to −20 kJ mol^{-1}, the inhibitor can be spontaneously adsorbed onto the metal surface by physisorption. A value more negative than −40 kJ mol^{-1} implies the chemisorption of inhibitors. By adhering to metal surfaces, inhibitor molecules occupy the active sites, suppressing the cathodic HER, thus providing corrosion protection (Fig. 13b).

Organic inhibitors may either dynamically generate an absorption layer on the surface or produce a protective layer with metal ions (Fig. 13b).[214,215] Take SDBS as an example: it is mainly composed of hydrophilic groups and hydrophobic alkyl chains.[216] The highest occupied molecular orbital exclusively distributes in the sulfonate anion region, which exhibits a negative electrostatic potential and helps to interact with the metal surface (Fig. 13c).[212,217] While the polar groups help inhibitors to adsorb onto the metal surface, the non-polar part

(such as the hydrocarbon chain) is forced towards the aqueous solution side due to its electrophilic reactivity. These tails repel the water and aggressive molecules away from the surface and thus decrease their corrosion effects.

Efficiency in inhibiting corrosion is primarily dependent on the completeness of the protective or absorption layer, which is closely tied to inhibitor concentrations and intrinsic characteristics. Increasing the inhibitor concentration to the critical micelle concentration value gradually increases, and full coverage can finally be achieved.[218] The adsorption of inhibitors on the metal surface typically obeys either Langmuir isotherm or Freundlich isotherm,[209,219] which can be expressed as follows:

$$\frac{C}{\eta} = \frac{1}{K_{\text{ads}}} + C \tag{3.2}$$

$$\log(\eta) = \log K_{\text{F}} + \frac{1}{n}\log C \tag{3.3}$$

where C is the inhibitor concentration, η is the surface coverage degree, K_{F} is the Freundlich equilibrium constant, and n is the empirical constant. η can be calculated from the corrosion current density or charge transfer resistance using the following equations:[220]

$$\eta = \frac{R_{\text{CT}} - R'_{\text{CT}}}{R_{\text{CT}}} \times 100\% \tag{3.4}$$

$$\eta = \frac{I_{\text{corr}} - I'_{\text{corr}}}{I_{\text{corr}}} \times 100\% \tag{3.5}$$

where R_{ct} and R'_{CT} are the charge transfer resistances of the metallic anodes in electrolytes with and without inhibitors, respectively. I_{corr} and I'_{corr} are the corrosion current densities of the metallic anodes in electrolytes with and without inhibitors. Besides, the molecules containing the carbonyl group, carboxyl group, amino group, benzene rings, heterocyclic ring, or more heteroatoms should present higher corrosion inhibition efficiency due to the improved absorption interaction (Fig. 13a).[39,219,220] Moreover, the alkyl chain length significantly influences the corrosion efficiency. Too short an alkyl chain may make it hard to form an intact film, while a too-long alkyl chain might result in a loose adsorbed layer.[221] The film formed by a longer alkyl chain presents a smaller channel size and higher water molecular/Zn^{2+} ion insertion energies (Fig. 13d).[213] Lastly, the effectiveness of corrosion inhibition also depends on the inhibitor's capacity to participate in the solvation shell. Solvated water rather than free water is more likely to be the origin of H_2 evolution and "parasitic" side reactions.[222] By substituting solvated water molecules, certain organic compounds can participate in the solvation structure of Zn ions, lowering the possibility of corrosion at the Zn electrode/electrolyte interface.[214,223–228]

Combining different inhibitors gives rise to a higher corrosion inhibition efficiency, thanks to their synergistic effect.[220,229] On the one hand, the branched and linear structures in organic inhibitors result in a more integrated protective layer. Inhibitors with a benzene ring or a heterocyclic ring exhibit strong adhesion on the metal surface (Fig. 14a). However, the as-formed absorption layer or protective layer may be loose and incomplete due to the steric effect of a highly branched structure. Introducing linear organic inhibitors such as PEG into an imidazole-containing system contributed to an intact protection film, improving the corrosion inhibition efficiency.[220] On the other hand, organic and inorganic composite inhibitors may present better corrosion protection performance. Some inorganic corrosion inhibitors such as ZnO and K_2SnO_3 endow *in situ* deposition of Zn or Sn layers on the anode surface.[56,230,231] Together with physical barrier actions, the increased HER overpotential by this kind of *in situ* formed metallic layers contributes to an enhanced corrosion inhibition efficiency. The inhibitors may also have significant influences on the solvation shell structure. For example, the radius of the hydrated zinc complex (4.30 Å) is approximately five times as large as that of the bare zinc cation itself (0.83 Å) (Fig. 14b). The hydration shells are mainly occupied by the coordinating water molecules. By selecting redox-inactive cations with appropriate coulombic repulsion energy and solvation rigidity (Fig. 14c), the solvation shell structure has been modified, leading to markedly improved cyclability.[223]

Recent advances in corrosion inhibitors for AMBs are summarized in Fig. 14d and Table 3. Though various inhibitors have already achieved remarkable corrosion inhibitions, further efforts need to be made to clarify their mechanisms. Especially for inorganic inhibitors, it is yet unknown how to restrict active centers for cathodic HERs or anodic dissolution, which impedes the development of effective corrosion inhibitors in the future. More emphasis should be paid to the adsorption characteristics of inorganic inhibitors, which impact the corrosion inhibitor efficiency. Since corrosion inhibitors may alter metallic anodes' reversible stripping/plating behaviors, their impact on battery kinetics should also attract greater attention.

3.3.2 Quasi-solid electrolyte design. Compared with aqueous electrolytes, hydrogel electrolytes are widely accepted owing to their high ionic conductivity and less free water, which may reduce the parasitic HER on metal surfaces.[267–273] They are typically hydrophilic crosslinked polymers and can immobilize water molecules due to the polymer's strong interaction between water and functional groups. In the illustration of sodium polyacrylate (PANa), OH^- and H_2O connected with PANa and cellulose chains, respectively, *via* hydrogen bonds confined their diffusion towards the metal surface (Fig. 15a).[274] A polyacrylamide (PAM)-based electrolyte was also developed, in which strong hydrogen-bonding interactions were formed among water, ethylene glycol (EG), and PAM chains (Fig. 15b). In addition, the carboxyl and hydroxyl side groups in alginate could also form hydrogen bonding interactions with the molecules of EG and water, which potentially greatly affected the immobilization of free water.[275] Other hydrogel electrolytes such as polyacrylic acid-based alkaline gel electrolytes,[276] polyvinyl alcohol-based electrolytes,[19] poly[2-(methacryloyloxy)ethyl]dimethyl-(3-sulfopropyl)-based hydrogel electrolytes[277] have also been proven to be beneficial for the corrosion inhibition of metallic anodes. It is anticipated that the polymer hydrogels applied in dendrite suppression, including Zn-alginate/PAM,[278–280] sulfobetaine,[281] Pluronic,[282] gelatin,[283,284] and xanthan,[285] should perform well in corrosion inhibition as well.

Gel electrolytes prepared by direct gelatinization of aqueous electrolytes were also reported, which can be doped with

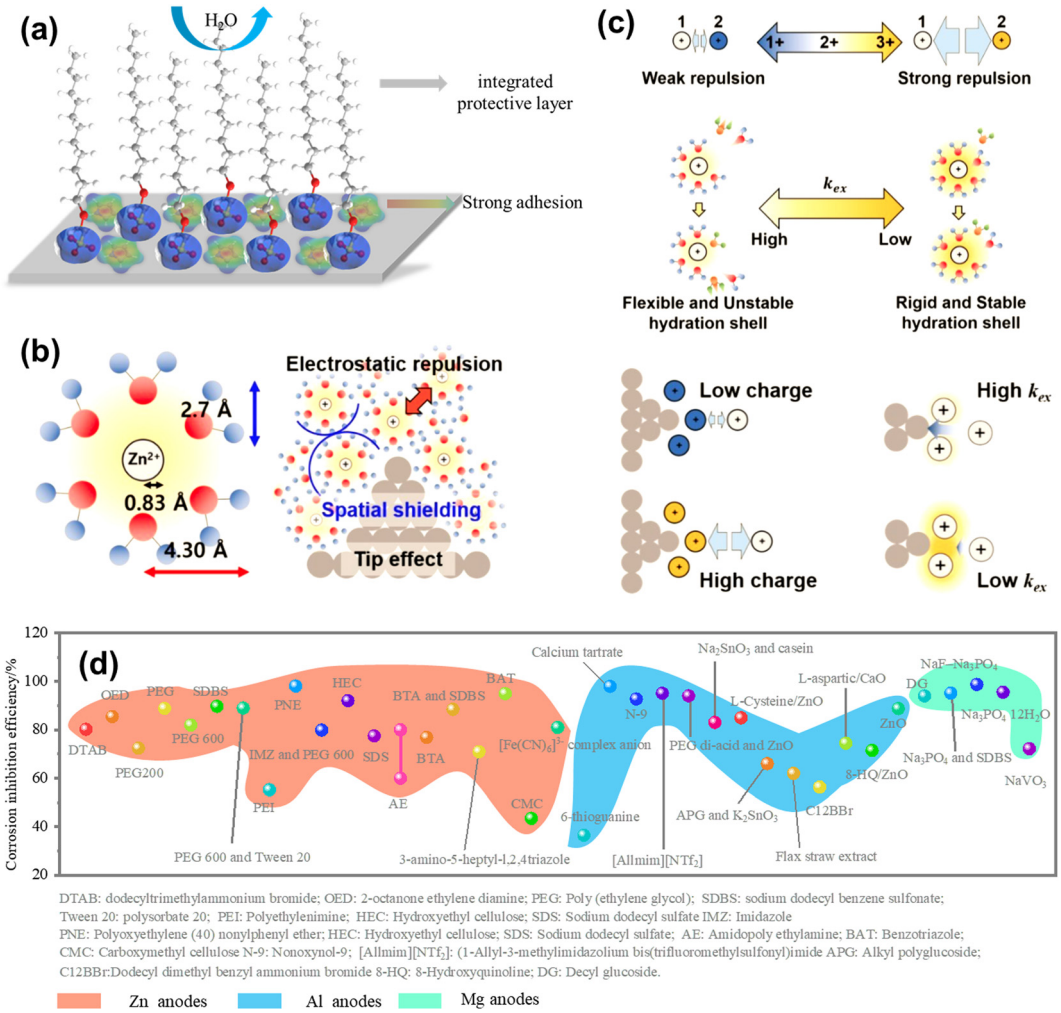

DTAB: dodecyltrimethylammonium bromide; OED: 2-octanone ethylene diamine; PEG: Poly (ethylene glycol); SDBS: sodium dodecyl benzene sulfonate; Tween 20: polysorbate 20; PEI: Polyethylenimine; HEC: Hydroxyethyl cellulose; SDS: Sodium dodecyl sulfate IMZ: Imidazole PNE: Polyoxyethylene (40) nonylphenyl ether; HEC: Hydroxyethyl cellulose; SDS: Sodium dodecyl sulfate; AE: Amidopoly ethylamine; BAT: Benzotriazole; CMC: Carboxymethyl cellulose N-9: Nonoxynol-9; [Allmim][NTf_2]: (1-Allyl-3-methylimidazolium bis(trifluoromethylsulfonyl)imide APG: Alkyl polyglucoside; C12BBr:Dodecyl dimethyl benzyl ammonium bromide 8-HQ: 8-Hydroxyquinoline; DG: Decyl glucoside.

Fig. 14 (a) Schematic of the absorption for different inhibitors with a linear alkyl chain or a heterocyclic ring. Effect of key parameters of redox-inactive cationic additives on tip blocking: (b) physical dimensions of a hydrated Zn ion and scheme of the tip effect. (c) Illustration of the charge and the water exchange rate modifications by redox-inactive cations. Reproduced from ref. 223 with permission from John Wiley & Sons, copyright 2022. (d) Corrosion inhibition efficiencies of various corrosion inhibitors for Zn-, Al-, and Mg-based anodes.

corrosion inhibitors such as lignin, pyrazole, Pb^{2+}, and polyethylene glycol.[287–289] The combination of water immobilization and corrosion inhibitors gives rise to good corrosion inhibition efficiency.

Water-in-salt (WIS) electrolytes contain more excellent dissolved salt than water, in which all water molecules are a part of ion solvation shells and no free water is present. This type of super-concentrated electrolyte has been applied in various aqueous batteries due to its expanded electrochemical stability window.[290–292] As the water molecules are all immobilized by an electrolyte salt, the corrosion reaction of metallic anode and cathodic HERs in WIS electrolytes is suppressed. For example, a WIS electrolyte containing 16 M potassium acetate (KOAc) and 4 M KOH was developed to suppress Al corrosion in Al–air batteries.[286] With the gradual increase in the amount of KOAc, acetate anions cooperated with the sheaths of K^+, and more water molecules were involved in binding interactions in solvation sheaths (Fig. 15c). Fewer water molecules adsorbed onto the Al anode surface due to the greatly reduced free water. Therefore, the HER was significantly inhibited and Al anode corrosion was obviously reduced.

3.4 Other strategies

Some other promising strategies, ranging from tuning the exposure crystal plane to rationally designing the battery configurations, have also been developed to address the corrosion issue of metallic anode. Recently, some researchers have proposed that the corrosion behavior of metallic anodes is highly related to their crystallographic planes. Zn corrosion is mainly prone to occur in the (100) plane, while it is not likely to happen on the (002) plane.[2,159,293,294] Electrodeposition of Zn in the presence of various additives, such as indium sulfate, tin oxide, and boric acid, will give rise to different surface textures and crystallographic orientations. Among different additives, boric acid helps to produce Zn with the dominance of the (002) surface, which has a higher resistance to dendrite formation and corrosion. Similar phenomena were also detected in the Al anode, which suggested that the (001) plane has good corrosion resistance and the (110)

Table 3 Corrosion inhibition efficiency of various inhibitors

	Anode	Electrolyte	Corrosion inhibitor	Corrosion inhibition efficiency	Battery performance	Ref.
1	Zn	7 M KOH	DTAB	80.2%	—	232
2	Zn	6 M KOH	OED	85.5%	Both improved capacity and stability	233
3	Zn	1 M Li_2SO_4/ 2 M $ZnSO_4$	PEG200	72.4%	32% improvement in capacity	167
4	Zn	9.5 M KOH	PEG	88.9%	—	218
5	Zn	8.5 M KOH	PEG600	82%	—	234
6	Zn	26% NH_4Cl	SDBS	89.7%	—	217
7	Zn	3 M KOH	PEG 600 and Tween 20	89%	33% improvement in capacity	235
8	Zn	6 M KOH	PEI	55.2%	Improved stability	236
9	Zn	7 M KOH	PNE	98.1%	Improved capacity	211
10	Zn	3 M KOH	IMZ and PEG600	79.9%	—	220
11	Zn	26% NH_4Cl	HEC	92.07%	—	209
12	Zn	7 M KOH	SDS	77.5%	24% improvement in capacity	237
13	Zn	$ZnCl_2$/NH_4Cl	AE	60–80%	—	219
14	Zn	6 M KOH	BAT	76.9%	31.9% improvement in capacity	238
15	Zn	6 M KOH	BTA and SDBS	88.5%	34.3% improvement of capacity	238
16	Zn	2 M $ZnSO_4$	Sodium anthraquinone-2-sulfonate	Reduced corrosion	Longer cycle life	239
17	Zn	1 M $ZnSO_4$	1,2-Butanediol	Lower I_{corr}	5–20 fold zinc cyclability enhancement	240
18	Zn	6 M KOH	CMC	43.5%	—	241
19	Zn	2 M $ZnSO_4$	Trehalose	Lower I_{corr} and higher E_{corr}	two times enhancement in cycle stability	242
20	Zn	2 M $ZnSO_4$	Zinc pyrrolidone carboxylate	More positive E_{corr}	Enhanced cycle stability	243
21	Zn	2 M $ZnSO_4$	Nitrilotriacetic acid	Much lower I_{corr}	regulate the Zn deposition	244
22	Zn	2 M $ZnSO_4$	Imidazo[1,2-*b*]pyridazine	lower I_{corr}	Better reversibility	245
23	Zn	2 M $ZnSO_4$	Pyrimidine	lower I_{corr}	Accelerating the desolvation process	246
24	Zn	1 M $Zn(OAc)_2$	Ethylene glycol	15 times lower corrosion rate	Higher capacity retention	247
25	Zn	3 M $Zn(OTf)_2$	Urea/LiOAc	Far less I_{corr}	highly reversible plating/stripping	229
26	Zn	2 M $ZnSO_4$	Zinc acetylacetonate	Lower I_{corr} and higher E_{corr}	10 times longer cyclability	248
27	Zn	2 M $ZnSO_4$	Ammonium hydroxide	Lower HER potential	much better cyclic stability	249
28	Zn	2 M $ZnSO_4$	Sc^{3+} additive	Higher corrosion resistance	5–8 fold cycle life	250
29	Zn	2 M $ZnSO_4$	Sodium 3,3′-dithiodipropane sulfonate	Lower I_{corr} and higher E_{corr}	Extended cycle life	251
30	Zn	2 M $ZnSO_4$	C5SeCN	Reduced I_{corr}	Improved Zn utilization	252
31	Zn	2 M $ZnSO_4$	Protonated triglycine	Increased E_{corr}	Prolonged operation life	253
32	Al	4 M NaOH	6-thioguanine	36.56%	Enhanced Al utilization: from 38.5% to 74.6%	254
33	Al	4 M NaOH	N-9	92.8%	15–25% improvement of capacity	255
34	Al	4 M NaOH	[Allmim][NTf2]	95.1%	48.5% improvements in capacity	256
35	Al	4 M KOH	APG and K_2SnO_3	94.1%	250% improvements in capacity	56
36	Al	4 M NaOH	Na_2SnO_3 and casein	83.1%	89.3% improvements in capacity	230
37	Al	4 M NaOH	L-Cysteine/ZnO	85%	Enhanced Al utilization: from 7.4% to 19.9%	257
38	Al	5 M KOH	PEG di-acid and ZnO	66%	57.3% improvements in capacity	258
39	Al	5 M KOH	Flax straw extract	62%	23.5% improvements in capacity	259
40	Al	4 M NaOH	$C_{12}BBr$	56.3%	96% improvements in capacity	260
41	Al	4 M NaOH	L-Aspartic/CaO	74.5%	—	261
42	Al	4 M NaOH	8-HQ/ZnO	71.5%	Enhanced Al utilization: from 56.2% to 70.3%	262
43	Mg	3.5% NaCl	DG	94%	Enhanced Mg utilization: from 39.4% to 89.7%	263
44	Mg	3.5% NaCl	Na_3PO_4 and SDBS	95.2%	Enhanced Mg utilization: from 44.1% to 49.1%	264
45	Mg	2 M $MgSO_4$/ 2 M $Mg(NO_3)_2$	NaF–Na_3PO_4	98.8%	57% improvement in capacity	208
46	Mg	0.6 M NaCl	$Na_3PO_4{\cdot}12H_2O$	95.6%	25% decrease of capacity	265
47	Mg	0.6 M NaCl	$NaVO_3$	72.2%	6.7% improvement in capacity	265
58	Al	10 M LiTFSI	Hydrolyzation type-anodic additive	Three orders lower I_{corr}	Improved cycling stability and initial efficiency	266

plane is more sensitive.[295,296] Experimental results confirmed that the hydrogen evolution rate and corrosion current density follow the order of (001) single crystal < (111) single crystal < (110) single crystal < polycrystalline. Therefore, tuning the crystallographic planes might be an effective way to suppress both dendrite formation and corrosion.

Rational battery configuration may also help to remit the corrosion issue of metallic anodes. Displacing electrolytes from the electrode with a non-conductive oil during battery standby was developed in a primary Al–air battery to suppress the open-circuit corrosion.[297] However, this battery design still has self-corrosion during the discharging process. A magnesium-moisture battery without additional electrolytes was proposed, in which metallic Mg served as the anode and a semi-conducting polyaniline (PANI) foam served as the cathode (Fig. 16a). Trace-absorbed water causes Mg corrosion, which generates Mg^{2+} ions and electrons. Because of the much lower electronic conductivity than the ionic conductivity of PANI, the electrons have to run into an external circuit due to the depolarization process.[298] Although the discharge current is not high, this battery configuration prevented the energy loss caused by corrosion.

Another approach to raising the efficiency of the metallic anode is collecting the hydrogen produced by the parasitic cathodic reactions during corrosion. Devices combined with

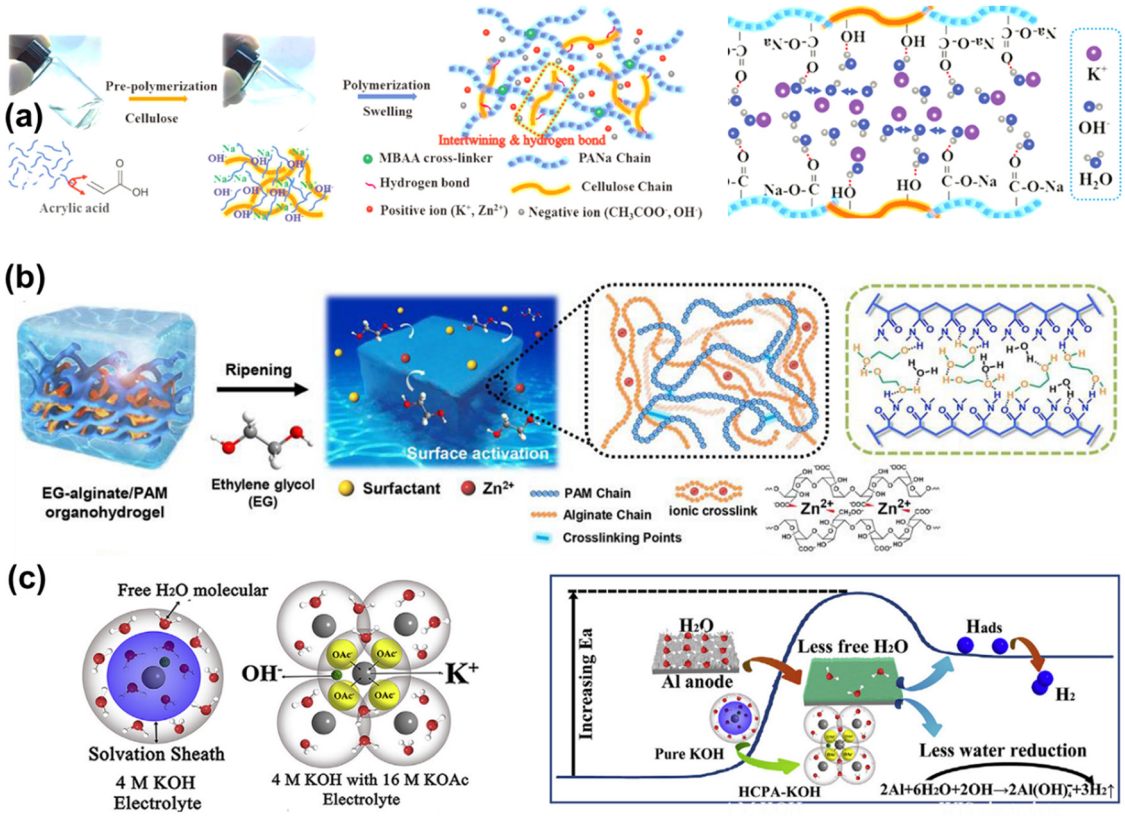

Fig. 15 (a) Synthetic procedure of the PANa-cellulose hydrogel electrolyte and illustration of entrapped OH^- ions and water in the hydrogel *via* hydrogen bonding. Reproduced from ref. 274 with permission from John Wiley & Sons, copyright 2019. (b) Design principle of PAM-based hydrogel electrolyte and its structural illustration. Reproduced from ref. 275 with permission from John Wiley & Sons, copyright 2019. (c) Schematic of the solvation sheath in different electrolytes and illustrations of reduced water reduction reaction and Al anode corrosion in the WIS electrolyte. Reproduced from ref. 286 with permission from Elsevier, copyright 2020.

electrical energy and chemical energy (H_2 storage) storage systems were developed (Fig. 16b and c).[299,301] Apart from the normal function of the battery, the hydrogen produced during the corrosion can be stored. To effectively collect hydrogen, it should be mentioned that the anode compartment needs to be deoxygenated. A recently reported Zn/Al–CO_2 system may also provide insights into this tactic, which adopted HER as the cathodic reaction to achieve both electrons and H_2 collection.[300] Similarly, the hydrogen produced in the corrosion process was also anticipated to be utilized by this battery system. Although this strategy reduces the side effects caused by corrosion, it is unsuitable for practical battery systems due to their complicated configurations.

The aforementioned review and discussion lead us to the conclusion that the anti-corrosion strategy of the metal anode can be macroscopically divided into two parts: electrode design and electrolyte design. The interfacial protective coating, which has multifunctional characteristics and is customizable, generally prevents the electrolyte from corroding to the metal anode through the physical barrier effect. However, the corrosion inhibition performance of the electrode is heavily dependent on the microstructural characteristics and inherent physicochemical properties of the coating layer, which undoubtedly increases the difficulty and cost of preparation. The alloy anode is easy to prepare on a large scale and has good stability, but alloying engineering requires strict control of the alloy ratio and process to ensure the anode's electrochemical performance. There are still issues with alloy element compatibility and precise phase composition management. Moreover, the introduced inactive competent inevitably decreases the energy density of the battery. The most popular approach in electrolyte design is the introduction of corrosion inhibitors. This approach offers special benefits such easy large-scale preparation, cheapness, and simple operation. However, while choosing additives, it is important to consider if they might cause problems with other battery parts (such as the separator and cathode), which could impact the battery's overall charge/discharge performance. Special attention must be paid to how corrosion inhibitors affect the battery's charge/discharge kinetics in order to prevent lowering the power characteristics.

4. Characterization techniques

Advanced techniques to characterize metallic anode corrosion and the as-proposed protective approaches play a vital role in understanding the corrosion processes and evaluating the corrosion inhibition performance. Electrochemical characterizations,

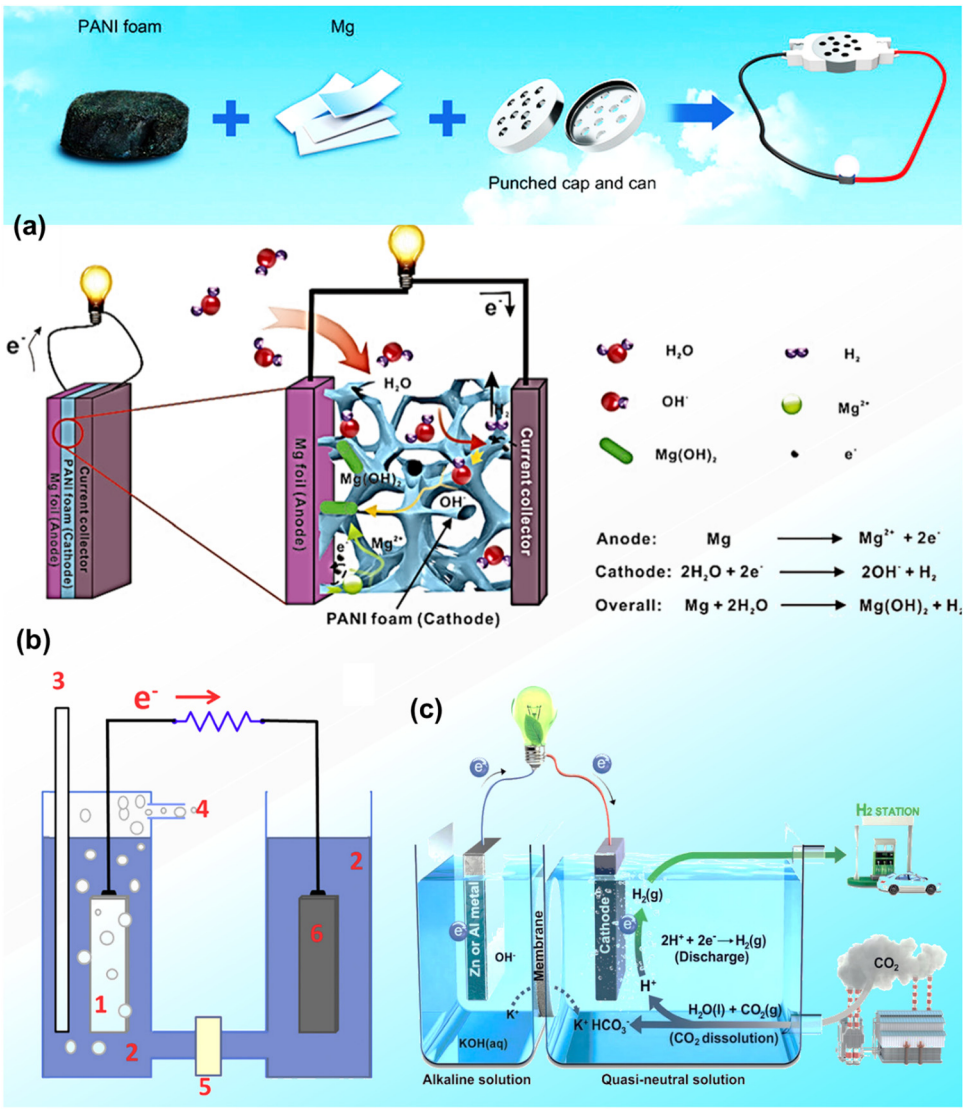

Fig. 16 (a) Schematic of the Mg-PANI foam battery. Reproduced from ref. 298 with permission from John Wiley & Sons, copyright 2015. (b) Schematic of a device combining electrical and chemical storage (1-Al anode; 2-aqueous alkaline electrolyte; 3-introduction of inert gas; 4-H_2 collection; 5-ion-exchange membrane; and 6-cathode); Reproduced from ref. 299 with permission from Elsevier, copyright 2016. (c) Schematic of the aqueous Zn/Al-CO_2 systems. Reproduced from ref. 300 with permission from John Wiley & Sons, copyright 2019.

including polarization curve method, electrochemical impedance spectroscopy (EIS), electrochemical noise (EN), and scanning electrochemical microscopy (SECM), make prominent contributions to corrosion mechanism determination. The formation of byproducts and passivation layers, which have huge impacts on further corrosion and battery performance, can be assessed by various spectroscopic techniques including X-ray diffraction (XRD), X-ray photoelectron spectroscopy (XPS), and Raman spectroscopy. A series of microscopy techniques can visually monitor the morphological evolution of the metallic anode during the corrosion process and long-term battery running.

4.1 Electrochemical techniques

4.1.1 Polarization curves. The polarization curve can be recorded by controlling the voltage or current as independent variables, which is an effective method for analyzing the corrosion reaction kinetics. A series of fundamental parameters including corrosion potential, corrosion current, passivation/pitting potentials, and rate-controlling step can be achieved. The potential for anodic dissolution and cathodic reaction to reach equilibrium is corrosion potential. Currents at the corrosion potential are defined as corrosion currents, which can be directly worked out from the Tafel polarization plot. Relationships between total current density (i_{tot}) and corrosion current density (i_{corr}) can be expressed as follows:[302]

$$i_{tot} = i_a + i_c = i_{corr}\left[\exp\left(\frac{E - E_{corr}}{\beta_a}\right) - \exp\left(\frac{E - E_{corr}}{\beta_c}\right)\right] \quad (4.1)$$

where i_a and i_c are the anodic and cathodic current densities, respectively. β_a and β_c are the Tafel constants of anodic and cathodic branches, respectively.

However, the Tafel plots are easily affected by the passivation process or other redox reactions on the electrode surface, thereby increasing the difficulty of corrosion current measurement. Under this circumstance, linear polarization near E_{corr} provides more accurate information. Corrosion current can be calculated by the slope of the linear polarization curve according to the Stern-Geary equation as follows:[303]

$$i_{corr} = \frac{B}{R_p} \quad (4.2)$$

where B is a constant and R_p is the linear polarization resistance or slope of the linear polarization curve near E_{corr}.

The metal dissolution rate increases during the anodic polarization and the as-produced byproducts may cause electrode passivation. Then, the corrosion current reduces due to the protection of the passivation film until the occurrence of pitting corrosion (Fig. 17a). Therefore, polarization curves can reveal the overall corrosion process and play a significant role in the mechanism study.[11,240,304,305] Corrosion protection performance can also be easily evaluated by polarization curves. For instance, more positive corrosion potential and smaller corrosion current were observed for a Cu alloyed Zn anode, demonstrating good corrosion inhibition efficiency.[8] Another example is that the N9 surfactant caused a marked decrease in cathodic current and slightly impeded the anodic curve, inferring that this corrosion inhibitor is a cathodic inhibitor.[255]

In summary, the polarization curve method is a fundamental technique to obtain corrosion reaction kinetics and describe the overall corrosion behaviors. However, one thing that should be particularly noted is that E_{corr} cannot estimate the corrosion tendency individually. The positive shift of corrosion potential does not always suggest corrosion inhibition behavior, which should be evaluated together with corrosion current.

4.1.2 Electrochemical impedance spectroscopy. EIS is another technique shared in corrosion studies, and it is instantaneous and non-destructive. The EIS can obtain faradic resistance, ion diffusion resistance, and possible capacitance, which provides more information related to the reaction kinetics and the electrode surface.[162,294,306,308,309] Nyquist plots obtained by EIS data help to estimate the corrosion mechanism. An *in situ* EIS measurement has been previously performed to illustrate Mg's corrosion behavior and mechanism.[306] In the initial stage, a single capacitive loop observed at a high frequency corresponds to the faradic resistance. With further corrosion, the increase in the first loop and the appearance of the second loop (Fig. 17b) demonstrate the onset of mass transfer limitations

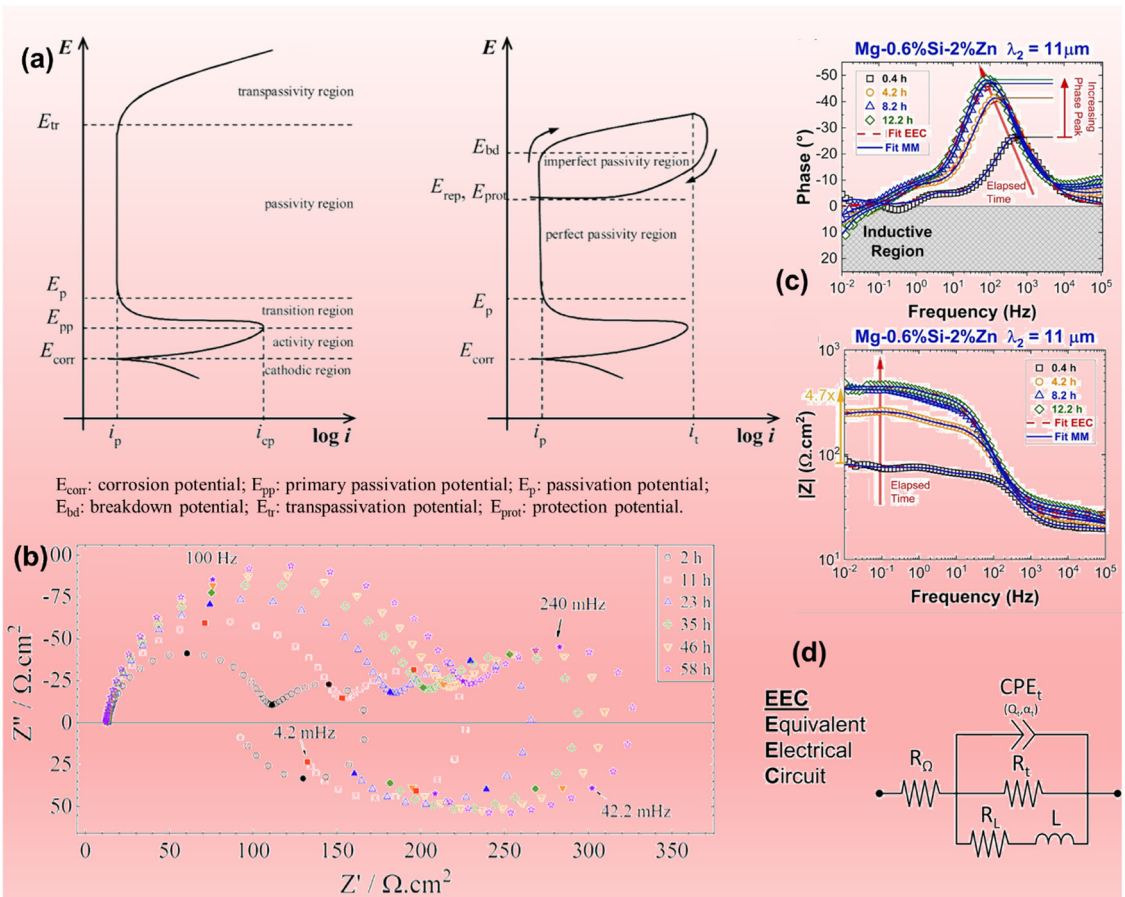

Fig. 17 (a) Schematic of polarization curves. Reproduced from ref. 302 with permission from Elsevier, copyright 2018. (b) *In situ* Nyquist plots of the Mg electrode in Na_2SO_4 electrolytes. Reproduced from ref. 306 with permission from Elsevier, copyright 2019. (c) Bode phase and Bode |*Z*| plots of the Mg–0.6%Si–2%Zn alloys. (d) Equivalent electrical circuit. Reproduced from ref. 307 with permission from Elsevier, copyright 2024.

caused by the porous byproducts. The low-frequency inductive loop is ascribed to the relaxation of adsorbed intermediates. Coating protection performance can also be assessed using the EIS method. Typically, the more negative phase at lower frequencies in the Bode phase plot and increased $|Z|$ in the Bode impedance modulus plot indicate the formation of a protective layer on the samples (Fig. 17d).

To better understand and quantify the EIS plots, the data are typically fitted using corresponding equivalent electrical circuits, which ordinarily include the components of resistance, capacitance, and constant phase element (CPE). In the equivalent electrical circuit (Fig. 17d), R_Ω, R_t, and R_L are the solution resistance, combined resistance of migration along the porous layer, and inductor resistance, respectively. CPE is described by its parameter Q and its exponent α, to account for the heterogeneities presented on the surfaces. The corrosion tendency, protective coating efficiency, and electrolyte/electrode interface modification can be evaluated by the variations of these parameters.[310,311]

4.1.3 Electrochemical noise technique. EN signals, corresponding to fluctuations in potential and current during the electrochemical process, can provide valuable information about the corrosion process. EN analysis is an outstanding *in situ* technique for corrosion detection due to its non-destructive and non-intrusive nature.[312,313] In time domains, EN signal analysis begins with removing DC drift, followed by statistical processing to obtain the key parameters including standard deviation, noise resistance, skewness, and kurtosis (Fig. 18a). Higher standard deviation and lower noise resistance suggest a higher corrosion rate. Besides, the Localization Index (LI) is an important statistical parameter that can signify the corrosion type. An LI value near zero indicates general corrosion or passivation, while a value close to 1 demonstrates localized corrosion behavior. For instance, the LI values for Al alloy in DI water were within the range of 0–1, displaying a mixed corrosion behavior (Fig. 18b).[314]

The power spectral density (PSD) of the EN signals can be obtained by fast Fourier transform or maximum entropy method, which provides characteristic information on corrosion behaviors in the frequency domain (Fig. 18c). If the PSD spectrum presents a white noise feature, the electrode is inferred to be dominated by uniform corrosion. It is reported that the average value of the PSD in a certain frequency range of

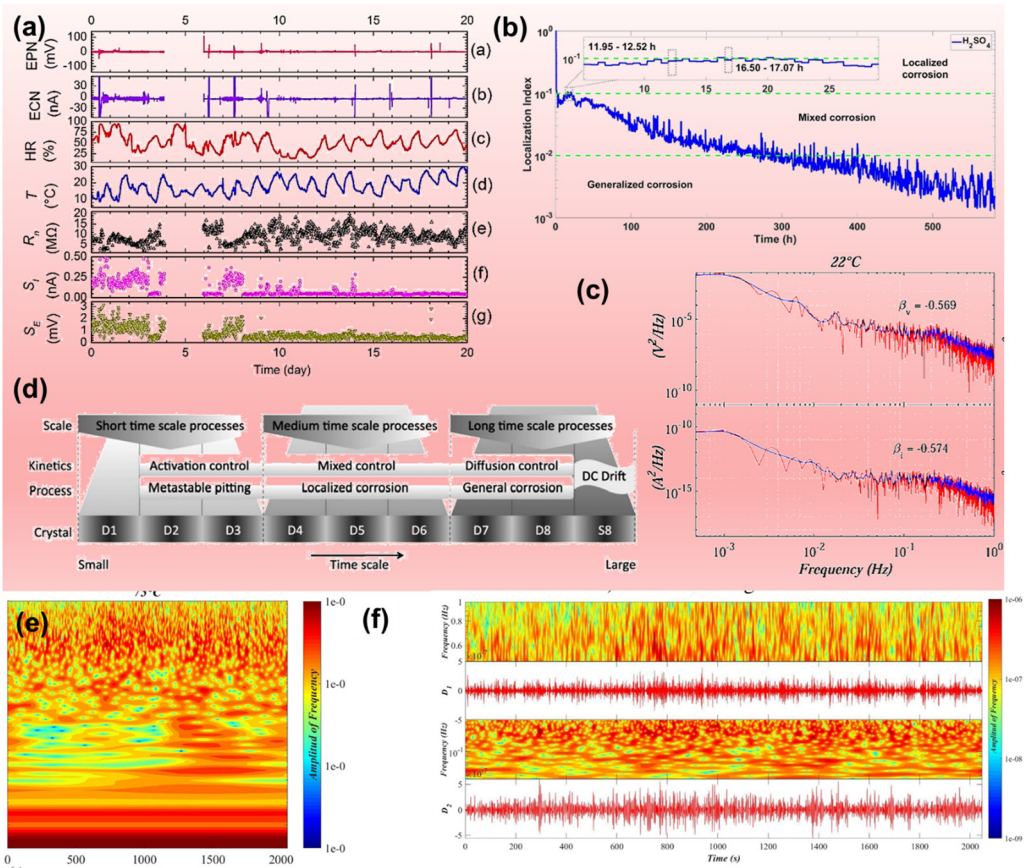

Fig. 18 (a) Typical EN signals of Q235 steel including potential noise, current noise, noise resistance, and standard deviation. Reproduced from ref. 315 with permission from Maney Publishing, copyright 2017. (b) Localization Index of EN signals in different electrolytes. Reproduced from ref. 314 with permission from Elsevier, copyright 2019. (c) PSD curves for the electrochemical potential noise and electrochemical current noise signals obtained from the Al 6061-T6 alloy in a NaCl electrolyte. (d) Schematic of the information that may be obtained from an EDP. Reproduced from ref. 316 with permission from Taylor & Francis, copyright 2019. (e) ST analysis from the electrochemical current noise signals. (f) Comparison between the ST and wavelet transform using the current signal. Reproduced from ref. 317 with permission from Elsevier, copyright 2019.

10–250 MHz corresponds well with the uniform corrosion rate.[318] A roll-off slope of −20 dB per decade or less demonstrates the localized corrosion.[319]

Another method to analyze EN signals is wavelet transform, which can decompose the EN into wavelet coefficients of different scales. Events in the time domain, such as diffusion, activation, or mixed controlled processes, are converted into wavelet crystals with respective crystal energy. The energy distribution plot (EDP), referring to the plot of accumulated energy *vs.* the crystal name, provides detailed information about corrosion mechanisms. The position of the maximum relative energy in the EDP corresponds to the dominant corrosion type. Typically, short-time-scale crystals (D2 and D3 crystals) are associated with activation-controlled pitting corrosion. In contrast, medium-time-scale crystals (D4, D5, and D6) and long-time-scale crystals (D7 and D8) should be related to mixed-controlled localized corrosion and diffusion-controlled general corrosion, respectively (Fig. 18d).[316,319,320]

Furthermore, the Stockwell transform (ST) and Shannon Energy have also been presented as effective proposals to identify the corrosion type at different temperatures (Fig. 18e and f). ST analyses give rise to a series of amplitude scales and establish the relationship between EN signals and the corrosion types. Typically, the amplitude values from potential signals of 1×10^{-6}–1×10^{-5} represent the material passivation, while the values of 1×10^{-5}–1×10^{-4} are considered mixed corrosion. In the range of 1×10^{-4}–1×10^{-3}, the corrosion type is suggested as localized corrosion and uniform corrosion exhibits higher amplitudes. As to ST analyses from current signals, the amplitudes of 1×10^{-9}–1×10^{-8}, 1×10^{-8}–1×10^{-7}, and 1×10^{-7}–1×10^{-6} imply the types of passivation, mixed corrosion, and localized corrosion, respectively.[317] With this promising technique, it is possible to obtain corrosion information at any temperature in terms of corrosion type, corrosion rate, and occurrence time.

4.1.4 Scanning electrochemical microscopy. SECM is a technique that probes the local surface reactivity and chemistry with both high spatial and temporal resolution, by which corrosion behaviors can be expressed in the form of current signals. This kind of visualization for the corrosion behaviors is beneficial for the mechanistic study. It has been widely employed in corrosion studies, including pitting initiation and propagation, surface microstructure, electron transfer kinetics, and corrosion inhibition effectiveness.[157,321–323] First, pitting corrosion initiation on the metal surface can be detected by the conductivity variation that the feedback mode of SECM will visualize.[324] Current density distribution on the Mg surface exposed to 2 M NaCl electrolytes was collected in real time and revealed the passivation film breakdown regions, as illustrated by the higher current densities at the initial stage of corrosion (Fig. 19a). The transition from anodic regions to localized cathodes was also observed by the variation in current (Fig. 19a), which provides evidence for the NDE.[80] Second, local galvanic corrosion or passivation film breakdown can also be monitored due to the enhanced surface reactivity.[325] For example, an SECM measurement of the NiO film breakdown was conducted by using a nanopipette as the probe, which is controlled to contact the Ni/NiO substrate electrode.[326] The E_{break} map indicates that film breakdown susceptibility is spatially grouped and may be categorized into several regions associated with various Ni grains. As an illustration, grains 5 and 6 exhibited reduced E_{break} on average, while grains 3 and 7 showed mostly no breakdown (Fig. 19b). Third, benefitting from the good association between corrosion behavior and detection current, SECM is good at assessing the protection efficiency of the coating layer or corrosion inhibitors.[327,328] The ability of the solid electrolyte interface (SEI) to prevent electron transfer at the electrode surface was investigated using the feedback mode of SECM (FB-SECM).[329] Fig. 19c shows the electrochemical cell's layout as well as a magnified view of the model battery sample with the two separate SEI-covered and SEI-free areas. Regarding the electrical characteristics, the bare Cu and the SEI-covered portions were different, according to the obtained SECM pictures (Fig. 19c). As would be anticipated for a bare metal surface, the normalized tip current is greater than 1 (positive feedback) on the left side of the SECM maps over the SEI-free region. Conversely, over the SEI-covered area on the right, the normalized current is less than 1 (negative feedback).

The tip collection mode of SECM provides opportunities to detect electrochemical hydrogen evolution.[322,330,331] It is reported that a platinum electrode enables the oxidation of hydrogen evolved from the metallic surface and can be used to identify the corrosion sites.[332,333] The hydrogen evolution rate is related to the detection current and gives rise to a visualized corrosion distribution on the surface (Fig. 20a). In addition, the local pH distributions in the corroded region can be monitored in the potentiometric mode with a pH-sensitive antimony microelectrode tip (Fig. 20b and c),[334,335] thereby leading to a better understanding of corrosion mechanisms. Through SECM equipped with a pH-sensitive microelectrode, the pH distribution and variation with time in the vicinity of a corroding surface can be visualized, which is of interest to understanding the corrosion behaviors on a microscale. For example, the pH distribution above an iron sample was presented.[336] The spatial distribution of pH values from the surface into the bulk electrolyte can be observed from the inspection of this image. A relatively homogeneous pH distribution was observed over the Zn sample, suggesting its different corrosion mechanism from that of the iron sample. Moreover, the dissolved oxygen concentration near the metallic surface can be revealed. As shown in Fig. 20d, the oxygen can be intercepted by the SECM tip, which can be reduced at special potentials and give rise to corresponding current signals. In summary, SECM is a powerful tool for detecting the spatial distribution of corrosion reactions in real time, leading to a better understanding of the complicated corrosion mechanisms.

4.2 Spectroscopy characterization

Understanding the crystal and chemical structures of corrosion products on the metallic anode surface is crucial to interpreting the corrosion mechanism and evaluating its influence on the battery performance. Generally, the insoluble corrosion products will lead to the passivation of the metallic anode, which

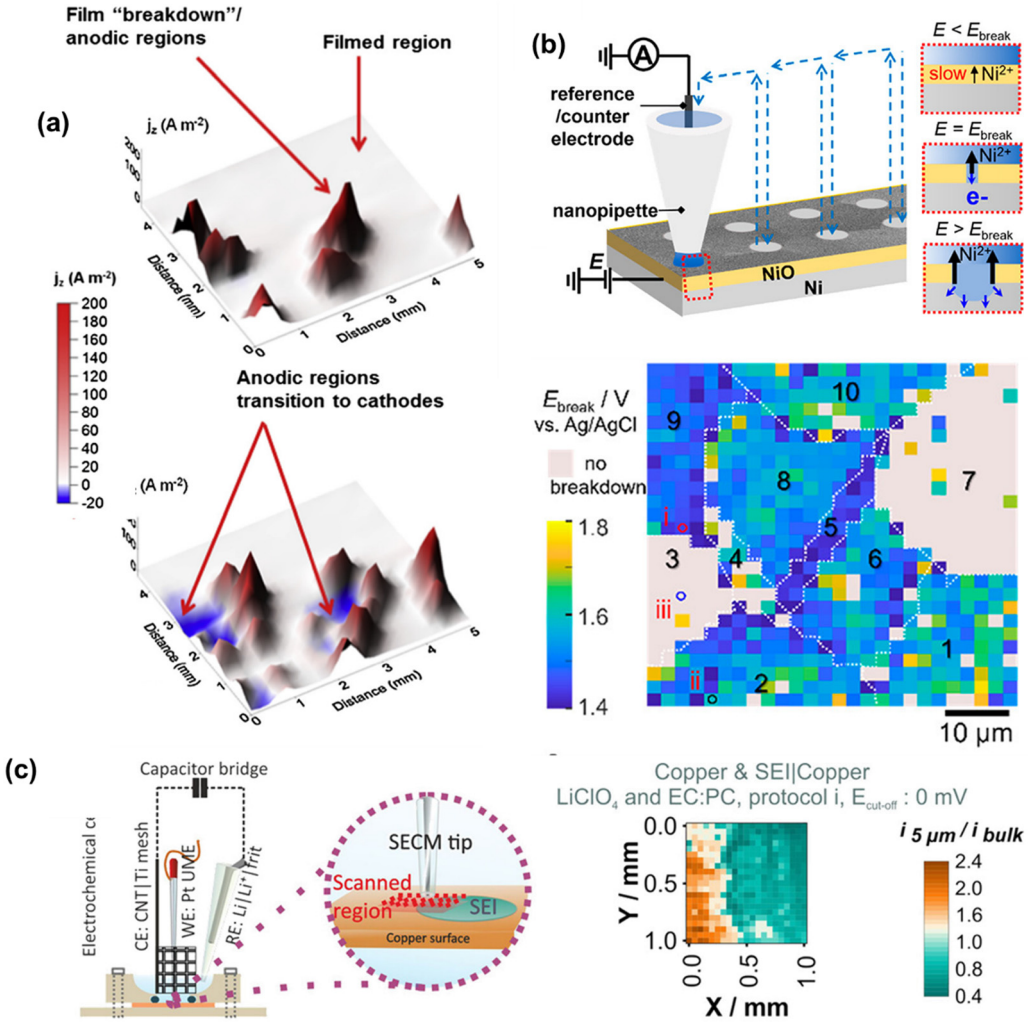

Fig. 19 (a) Current density distributions on Mg surface exposed to 2 M NaCl electrolyte at different time points. Reproduced from ref. 80 with permission from Elsevier, copyright 2015. (b) Schematic showing the mapping of NiO film breakdown on Ni at individual locations *via* SECM and map of breakdown potential (E_{break}) on different grains. Reproduced from ref. 326 with permission from the American Chemical Society, copyright 2022. (c) Schematic of the coaxial electrochemical cell and Non-interpolated SECM image of the scanned area covering the SEI-free (left) and SEI-covered (right) areas. Reproduced from ref. 329 with permission from Wiley, copyright 2022.

will suppress further corrosion and simultaneously hinder the battery kinetics. In this section, applications of advanced spectroscopic techniques in the field of corrosion inhibition, including XRD, Fourier transform infrared (FTIR) spectroscopy, Raman spectroscopy, and XPS, will be discussed.

4.2.1 X-ray diffraction. XRD is frequently applied in phase structure analysis, which provides direct information on the production products. In the first place, the corrosion product on the metal surface can be determined by XRD analysis, through which the possible mechanism and passivation of the metal anode can be evaluated.[339,340] Besides, the successful coating on metallic anode, such as Al_2O_3, TiO_2, and Kaolin layer, can be proved by XRD.[115,121,341–343] Corrosion protection by coating layers can be assessed by the weakened XRD patterns of corrosion products.[115] *In situ* XRD analysis was also reported to investigate the corrosion process of Zn in saline solutions, which demonstrated the gradual appearance of $Zn_5(OH)_8Cl_2 \cdot H_2O$ and $Zn(OH)_2$ after different periods.[344] In brief, XRD helps to distinguish the possible solid species on the metal surface during the corrosion process, which provides a reference for understanding the corrosion process.

4.2.2 Fourier transform infrared spectroscopy. FTIR spectroscopy analysis reveals chemical properties based on the absorption of infrared signals by various covalent bonds at specific wavenumbers. In the field of metal corrosion, FTIR spectroscopy is typically employed to evaluate the surface modification of metallic surfaces. Interaction between metallic anode and organic corrosion inhibitors, such as PEG, PNE, and HEC, can be characterized.[167,209,211,262] The adsorption/desorption of organic corrosion inhibitors during the charge/discharge process is monitored by observing the intensity variations of characteristic bands.[304] Additionally, the organic polymer coating of the metallic anode can be investigated by FTIR spectroscopy analysis.[118,121]

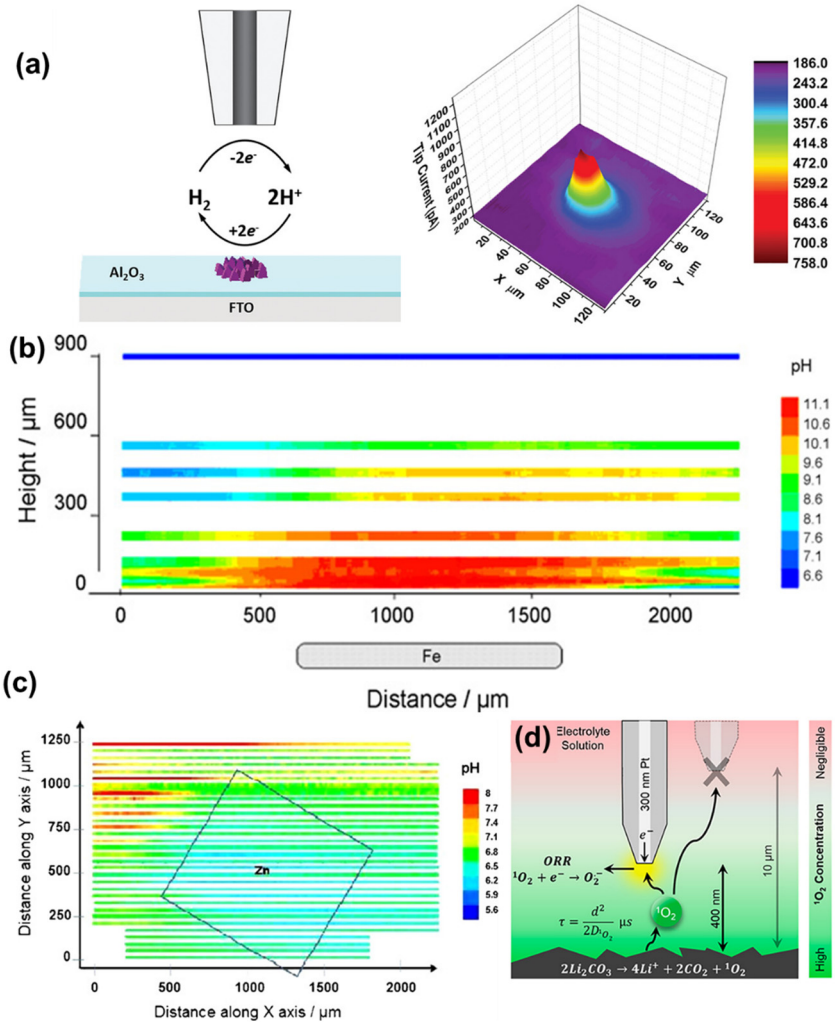

Fig. 20 (a) Schematic of H_2 detection by SECM and the corresponding current distribution caused by H_2 fluxes. Reproduced from ref. 337 with permission from Wiley, copyright 2022. (b) pH distribution in a plane perpendicular to the surface of iron after immersion in 0.1 M NaCl for 22 h. (c) pH distribution in a plane parallel to the surface of Zn after immersion in 0.1 M NaCl for 7 h. Reproduced from ref. 336 with permission from Elsevier, copyright 2011. (d) Illustration of the processes occurring at the electrode-electrolyte interface during SECM measurement; Reproduced from ref. 338 with permission from the American Chemical Society, copyright 2024.

In situ FTIR spectroscopy analysis is a powerful tool to assess the gradual formation of corrosion products. The evolution of Zn surface chemistry in a NaCl solution was detected from the *in situ* FTIR spectra.[344] With the increasing soaking time, the Zn–Cl peak intensity was enhanced, inferring that chloride species were gradually formed on the Zn surface during the corrosion process. In another case, the gradual appearance of Al^{3+}-complexation was demonstrated by increasing the exposure time of the Al electrode in electrolytes containing a humic acid inhibitor, which would serve as a protective film on the Al anode.[259] The characteristic absorption of hydroxy groups in metal hydroxides can also be detected to indicate the corrosion behavior. For instance, shallow $Zn(OH)_2$ was formed on the surface of the MOF-protected Zn anode, demonstrating the inferior corrosion behavior of MOF-based Zn than that of bare Zn (Fig. 21a).[49] From the above description, it can be inferred that FTIR spectroscopy plays a crucial role in the research related to the surface/interface modification engineering of metallic anodes.

4.2.3 X-ray photoelectron spectroscopy. XPS analysis provides information on elements related to valence states and coordination environments on the electrode surface, thereby revealing the elemental composition and surface chemistry. Particularly in alloying engineering, XPS analysis efficiently indicates the valence state evolution of alloying elements and helps to estimate the possible corrosion inhibition mechanisms.[79,171] Matrix metal variation in valance states and coordination environments can also be detected to assess the anodic dissolution process. The appearance of corrosion products and their relative content on the metal surface, such as ZnO, $Zn(OH)_2$, $Al(OH)_3$, $Al(OH)SO_4$, and $Al_2(SO_4)_3{\cdot}18H_2O$, can be distinguished and calculated by high-resolution XPS analysis.[65,167] Besides, XPS analysis is a promising approach to demonstrate the appearance of protective coating layers and to reveal the possible interactions between the

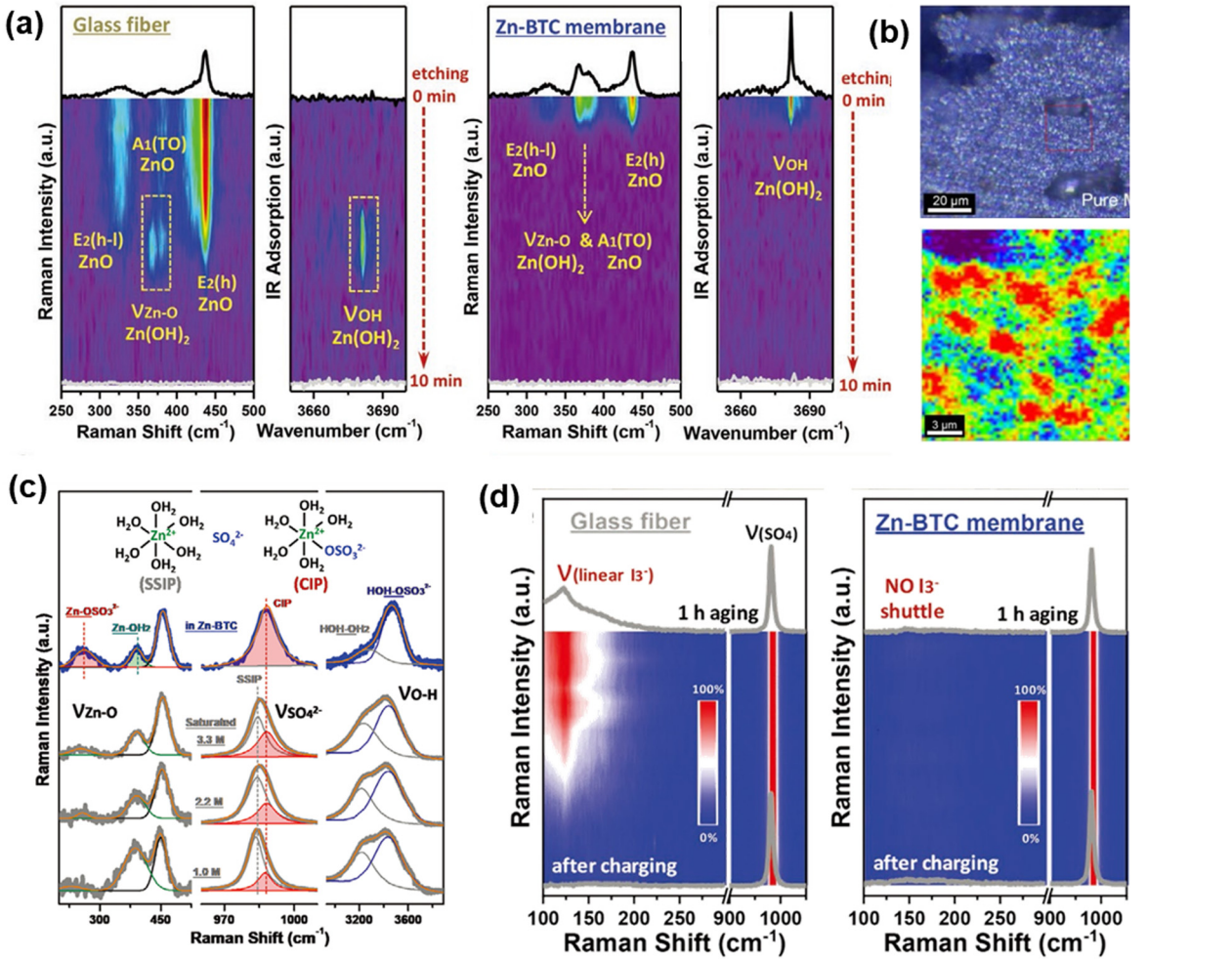

Fig. 21 (a) Raman and FTIR spectra with glass fiber and MOF-based membrane. Reproduced from ref. 49 with permission from John Wiley & Sons, copyright 2020. (b) Raman mapping of the Mg electrode after immersion in 0.1 M NaCl electrolytes. Reproduced from ref. 345 with permission from the Institute of Physics, copyright 2017. (c) Raman spectra $ZnSO_4$ electrolytes (with different concentrations and electrolytes in MOF-based film channels) and (d) Raman spectroscopy of separator harvested from Zn–I_2 batteries after 1 h aging for GF separator and Zn-BTC membrane.

metal surface and coating layers.[115,117] In future studies, we believe that XPS analysis will play a more critical role in clarifying corrosion inhibitors' adsorption/desorption process and the formation process of corrosion products.

4.2.4 Raman spectroscopy. Raman spectroscopy is another powerful tool for studying the chemical composition of corroded electrode surfaces and interactions at the electrode/electrolyte interface or electrode/coating layer interface.[215,222,346–348] On the one hand, the corrosion product formation on the metal surface can be detected by the Raman spectrum. It was reported that Zn electrodes under various degrees of passivation displayed spectral Raman bands corresponding to ZnO. Typically, by *in situ* observing the variation in bands centered at 440 and 550 cm^{-1}, the gradual passivation film formation of the Zn anode in alkaline electrolytes can be illustrated.[349] In another case, E_2(h-l), $A1_{(TO)}$, and E_2(h) modes of ZnO were observed on the Zn surface. Together with ion sputtering equipment, the perpendicular distribution of ZnO in the passivation film was achieved (Fig. 21a). Interestingly, Raman mapping analysis provides more visualized information about the corrosion distribution. $Mg(OH)_2$ distribution across the Mg surface was demonstrated by Raman mapping (Fig. 21b), which can precisely estimate the corrosion tendency of Mg with different surface features.[345]

On the other hand, Raman can probe the electrolyte composition at the electrode/electrolyte interface to evaluate its influence on the corrosion behaviors.[160] Raman spectra of the electrolytes suggested that the hydroxy stretching feature corresponding to free water molecules was suppressed at higher electrolyte concentration levels.[65] With the increase in salt concentration, the free water was transformed into solvating water, leading to corrosion inhibition. Another work also proposed this observation that evaluated the variation in Zn–OH_2, Zn$^-$$OSO_3^{2-}$, SO_4^{2-}, and HOH–OH_2 stretching vibrations by Raman analysis.[49] The results indicated that the electrolyte solvation sheath was enhanced and free water molecule was minimized in the protective film (Fig. 21c). Besides, the corrosive species in the electrode/electrolyte interface can be monitored as well. For instance, with the assistance of Raman analysis, the shuttling of corrosive I_3^- ions

toward the Zn surface was confirmed (Fig. 21d) and the protection of MOF-based film is proposed.[49]

4.3 Morphology characterization

The morphology evolution of metallic anode surfaces, such as passivation film formation and corrosion pits, provides direct evidence for corrosion behaviors. The validity of corrosion inhibition strategies can be visually characterized by morphological information. In this section, four typical techniques, namely atomic force microscopy (AFM), optical microscopy, scanning electron microscopy (SEM), and X-ray computed tomography (CT) will be discussed.

4.3.1 Atomic force microscopy. AFM exhibits a high lateral resolution and is sensitive to morphological change, which endows a precise study of the morphology evolution during the corrosion process. AFM is advantageous in researching the initial stage of corrosion reaction or very localized corrosion behaviors due to its ultrahigh resolution at the nanoscale level. Take pitting corrosion as an example: pit onset locations of stainless steel and metallic Cu have been detected using AFM techniques. Together with other characterizations, the initiation mechanisms of pitting corrosion are achieved.[350,351] During the pitting corrosion, the formation of a pit cap, collapse of the cap, and development in depth of the pit have also been revealed in detail by the *in situ* AFM, giving rise to a comprehensive understanding of the pitting corrosion process.[352] Besides, the galvanic corrosion process at the metal/impurity interface can also be *in situ* characterized by AFM, which exhibits a gradual evolution of topography around impurities. Taking AA2024-T3 aluminum alloy as an example, the Fe-containing (B) and Mg-containing (A) intermetallic particles can be distinguished from the Al matrix due to their different height features, which also present various Volta potentials (Fig. 22a and b).[353] Thus, the galvanic corrosion occurred, leading to a preferential dissolution of Mg. In another case, the Volta potential of the FCC phase was 15 mV higher than that of the BCC phase in the $AlCoCrFeNi_{2.1}$ eutectic high-entropy alloy (EHEA) (Fig. 22c).[354] A micro-galvanic corrosion cell was established between FCC and BCC phases after EHEA was immersed in an acidic electrolyte, resulting in the selective dissolution of BCC phase at the FCC/BCC interface

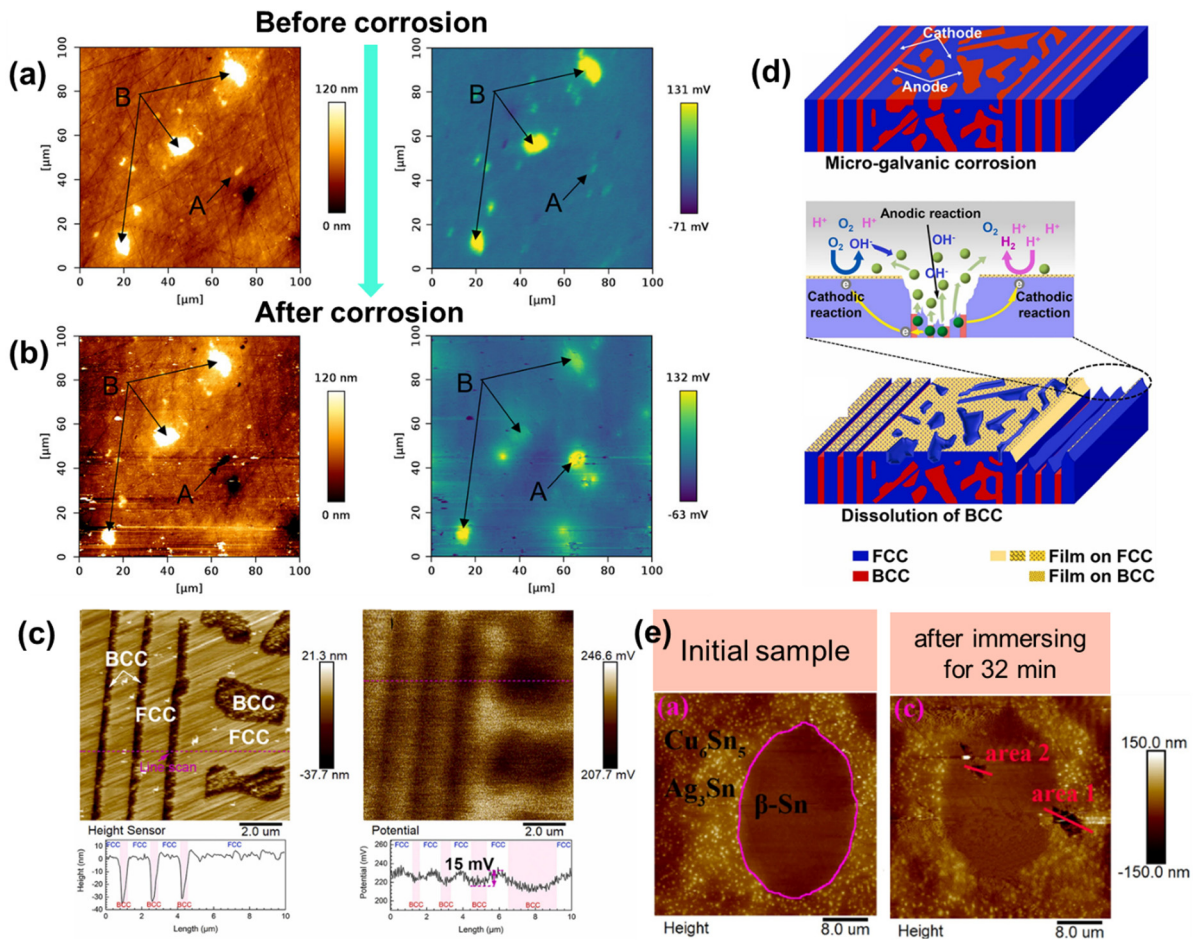

Fig. 22 AFM topography (left) image and Volta potential map (right) of a bare AA2024-T3 sample (a) before and (b) after the corrosion experiment in a 0.1 M $NaClO_4$ electrolyte solution. Reproduced from ref. 353 with permission from Wiley, copyright 2022. (c) Surface topography and Volta potential maps/line profiles of EHEA in 0.5 M H_2SO_4 after 5 min of immersion. (d) Schematic of the corrosion mechanism of EHEA in a sulfuric acid solution. Reproduced from ref. 354 with permission from Elsevier, copyright 2022. (e) Micro-topography of SAC305 alloy after immersion in 0.1 wt% $FeCl_3$; Reproduced from ref. 356 with permission from Elsevier, copyright 2021.

(Fig. 22d). These *in situ* AFM techniques have also underlined relations between local corrosion and structural defects, suggesting that pitting corrosion occurs at grain boundaries or defects.[355] For example, the micro-topography of the SAC305 alloy demonstrated that the local corrosion appears on the eutectic phase (area 1) and β-Sn (area 2) sites (Fig. 22e).[356]

Moreover, *in situ* AFM allows quantitative probing of the local morphology variation in real space and real time at the nanoscale level. Combining *in situ* AFM with other *ex situ* characterizations that allow the identification of the corrosion products, more accurate surface evolution over time can be obtained. AFM can monitor *in situ* variations in height, amplitude, and phase angle on the surface and is typically employed to assess the corrosion product formation.[357] For instance, *in situ* AFM was applied to monitor the initial nucleation and dissolution of Zn in the 5.0 M $ZnCl_2$ electrolyte.[358] The variation in height intuitively demonstrated the plating and striping process of Zn (Fig. 23a and b).

In addition, *in situ* electrochemical AFM (EC-AFM) has been developed to depict the morphological variation under electrochemical control directly.[251] By tuning the applied potential, the corrosion behaviors during the charge/discharge process may be revealed. Using *in situ* EC-AFM, a relationship between the microstructure of Al alloy and localized corrosion was elaborated, giving rise to guidance for the rational design of Al alloys.[361] This type of *in situ* EC-AFM analysis can also clarify the dynamics of the corrosion process. For example, the topography measurement of a 0.5 M NaCl electrolyte-immersed AA2024 alloy with the application of chrono-amperometric pluses was conducted.[359] The roughness, skewness, and kurtosis varied regularly with the pulses (Fig. 23c), illustrating the formation process of an amorphous oxide/oxyhydroxide layer.

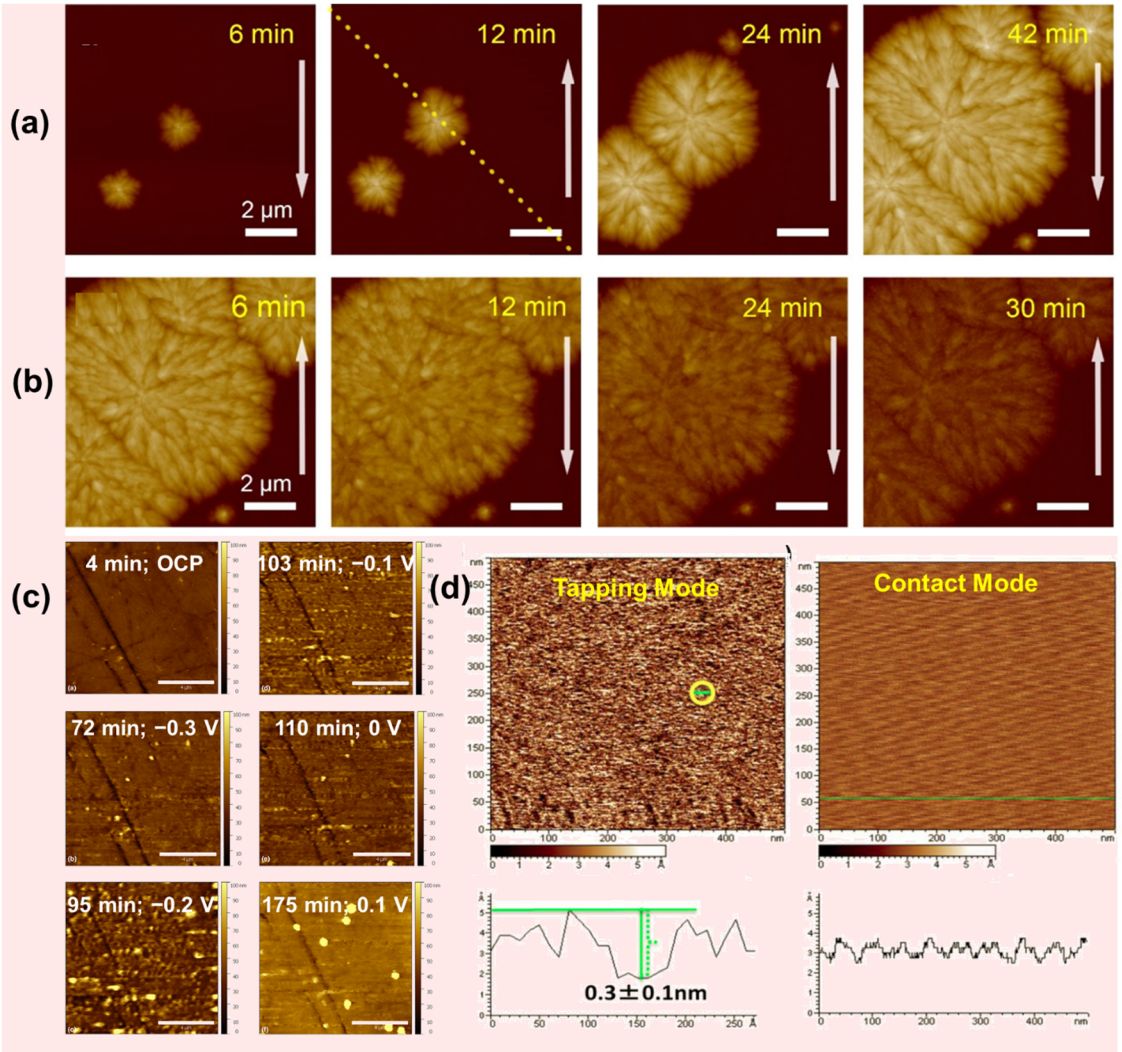

Fig. 23 *In situ* AFM images of (a) nucleation and early growth and (b) dissolution of Zn in the 5.0 M $ZnCl_2$ electrolyte, captured during the galvanostatic charge–discharge process. Reproduced from ref. 358 with permission from the American Chemical Society, copyright 2021. (c) *In situ* EC-AFM topography measurement of immersed AA2024 with the application of chronoamperometric pulses. Reproduced from ref. 359 with permission from Springer Nature, copyright 2021. (d) Comparison between the tapping-mode AFM and contact-mode AFM images of inhibitor films formed on mica. Reproduced from ref. 360 with permission from NACE International, copyright 2021.

Apart from the contact mode, tapping mode is another AFM imaging mode that allows the detection of samples' mechanical properties by phase imaging. By phase image, the difference between the amorphous matrix and α-Al can be distinguished, which provides in-depth observation of the earliest stages of passive film formation in Al metals.[362] Tapping mode AFM has multiple advantages in the imaging of soft surfaces or weak adsorption of corrosion inhibitor molecules. For example, researchers found that tapping mode topography made it easier to distinguish the inhibitor adsorption film that formed on the mica substrate (Fig. 23d).[360] Tapping mode AFM also provides a phase image that can differentiate between areas with different properties regardless of their topographical nature. Sometimes the phase images can provide detailed surface structure, while topography images are quite blurry.

In summary, *in situ* AFM is a powerful technique to monitor the diminutive morphological changes, which provides opportunities for resolving the early stage of the corrosion process.

4.3.2 ***In situ*** **optical microscopy.** Optical microscopy can monitor electrode color and morphology evolutions at a micrometer-scale level. Corrosion product formation, pits appearance, and gas bubble generation can be observed (Fig. 24a and b).[76,93,147,363,364] For instance, the corrosion behavior of Mg electrodes was investigated by real-time microscopy, which found that the surface appearance progressively changes from silvery to dark as a result of the corrosion process. The ratio evolution between the dark regions and the total electrode surface over time was calculated to assess the degree of corrosion. It was also found that the gas bubbles are mainly generated in the dark regions.[93] Although optical microscopy is easy and cost-effective,

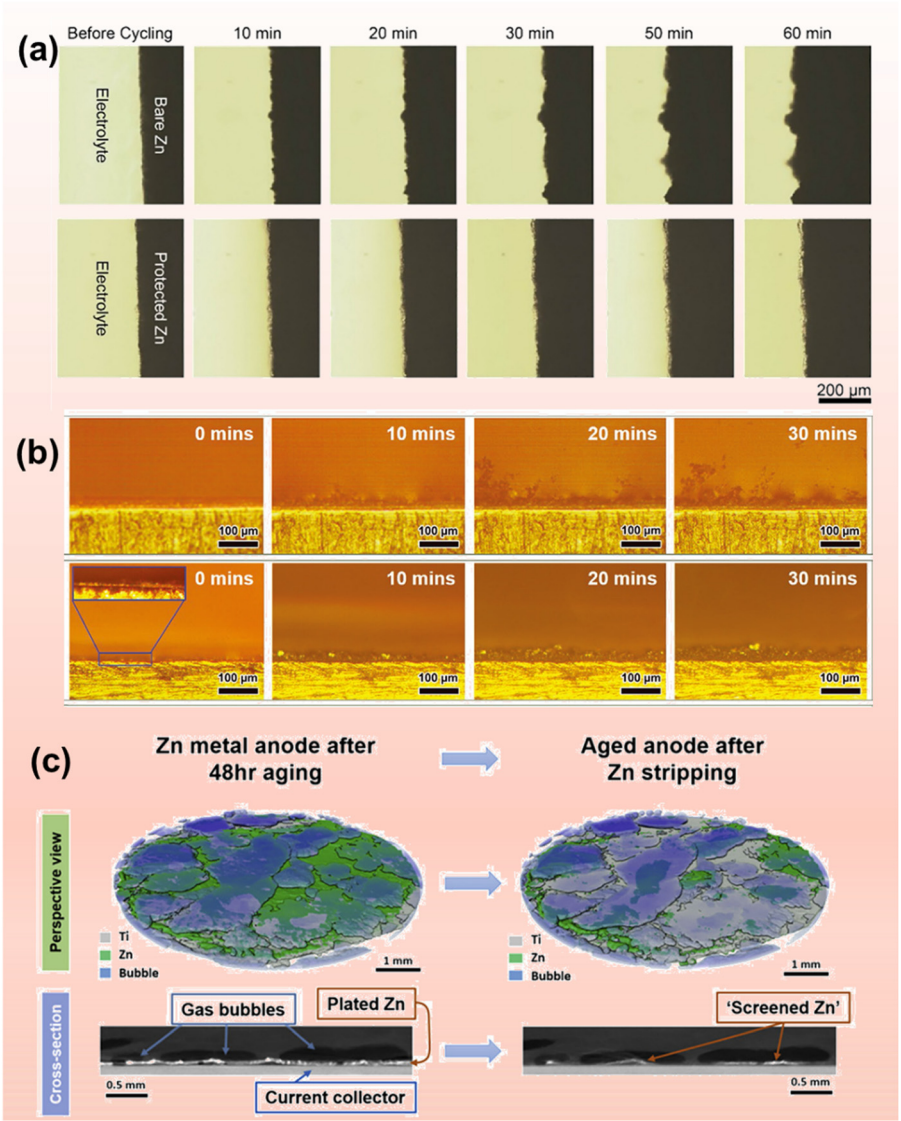

Fig. 24 (a) Operando optical microscopic images of the electrode/electrolyte interface for bare Zn and indium-protected Zn. Reproduced from ref. 120 with permission from Elsevier, copyright 2020. (b) *In situ* optical images of bare Zn and protected Zn surfaces at a current density of 10 mA cm^{-2}. Reproduced from ref. 122 with permission from John Wiley & Sons, copyright 2020. (c) *In situ* CT of Zn anodes undergoing aging. Reproduced from ref. 27 with permission from Cell Press, copyright 2023.

it can only observe the remarkable corrosion tendency and phenomena.

4.3.3 Scanning electron microscopy. Compared with optical microscopy, SEM can provide information about the surface at a smaller scale. SEM analysis is typically employed to compare the morphological changes before and after corrosion.[286,365,366] Corrosion products precipitated on the surface and pits formed on the surface are easily observed by SEM images. Corrosion inhibition efficiencies by various protective strategies can also be assessed by comparing the surface morphologies after corrosion.[167,171] Moreover, the cross-section of electrodes is capable of being characterized by SEM, which helps to evaluate the thickness variation of electrode and passivation layers.[8,120,121,367] Together with energy-dispersive spectroscopy, SEM is good at analyzing the elemental distribution of the corrosion products.[8,80,171]

4.3.4 X-ray computed tomography. Very recently, CT, as a non-destructive tool, has been increasingly used to access the structural evolution of the electrode.[368–370] It is an expert in probing and quantifying valuable 3D morphological parameters, such as porosity and particle distribution. For example, the deposition behavior of Zn has been intuitively observed from the 3D motion diagram generated by *in situ* CT measurement.[370] Different species can be easily identified during *in situ* or operando measurements, and the chemical evolution in the electrodes will be noted. This is because the grey values in CT scans are proportional to the X-ray attenuation of the materials. Take the Zn–Ag battery as an example: the segmentation of Zn particles from ZnO was realized using *in situ* microCT analysis.[369] Besides, as Alex W. Robertson *et al.* reported, electrodeposited Zn and consequently generated H_2 bubbles through corrosion were separated in the CT images.[27] The H_2 bubble-induced screened Zn formation process was also clearly visualized (Fig. 24c). Therefore, CT is a potent supplement to existing morphological characterization methods, which helps to analyze the structural composition and evolution of the electrodes.

5. Summary and prospect

This review article introduced the corrosion behaviors of metallic anodes in aqueous electrolytes. Corrosion mechanisms, possibly generated corrosion products, and influencing factors were discussed in depth. Various strategies to inhibit metallic anode corrosion, including interface engineering, alloying engineering, and electrolyte designing, were summarized. In addition, recent developments in advanced techniques to monitor corrosion processes in the past few years were presented. Research achievements in the field of corrosion inhibition for metallic anodes can be briefly summarized as follows:

(1) The corrosion of metallic anodes results in problems including low utilization of metallic anodes, electrolyte depletion, passivation issues, and H_2 generation. Electrons generated by the metal corrosion are consumed by the cathodic HER rather than run through an external circuit to the cathode of batteries, leading to an irreversible energy loss. The cathodic HER causes the reduction of water and H_2 evolution, which will cause an increase in electrolyte concentration and battery internal pressure. Besides, the corrosion products may cause the passivation of metallic anode. Although they might be protective for further corrosion reactions, the battery kinetics is seriously affected.

(2) Zn anodes are thermodynamically unstable in aqueous electrolytes, and are inclined to be corroded with parasitic HERs or ORRs. In highly acidic electrolytes, Zn^{2+} is the main corrosion product accompanied by the reduction of H^+. In the pH range of 4–11, water reduction and metal hydrolysis greatly influence the local pH values and corrosion product formation. Non-protective ZnO or $Zn(OH)_2$ fractions are formed on the metal surface in this pH range, which is a net result of the passive layer formation caused by OH^- and the destabilization process promoted by H^+. With the continuous increase in pH, three types of $ZnO/Zn(OH)_2$ are generated that can protect Zn from further corrosion but limit the battery kinetics. In highly alkaline electrolytes, zincate is the leading corrosion product. Impurities in Zn anodes, dissolved oxygen, and anions in the electrolytes, such as Cl^-, ClO_4^-, SO_4^{2-}, and CO_3^{2-}, can participate in the corrosion reactions and make differences in the corrosion behaviors.

(3) Al anode corrosion in acidic electrolytes is similar to that of Zn. In mildly acidic or alkaline electrolytes, the compact Al_2O_3 layer can protect Al from corrosion and suppress the reversible plating/stripping of Al at the same time. In highly alkaline electrolytes, Al corrosion proceeds with the continuous formation of $Al(OH)_3$ in the metal/passivation layer interface and the dissolution of $Al(OH)_3$ in the passivation/electrolyte interface. The passivation layer on the surface plays an important role in the corrosion process. Similarly, impurities in Al anodes, dissolved oxygen, and aggressive anions can accelerate the corrosion reaction of Al, which should be mainly considered.

(4) Corrosion mechanisms of Mg are controversial and the most convincing one demonstrates that Mg corrosion is initiated with the local breakdown of the MgO film and the NDE is ascribed to the formation of $Mg(OH)_2$ product. In neutral and alkaline electrolytes, $Mg(OH)_2$ is the only corrosion product, which would serve as cathodic sites to accelerate the HER. However, when the pH value exceeds 10.5, $Mg(OH)_2$ formed on the surface will passivate Mg from dissolution. It is worth noting that dissolved oxygen in electrolytes does not influence Mg corrosion much due to the high HER rates. Most of the metallic impurities are more noble than Mg and will accelerate Mg dissolution.

(5) Artificial interfaces including carbonaceous layers, metallic compounds, and organic polymers can protect metallic anodes from direct exposure to aqueous electrolytes, thereby reducing corrosion reactions. Apart from acting as physical barriers, some interfaces such as indium-based compounds also serve as chemical corrosion inhibitors, which can increase the HER overpotential. The abundant surface chemistry of carbon layers or organic polymers is also important in preventing aggressive anions from getting close to the metal surface. Though effective in corrosion inhibition, the coating layer will cause sluggish ion transport between the metal anode and

electrolytes, resulting in inferior battery kinetics and large polarization. The corrosion inhibition efficiency and battery performance are heavily dependent on the microstructural characteristics of the coating layer, which undoubtedly increases the difficulty and cost of preparation. Most of the sophisticated synthetic techniques published in the literature are not suited for large-scale preparation, which restricts their practical applicability.

(6) Alloying engineering is another effective strategy to improve the corrosion resistance of metallic anodes. On the one hand, alloying elements or as-formed intermetallic phases with higher HER overpotentials are beneficial to reducing the cathodic HER. On the other hand, some alloying elements help to form protective corrosion layers (such as $La(OH)_3$ and Al_2O_3) during the corrosion process. However, the formed secondary phase will accelerate the corrosion reaction if it presents a more noble electrochemical activity than the protected metal. Almost all Mg intermetallic phases can enhance the dissolution of Mg due to the formation of galvanic cells. Although the alloy anode is easy to prepare on a large scale, alloying engineering requires strict control of the alloy ratio and phase distribution to ensure the anode's electrochemical performance. There are still issues with alloy element compatibility and precise phase composition management during large-scale preparation.

(7) Electrolyte engineering significantly impacts the electrochemistry at the metallic anode/electrolyte interface. Metal corrosion behavior in aqueous electrolytes highly depends on the pH value, which should be considered when designing electrolytes. Reducing the contents of free water molecules through high-concentration electrolytes or gel electrolytes greatly diminishes the interaction between metal and water, thus protecting metallic anodes from corrosion. The corrosion inhibitor strategy offers special benefits such as easy large-scale preparation, cheapness, and simple operation. All that is required for this method is the addition of a very small quantity of an appropriate corrosion inhibitor to the electrolyte. Corrosion inhibitors suppress metal corrosion in various ways, including protective layer formation, surface chemistry modification, and adjustment of electrolyte pH. Although the addition of corrosion inhibitors may deteriorate the battery kinetics, it is the most facile and cost-effective strategy to suppress metal corrosion.

(8) The change of electrochemical signals or surface morphology can monitor corrosion behaviors. The polarization curve method, EIS, and EN technique are frequently employed to understand corrosion mechanisms and get information on corrosion tendency and rate. Some advanced techniques such as *in situ* SECM, *in situ* AFM, and operando optical microscopy allow for observing the spatial distribution of corrosion reaction in real time by monitoring surface currents and morphology evolutions. Besides, conventional characterization methods such as Raman, SEM, and FTIR can help distinguish corrosion products.

Besides these achievements discussed in this review, many challenges remain (Fig. 25). The challenges that should be addressed and potential further research directions are summarized as follows:

1. Fundamental corrosion mechanisms of metallic anodes in aqueous electrolytes should be further elucidated. Behaviors at the initial stage of the corrosion reaction are still unclear, and the formation of corrosion products essentially speculates on the existing mechanism. Besides, the corrosion behavior monitoring during the charge/discharge process of the battery deserves more effort, which should consider the reversible stripping/plating of the metal anode. Moreover, the corrosion mechanism of Mg is still controversial and advanced *in situ* techniques should be employed to classify the Mg corrosion behaviors.

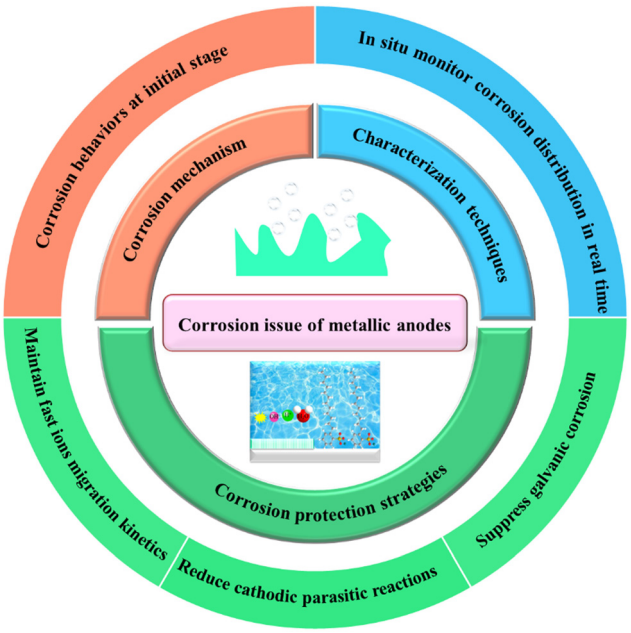

Fig. 25 Challenges and potential research directions toward the corrosion issue of metallic anodes.

2. Artificial interface engineering to protect metallic anodes from corrosion suffers from the main penalty of deteriorating battery kinetics. Although water molecules and aggressive anions can be kept out of the anode surface efficiently, sluggish metal ion migration across the coating layer results in large polarization and inferior rate capability. Besides, the structural integrity of the protective interfaces in large-scale production is still challenging, which may lead to serious pitting corrosion. The *in situ* formation of protective film or artificial solid electrolyte interface during the charge/discharge process may be a promising direction, which reduces the assembly cost and maintains the durability of the protective layer. High chemical/electrochemical stability, high integrity without fractures, high-speed electrolyte ion conductivity, a strong capacity to bond with the metal anode, and lightweight characteristics are all necessary for the perfect interface protection layer.

3. In alloying engineering, there is no standard criterion for choosing alloying elements and their corresponding amounts. A comprehensive examination of relationships between alloying elements and their protection efficiency is urgently needed to tackle this challenge. Meanwhile, the influences of alloying elements on the grain size, intermetallic phase distribution, and exposed crystalline facet should be considered in further research.

4. As to electrolyte engineering, developing new electrolyte systems with mild acidity/alkalinity and less aggressive anions is a potential direction to gain excellent corrosion inhibition. Despite various additives' great corrosion inhibition efficiency, the surface chemistry variation caused by organic additives lacks in-depth understanding. Further research on organic additives' adsorption/desorption kinetics and corresponding surface properties evolutions is urgently needed. A rational combination of different additives may be a potential research direction to improve the corrosion inhibition efficiency. Besides, hydrogel electrolytes with less free water molecules have tremendous application potential in suppressing metallic anode corrosion. Moreover, organic/aqueous hybrid electrolyte design is another attractive research direction in this field, as the reduced protons in the hybrid electrolytes may hinder the corrosion of metallic anodes.

5. Apart from the electrolyte pH values, local pH values play a crucial role in affecting the corrosion behaviors, which are seldom examined. Advanced microelectrochemical techniques such as scanning vibrating electrode techniques deserve more investigations, which can give rise to new mechanistic insights into the highly localized corrosion processes. Employing more *in situ* techniques such as AFM, SECM, and EN to study the metallic anode's corrosion should be a potential research trend.

Data availability

No primary research results, software or code have been included and no new data were generated or analyzed as part of this review. All the figures and tables were reproduced from references with permissions.

Conflicts of interest

There are no conflicts to declare.

Acknowledgements

This work was supported by the National Natural Science Foundation of China (22109178, 52277229, 52202337, 22371153), Natural Science Foundation of Shandong Province (ZR2023MB051, ZR2021QB085), National Key Research and Development of China (2022YFA1503402), the Fundamental Research Funds for the Central Universities (2462023QNXZ015, 24CX07003A), and the Young Taishan Scholars Program of Shandong Province (tsqn202211082, tsqn202312224).

References

1 X. Cai, X. Wang, Z. Bie, Z. Jiao, Y. Li, W. Yan, H. J. Fan and W. Song, *Adv. Mater.*, 2024, **36**, 2306734.
2 Z. Chen, Y. Wang, Q. Wu, C. Wang, Q. He, T. Hu, X. Han, J. Chen, Y. Zhang, J. Chen, L. Yang, X. Wang, Y. Ma and J. Zhao, *Adv. Mater.*, 2024, **36**, 2411004.
3 Q. Yang, Q. Li, Z. Liu, D. Wang, Y. Guo, X. Li, Y. Tang, H. Li, B. Dong and C. Zhi, *Adv. Mater.*, 2020, **32**, 2001854.
4 W. Zhou, S. Ding, D. Zhao and D. Chao, *Joule*, 2023, **7**, 1104–1107.
5 Y. Zhao, D. Wang, X. Li, Q. Yang, Y. Guo, F. Mo, Q. Li, C. Peng, H. Li and C. Zhi, *Adv. Mater.*, 2020, **32**, 2003070.
6 B. Ge, L. Hu, X. Yu, L. Wang, C. Fernandez, N. Yang, Q. Liang and Q.-H. Yang, *Adv. Mater.*, 2024, **36**, 2400937.
7 Z. Zhao, X. Fan, J. Ding, W. Hu, C. Zhong and J. Lu, *ACS Energy Lett.*, 2019, **4**, 2259–2270.
8 Z. Cai, Y. Ou, J. Wang, R. Xiao, L. Fu, Z. Yuan, R. Zhan and Y. Sun, *Energy Storage Mater.*, 2020, **27**, 205–211.
9 Y. Liu, Q. Sun, W. Li, K. R. Adair, J. Li and X. Sun, *Green Energy Environ.*, 2017, **2**, 246–277.
10 A. R. Mainar, O. Leonet, M. Bengoechea, I. Boyano, I. de Meatza, A. Kvasha, A. Guerfi and J. Alberto Blazquez, *Int. J. Energy Res.*, 2016, **40**, 1032–1049.
11 G. Chen, Y. Kang, H. Yang, M. Zhang, J. Yang, Z. Lv, Q. Wu, P. Lin, Y. Yang and J. Zhao, *Adv. Funct. Mater.*, 2023, **33**, 2300656.
12 Y.-H. Lee, Y. Jeoun, J. H. Kim, J. Shim, K.-S. Ahn, S.-H. Yu and Y.-E. Sung, *Adv. Funct. Mater.*, 2024, **34**, 2310884.
13 A. Kolesnikov, M. Kolek, J. F. Dohmann, F. Horsthemke, M. Börner, P. Bieker, M. Winter and M. C. Stan, *Adv. Energy Mater.*, 2020, **10**, 2000017.
14 W. Xiong, D. Yang, T. K. A. Hoang, M. Ahmed, J. Zhi, X. Qiu and P. Chen, *Energy Storage Mater.*, 2018, **15**, 131–138.
15 C. Y. Chen, K. Matsumoto, K. Kubota, R. Hagiwara and Q. Xu, *Adv. Energy Mater.*, 2019, **9**, 1900196.
16 C. Cai, R. Song, L. Wang and J. Li, *Appl. Surf. Sci.*, 2018, **462**, 243–254.
17 K. Yasakau, *Corros. Mater. Degrad.*, 2020, **1**, 345–372.
18 W. Yuan, X. Nie, G. Ma, M. Liu, Y. Wang, S. Shen and N. Zhang, *Angew. Chem., Int. Ed.*, 2023, **62**, e202218386.
19 Y. Li, X. Fan, X. Liu, S. Qu, J. Liu, J. Ding, X. Han, Y. Deng, W. Hu and C. Zhong, *J. Mater. Chem. A*, 2019, **7**, 25449–25457.
20 P. Katsoufis, V. Mylona, C. Politis, G. Avgouropoulos and P. Lianos, *J. Power Sources*, 2020, **450**, 227624.
21 C. Lv, Y. Zhang, J. Ma, Y. Zhu, D. Huang, Y. Li, H. Wang and Y. Tang, *J. Mater. Chem. A*, 2022, **10**, 9506–9514.
22 C. Lv, Y. Zhu, Y. Li, Y. Zhang, J. Kuang, Y. Tang, H. Li and H. Wang, *Energy Storage Mater.*, 2023, **59**, 102756.
23 W. Du, E. H. Ang, Y. Yang, Y. Zhang, M. Ye and C. C. Li, *Energy Environ. Sci.*, 2020, **13**, 3330–3360.
24 J. Sun, F. Kang, D. Yan, T. Ding, Y. Wang, X. Zhou and Q. Zhang, *Angew. Chem., Int. Ed.*, 2024, **63**, e202406511.
25 G. Wang, Q.-K. Zhang, X.-Q. Zhang, J. Lu, C. Pei, D. Min, J.-Q. Huang and H. S. Park, *Adv. Energy Mater.*, 2025, **15**, 2304557.
26 Z. Cai, J. Wang and Y. Sun, *eScience*, 2023, **3**, 100093.
27 S. D. Pu, B. Hu, Z. Li, Y. Yuan, C. Gong, Z. Ning, C. Chau, S. Yang, S. Zhang, L. Pi, Y. T. Tang, J. Yue, T. J. Marrow, X. Gao, P. G. Bruce and A. W. Robertson, *Joule*, 2023, **7**, 366–379.
28 C. Liu, Z. Luo, W. Deng, W. Wei, L. Chen, A. Pan, J. Ma, C. Wang, L. Zhu, L. Xie, X.-Y. Cao, J. Hu, G. Zou, H. Hou and X. Ji, *ACS Energy Lett.*, 2021, **6**, 675–683.

29 Y. Wang, H. Y. H. Kwok, W. Pan, H. Zhang, X. Lu and D. Y. C. Leung, *Appl. Energy*, 2019, **251**, 113342.
30 A. P. Sinha, T. S. Thomas and D. Mandal, *Energy Storage Mater.*, 2023, **63**, 102988.
31 J. Gao, X. Li, Q. Liu, H. Fan, S. Gao, Y. Song and E. Wang, *Chem. Eng. J*, 2023, **464**, 142655.
32 J. Wang, L. Cui, S. Li, T. Pu, X. Fang, S. Kang and X. Zhang, *New J. Chem.*, 2020, **44**, 1624–1631.
33 H. Li, L. Ma, C. Han, Z. Wang, Z. Liu, Z. Tang and C. Zhi, *Nano Energy*, 2019, **62**, 550–587.
34 X. Li, Y. Tang, J. Zhu, H. Lv, L. Zhao, W. Wang, C. Zhi and H. Li, *Small*, 2020, **16**, 2001935.
35 Z. Liu, Y. Huang, Y. Huang, Q. Yang, X. Li, Z. Huang and C. Zhi, *Chem. Soc. Rev.*, 2020, **49**, 180–232.
36 Y. Tang, X. Li, H. Lv, D. Xie, W. Wang, C. Zhi and H. Li, *Adv. Energy Mater.*, 2020, **10**, 2000892.
37 X. Li, Y. Tang, H. Lv, W. Wang, F. Mo, G. Liang, C. Zhi and H. Li, *Nanoscale*, 2019, **11**, 17992–18008.
38 C. Han, W. Li, H. K. Liu, S. Dou and J. Wang, *Nano Energy*, 2020, **74**, 104880.
39 K. Wippermann, J. W. Schultze, R. Kessel and J. Penninger, *Corros. Sci.*, 1991, **32**, 205–230.
40 K. G. Boto and L. F. G. Williams, *J. Electroanal. Chem. Interfacial Electrochem.*, 1977, **77**, 1–20.
41 S. Thomas, N. Birbilis, M. S. Venkatraman and I. S. Cole, *Corrosion*, 2012, **68**, 9.
42 Z. Zembura and L. Burzynska, *Corros. Sci.*, 1977, **17**, 871–878.
43 M. Gmytryk and J. Sedzimir, *Corros. Sci.*, 1967, **7**, 683–695.
44 M. Mouanga, P. Berçot and J. Y. Rauch, *Corros. Sci.*, 2010, **52**, 3984–3992.
45 C. Qiao, L. Shen, L. Hao, X. Mu, J. Dong, W. Ke, J. Liu and B. Liu, *J. Mater. Sci. Technol.*, 2019, **35**, 2345–2356.
46 L. M. Baugh, *Electrochim. Acta*, 1979, **24**, 669–677.
47 M. Mokaddem, P. Volovitch and K. Ogle, *Electrochim. Acta*, 2010, **55**, 7867–7875.
48 L. M. Baugh and A. Higginson, *Electrochim. Acta*, 1985, **30**, 1163–1172.
49 H. Yang, Y. Qiao, Z. Chang, H. Deng, P. He and H. Zhou, *Adv. Mater.*, 2020, **32**, 2004240.
50 J.-H. Lee, Y. Byun, G. H. Jeong, C. Choi, J. Kwen, R. Kim, I. H. Kim, S. O. Kim and H.-T. Kim, *Adv. Mater.*, 2019, **31**, 1904524.
51 B. Evanko, S. J. Yoo, J. Lipton, S.-E. Chun, M. Moskovits, X. Ji, S. W. Boettcher and G. D. Stucky, *Energy Environ. Sci.*, 2018, **11**, 2865–2875.
52 L. Gao, Z. Li, Y. Zou, S. Yin, P. Peng, Y. Shao and X. Liang, *iScience*, 2020, **23**, 101348.
53 S. M. A. E. Haleem, *Br. Corros. J.*, 1976, **11**, 215–218.
54 X. G. Zhang, *Corrosion and Electrochemistry of Zinc*, Springer Science & Business Media, New York, 2013.
55 A. D. Keitelman, S. M. Gravano and J. R. Galvele, *Corros. Sci.*, 1984, **24**, 535–545.
56 S. Wu, Q. Zhang, D. Sun, J. Luan, H. Shi, S. Hu, Y. Tang and H. Wang, *Chem. Eng. J*, 2020, **383**, 123162.
57 C. Wu, S. Gu, Q. Zhang, Y. Bai, M. Li, Y. Yuan, H. Wang, X. Liu, Y. Yuan, N. Zhu, F. Wu, H. Li, L. Gu and J. Lu, *Nat. Commun.*, 2019, **10**, 73.
58 Y. Wang, T. Wu, Y. Lu, W. Zhang and Z. Li, *Angew. Chem., Int. Ed.*, 2024, e202416032n/a.
59 X. Yang, H. Gu, L. Chai, S. Chen, W. Zhang, H. Y. Yang and Z. Li, *Nano Lett.*, 2024, **24**, 8542–8549.
60 S.-M. Moon and S.-I. Pyun, *Electrochim. Acta*, 1999, **44**, 2445–2454.
61 I. Boukerche, S. Djerad, L. Benmansour, L. Tifouti and K. Saleh, *Corros. Sci.*, 2014, **78**, 343–352.
62 R. Ambat and E. S. Dwarakadasa, *J. Appl. Electrochem.*, 1994, **24**, 911–916.
63 J. Flis and L. Kowalczyk, *J. Appl. Electrochem.*, 1995, **25**, 501–507.
64 W.-J. Lee and S.-I. Pyun, *Electrochim. Acta*, 2000, **45**, 1901–1910.
65 S. Li and B. C. Church, *Appl. Surf. Sci.*, 2018, **440**, 861–872.
66 D. N. D. Singh, *J. Electrochem. Soc.*, 1982, **129**, 1869–1874.
67 G. O. H. Whillock and S. E. Worthington, in *Shreir's Corrosion*, ed. B. Cottis, M. Graham, R. Lindsay, S. Lyon, T. Richardson, D. Scantlebury and H. Stott, Elsevier, Oxford, 2010, vol. 2, pp. 1250–1269.
68 R. G. Wymer and R. E. Blanco, *Ind. Eng. Chem.*, 1957, **49**, 59–61.
69 G. T. Burstein and R. M. Organ, *Corros. Sci.*, 2005, **47**, 2932–2955.
70 K. F. Khaled, *Corros. Sci.*, 2010, **52**, 2905–2916.
71 B. C. Bunker, G. C. Nelson, K. R. Zavadil, J. C. Barbour and J. P. Sullivan, *J. Phys. Chem. B*, 2002, **106**, 4705–4713.
72 R. S. Alwitt, *J. Electrochem. Soc.*, 1974, **121**, 1322.
73 S. S. Razavi-Tousi and J. A. Szpunar, *Electrochim. Acta*, 2014, **127**, 95–105.
74 S.-I. Pyun and S.-M. Moon, *J. Solid State Electrochem.*, 2000, **4**, 267–272.
75 M. Jingling, W. Jiuba, Z. Hongxi and L. Quanan, *J. Power Sources*, 2015, **293**, 592–598.
76 Y. Liu, Q. Pan, H. Li, Z. Huang, J. Ye and M. Li, *J. Alloys Compd.*, 2019, **792**, 32–45.
77 P. W. Beetz, *Philos. Mag.*, 1866, **32**, 269–278.
78 M. Curioni, F. Scenini, T. Monetta and F. Bellucci, *Electrochim. Acta*, 2015, **166**, 372–384.
79 P. Gore, S. Fajardo, N. Birbilis, G. S. Frankel and V. S. Raja, *Electrochim. Acta*, 2019, **293**, 199–210.
80 S. Thomas, N. V. Medhekar, G. S. Frankel and N. Birbilis, *Curr. Opin. Solid State Mater. Sci.*, 2015, **19**, 85–94.
81 G. G. Perrault, *J. Electroanal. Chem. Interfacial Electrochem.*, 1970, **27**, 47–58.
82 E. Gulbrandsen, J. Taftø and A. Olsen, *Corros. Sci.*, 1993, **34**, 1423–1440.
83 G. L. Song and A. Atrens, *Adv. Eng. Mater.*, 1999, **1**, 11–33.
84 R. L. Petty, A. W. Davidson and J. Kleinberg, *J. Am. Chem. Soc.*, 1954, **76**, 363–366.
85 P. F. King, *J. Electrochem. Soc.*, 1966, **113**, 536.
86 M. E. Straumanis and Y. N. Wang, *J. Electrochem. Soc.*, 1955, **102**, 304.
87 G. R. Hoey and M. Cohen, *J. Electrochem. Soc.*, 1958, **105**, 245.
88 M. Taheri, J. R. Kish, N. Birbilis, M. Danaie, E. A. McNally and J. R. McDermid, *Electrochim. Acta*, 2014, **116**, 396–403.

89 M. Danaie, R. M. Asmussen, P. Jakupi, D. W. Shoesmith and G. A. Botton, *Corros. Sci.*, 2013, **77**, 151–163.
90 N. T. Kirkland, G. Williams and N. Birbilis, *Corros. Sci.*, 2012, **65**, 5–9.
91 G. S. Frankel, A. Samaniego and N. Birbilis, *Corros. Sci.*, 2013, **70**, 104–111.
92 L. Rossrucker, K. J. J. Mayrhofer, G. S. Frankel and N. Birbilis, *J. Electrochem. Soc.*, 2014, **161**, C115–C119.
93 M. Curioni, *Electrochim. Acta*, 2014, **120**, 284–292.
94 N. Birbilis, A. D. King, S. Thomas, G. S. Frankel and J. R. Scully, *Electrochim. Acta*, 2014, **132**, 277–283.
95 K. A. Unocic, H. H. Elsentriecy, M. P. Brady, H. M. Meyer, G. L. Song, M. Fayek, R. A. Meisner and B. Davis, *J. Electrochem. Soc.*, 2014, **161**, C302–C311.
96 J. Liang, P. B. Srinivasan, C. Blawert and W. Dietzel, *Corros. Sci.*, 2010, **52**, 540–547.
97 H. Wu, Z. Shi, X. Zhang, A. M. Qasim, S. Xiao, F. Zhang, Z. Wu, G. Wu, K. Ding and P. K. Chu, *Appl. Surf. Sci.*, 2019, **478**, 150–161.
98 M. Deng, D. Höche, S. V. Lamaka, L. Wang and M. L. Zheludkevich, *Corros. Sci.*, 2019, **153**, 225–235.
99 N. Wang, R. Wang, Y. Feng, W. Xiong, J. Zhang and M. Deng, *Corros. Sci.*, 2016, **112**, 13–24.
100 D. Lei, D. C. Lee, A. Magasinski, E. Zhao, D. Steingart and G. Yushin, *ACS Appl. Mater. Inter.*, 2016, **8**, 2088–2096.
101 H. Weinrich, J. Come, H. Tempel, H. Kungl, R.-A. Eichel and N. Balke, *Nano Energy*, 2017, **41**, 706–716.
102 C. Bai, H. Jin, Z. Gong, X. Liu and Z. Yuan, *Energy Storage Mater.*, 2020, **28**, 247–254.
103 X. Wu, A. Markir, Y. Xu, C. Zhang, D. P. Leonard, W. Shin and X. Ji, *Adv. Funct. Mater.*, 2019, **29**, 1900911.
104 X. Wu, A. Markir, Y. Xu, E. C. Hu, K. T. Dai, C. Zhang, W. Shin, D. P. Leonard, K. I. Kim and X. Ji, *Adv. Energy Mater.*, 2019, **9**, 1902422.
105 D. Enning and J. Garrelfs, *Appl. Environ. Microbiol.*, 2014, **80**, 1226.
106 E. E. Oguzie, B. N. Okolue, E. E. Ebenso, G. N. Onuoha and A. I. Onuchukwu, *Mater. Chem. Phys.*, 2004, **87**, 394–401.
107 R. C. Zeng, Y. Hu, S. K. Guan, H. Z. Cui and E. H. Han, *Corros. Sci.*, 2014, **86**, 171–182.
108 J. K. Lin, C. L. Hsia and J. Y. Uan, *Scr. Mater.*, 2007, **56**, 927–930.
109 J. Xu, J. Hu and S. Hu, *Chem. Res. Chin. Univ.*, 2019, **35**, 641–646.
110 P. Pei, K. Wang and Z. Ma, *Appl. Energy*, 2014, **128**, 315–324.
111 X. Yin, *Int. J. Electrochem. Sci.*, 2017, **12**, 4150–4163.
112 R. L. Liu, Z. R. Zeng, J. R. Scully, G. Williams and N. Birbilis, *Corros. Sci.*, 2018, **140**, 18–29.
113 H. Jia, Z. Wang, B. Tawiah, Y. Wang, C.-Y. Chan, B. Fei and F. Pan, *Nano Energy*, 2020, **70**, 104523.
114 M. Zhu, Q. Ran, H. Huang, Y. Xie, M. Zhong, G. Lu, F.-Q. Bai, X.-Y. Lang, X. Jia and D. Chao, *Nano-Micro Lett.*, 2022, **14**, 219.
115 K. Zhao, C. Wang, Y. Yu, M. Yan, Q. Wei, P. He, Y. Dong, Z. Zhang, X. Wang and L. Mai, *Adv. Mater. Interfaces*, 2018, **5**, 1800848.
116 K. Wongrujipairoj, L. Poolnapol, A. Arpornwichanop, S. Suren and S. Kheawhom, *Phys. Status Solidi B*, 2017, **254**, 1600442.
117 H. Wei, X. Hu, X. Zhang, Z. Yu, T. Zhou, Y. Liu, Y. Liu, Y. Wang, J. Xie, L. Sun, M. Liang and P. Jiang, *Energy Technol.*, 2019, **7**, 1800912.
118 Y. N. Jo, S. H. Kang, K. Prasanna, S. W. Eom and C. W. Lee, *Appl. Surf. Sci.*, 2017, **422**, 406–412.
119 P. Liang, J. Yi, X. Liu, K. Wu, Z. Wang, J. Cui, Y. Liu, Y. Wang, Y. Xia and J. Zhang, *Adv. Funct. Mater.*, 2020, **30**, 1908528.
120 K. Hu, X. Guan, R. Lv, G. Li, Z. Hu, L. Ren, A. Wang, X. Liu and J. Luo, *Chem. Eng. J*, 2020, **396**, 125363.
121 C. Deng, X. Xie, J. Han, Y. Tang, J. Gao, C. Liu, X. Shi, J. Zhou and S. Liang, *Adv. Funct. Mater.*, 2020, **30**, 2000599.
122 R. Zhao, Y. Yang, G. Liu, R. Zhu, J. Huang, Z. Chen, Z. Gao, X. Chen and L. Qie, *Adv. Funct. Mater.*, 2021, **31**, 2001867.
123 Z. Zhao, J. Zhao, Z. Hu, J. Li, J. Li, Y. Zhang, C. Wang and G. Cui, *Energy Environ. Sci.*, 2019, **12**, 1938–1949.
124 H. He, H. Tong, X. Song, X. Song and J. Liu, *J. Mater. Chem. A*, 2020, **8**, 7836–7846.
125 M. Schmid, U. Schadeck and M. Willert-Porada, *Surf. Coat. Technol.*, 2017, **310**, 51–58.
126 L. Zhu, H. Zhang, W. Li and H. Liu, *J. Phys. Chem. Solids*, 2009, **70**, 45–54.
127 J. H. Park, C. Choi, J. B. Park, S. Yu and D.-W. Kim, *Adv. Energy Mater.*, 2024, **14**, 2302493.
128 X. Zhu, W. Zhang, Z. Peng, L. Pan, B. Li, Z. Zhang, J. Zhu, W. Meng, L. Dai, L. Wang and Z. He, *Chem. Eng. J*, 2024, **499**, 156521.
129 K. Xia, L. Li, Y. Qiu, J. Weng, S. Shen, M. Chen, Y. Zhuang, Y. Wen, C. Yang, Z. Liu, M. Wu and Z. Zou, *J. Mater. Chem. A*, 2024, **12**, 24175–24187.
130 Q. Han, L. Cai, P. Huang, S. Liu, C. He, Z. Xu, H. Ying and W.-Q. Han, *ACS Appl. Mater. Inter.*, 2023, **15**, 48316–48325.
131 V.-C. Ho, H. Yen Nguyen Thi, T. Huong Pham, H.-G. Jung, J. Ho Kim, J. F. Kim and J. Mun, *Chem. Eng. J.*, 2024, **496**, 153845.
132 X. Sun, X. Lv, M. Zhang, K. Shi, Z. Li, X. Pan, T. Lian, R. Chen, F. Wu and L. Li, *ACS Nano*, 2024, **18**, 8452–8462.
133 H. Yang, J. Wang, P. Zhang, X. Cheng, Q. Guan, J. Dong, B. Chen, L. Jia, J. Zhang, Y. Zhang, Y. Liu and H. Lin, *J. Energy Chem.*, 2025, **100**, 693–701.
134 M. Wei, K. Wang, Y. Zuo, L. Zhong, A. Züttel, Z. Chen, P. Zhang, H. Wang, S. Zhao and P. Pei, *Adv. Funct. Mater.*, 2023, **33**, 2302243.
135 Z. Li, L. Wu, S. Dong, T. Xu, S. Li, Y. An, J. Jiang and X. Zhang, *Adv. Funct. Mater.*, 2021, **31**, 2006495.
136 Q. Hu, J. Hou, Y. Liu, L. Li, Q. Ran, J. Mao, X. Liu, J. Zhao and H. Pang, *Adv. Mater.*, 2023, **35**, 2303336.
137 Y. Wu, Y. Zhang, Y. Ma, J. D. Howe, H. Yang, P. Chen, S. Aluri and N. Liu, *Adv. Energy Mater.*, 2018, **8**, 1802470.
138 Q. Yang, Y. Guo, B. Yan, C. Wang, Z. Liu, Z. Huang, Y. Wang, Y. Li, H. Li, L. Song, J. Fan and C. Zhi, *Adv. Mater.*, 2020, **32**, 2001755.
139 S. Kim, G. Hee Ryu and G. H. An, *Appl. Surf. Sci.*, 2023, **635**, 157634.
140 X. Xu, S. Li, H. Yan, J. Du, S. Yang and B. Li, *Adv. Funct. Mater.*, 2024, **34**, 2308661.

141 M. Liu, W. Yuan, G. Ma, K. Qiu, X. Nie, Y. Liu, S. Shen and N. Zhang, *Angew. Chem.*, 2023, **135**, e202304444.
142 J. J. Conde, F. A. Paloma and A. M. Chaparro, *Appl. Mater. Today*, 2018, **13**, 100–106.
143 D. Han, S. Wu, S. Zhang, Y. Deng, C. Cui, L. Zhang, Y. Long, H. Li, Y. Tao, Z. Weng, Q.-H. Yang and F. Kang, *Small*, 2020, **16**, 2001736.
144 L. Kang, M. Cui, F. Jiang, Y. Gao, H. Luo, J. Liu, W. Liang and C. Zhi, *Adv. Energy Mater.*, 2018, **8**, 1801090.
145 H. J. Liu, C. Y. Yang, M. C. Han, C. Y. Yu, X. Li, Z. Z. Yu and J. Qu, *Angew. Chem.*, 2023, **135**, e202217458.
146 S. Zhou, Y. Wang, H. Lu, Y. Zhang, C. Fu, I. Usman, Z. Liu, M. Feng, G. Fang, X. Cao, S. Liang and A. Pan, *Adv. Funct. Mater.*, 2021, **31**, 2104361.
147 S. Di, X. Nie, G. Ma, W. Yuan, Y. Wang, Y. Liu, S. Shen and N. Zhang, *Energy Storage Mater.*, 2021, **43**, 375–382.
148 R. Wang, S. Xin, D. Chao, Z. Liu, J. Wan, P. Xiong, Q. Luo, K. Hua, J. Hao and C. Zhang, *Adv. Funct. Mater.*, 2022, **32**, 2207751.
149 H. Zhang, Y. Wu, J. Yu, T. Jiang and M. Wu, *Adv. Funct. Mater.*, 2023, **34**, 2301912.
150 F. Ling, L. Wang, F. Liu, M. Ma, S. Zhang, X. Rui, Y. Shao, Y. Yang, S. He, H. Pan, X. Wu, Y. Yao and Y. Yu, *Adv. Mater.*, 2023, **35**, 2208764.
151 X. Zhou, B. Wen, Y. Cai, X. Chen, L. Li, Q. Zhao, S. Chou and F. Li, *Angew. Chem., Int. Ed.*, 2024, **63**, e202402342.
152 Y. Fang, P. Lei, H. Xing, K. Xu, M. Zhu, Z. Fan, K. Qi, Q. Wu and Y. Zhu, *Energy Storage Mater.*, 2022, **53**, 13–21.
153 C. Deng, X. Xie, J. Han, Y. Tang, J. Gao, C. Liu, X. Shi, J. Zhou and S. Liang, *Adv. Funct. Mater.*, 2020, **30**, 2000599.
154 K. Wang, A. Paxson, T. I. Valdez, A. Erlat, P.-C. Lee, S. Yun, P. Khajanji, Z. Zhang, A. C. Kummel and P. Bandaru, *ACS Appl. Mater. Inter.*, 2024, **16**, 35043–35052.
155 J. Hao, B. Li, X. Li, X. Zeng, S. Zhang, F. Yang, S. Liu, D. Li, C. Wu and Z. Guo, *Adv. Mater.*, 2020, **32**, 2003021.
156 R. Guo, X. Liu, F. Xia, Y. Jiang, H. Zhang, M. Huang, C. Niu, J. Wu, Y. Zhao, X. Wang, C. Han and L. Mai, *Adv. Mater.*, 2022, **34**, e2202188.
157 P. Xiao, H. Li, J. Fu, C. Zeng, Y. Zhao, T. Zhai and H. Li, *Energy Environ. Sci.*, 2022, **15**, 1638–1646.
158 K. Ouyang, D. Ma, N. Zhao, Y. Wang, M. Yang, H. Mi, L. Sun, C. He and P. Zhang, *Adv. Funct. Mater.*, 2021, **32**, e202416032.
159 Z. Zhao, R. Wang, C. Peng, W. Chen, T. Wu, B. Hu, W. Weng, Y. Yao, J. Zeng, Z. Chen, P. Liu, Y. Liu, G. Li, J. Guo, H. Lu and Z. Guo, *Nat. Commun.*, 2021, **12**, 6606.
160 M. Fu, H. Yu, S. Huang, Q. Li, B. Qu, L. Zhou, G.-C. Kuang, Y. Chen and L. Chen, *Nano Lett.*, 2023, **23**, 3573–3581.
161 D. Xie, Z. W. Wang, Z. Y. Gu, W. Y. Diao, F. Y. Tao, C. Liu, H. Z. Sun, X. L. Wu, J. W. Wang and J. P. Zhang, *Adv. Funct. Mater.*, 2022, **32**, 2204066.
162 M. Liu, W. Yuan, G. Ma, K. Qiu, X. Nie, Y. Liu, S. Shen and N. Zhang, *Angew. Chem., Int. Ed.*, 2023, **62**, e202304444.
163 B. Lv, Q. Zong, Y. Yu, C. Liu, A. Pan, J. Wang, D. Tao, J. Zhang, Q. Zhang and G. Cao, *Adv. Funct. Mater.*, 2024, **34**, 2316535.
164 J. Yu, C. Chen, F. Shi, R. Li, F. Chen, J. Tang, K. C. Chan and Z.-L. Xu, *Energy Storage Mater.*, 2023, **63**, 102966.
165 D. Xie, Y. Sang, D. H. Wang, W. Y. Diao, F. Y. Tao, C. Liu, J. W. Wang, H. Z. Sun, J. P. Zhang and X. L. Wu, *Angew. Chem., Int. Ed.*, 2023, **62**, e202216934.
166 M. Liu, W. Yuan, X. Qu, X. Ru, X. Li, T. Wang, X. Wang, Y. Wang, Y. Liu and N. Zhang, *Energy Environ. Sci.*, 2024, **17**(24), 9611–9622.
167 A. Mitha, A. Z. Yazdi, M. Ahmed and P. Chen, *ChemElectroChem*, 2018, **5**, 2409–2418.
168 B.-S. Lee, S. Cui, X. Xing, H. Liu, X. Yue, V. Petrova, H.-D. Lim, R. Chen and P. Liu, *ACS Appl. Mater. Inter.*, 2018, **10**, 38928–38935.
169 Y. Gao, Z. Yan, J. L. Gray, X. He, D. Wang, T. Chen, Q. Huang, Y. C. Li, H. Wang, S. H. Kim, T. E. Mallouk and D. Wang, *Nat. Mater.*, 2019, **18**, 384–389.
170 Y. Huang, Z. Li, Z. Pei, Z. Liu, H. Li, M. Zhu, J. Fan, Q. Dai, M. Zhang and L. Dai, *Adv. Energy Mater.*, 2018, **8**, 1802288.
171 Y. Da, F. Zhao, J. Shi and Z. Zhang, *J. Electron. Mater.*, 2020, **49**, 2479–2490.
172 J. Ren, J. Ma, J. Zhang, C. Fu and B. Sun, *J. Alloys Compd.*, 2019, **808**, 151708.
173 B. Li, K. Yang, J. Ma, P. Shi, L. Chen, C. Chen, X. Hong, X. Cheng, M.-C. Tang, Y.-B. He and F. Kang, *Angew. Chem., Int. Ed.*, 2022, **134**, e202212587.
174 G. Lin, Y. Zhou, S. Zanna, A. Seyeux, P. Marcus and J. Swiatowska, *J. Magnes. Alloy*, 2024, **12**, 3646–3660.
175 H. Tian, G. Feng, Q. Wang, Z. Li, W. Zhang, M. Lucero, Z. Feng, Z.-L. Wang, Y. Zhang, C. Zhen, M. Gu, X. Shan and Y. Yang, *Nat. Commun.*, 2022, **13**, 7922.
176 M. Fayette, H. J. Chang, X. Li and D. Reed, *ACS Energy Lett.*, 2022, **7**, 1888–1895.
177 Y. Zhao, S. Guo, M. Chen, B. Lu, X. Zhang, S. Liang and J. Zhou, *Nat. Commun.*, 2023, **14**, 7080.
178 S. B. Wang, Q. Ran, R. Q. Yao, H. Shi, Z. Wen, M. Zhao, X. Y. Lang and Q. Jiang, *Nat. Commun.*, 2020, **11**, 1634.
179 H. Meng, Q. Ran, T.-Y. Dai, H. Shi, S.-P. Zeng, Y.-F. Zhu, Z. Wen, W. Zhang, X.-Y. Lang and W.-T. Zheng, *Nano-Micro Lett.*, 2022, **14**, 128.
180 C. Hu, Z. Yang, Q. Zhang, M. Zhang, T. Wu, C. Xie, H. Wang, Y. Tang and H. Wang, *Angew. Chem., Int. Ed.*, 2024, **63**, e202409096.
181 Y. Nie, H. Chen, J. Wu, R. Nie, L. Yu, L. Liu and J. Xi, *Chem. Eng. J.*, 2024, **498**, 155615.
182 Y. Du, Y. Feng, R. Li, Z. Peng, X. Yao, S. Duan, S. Liu, S. C. Jun, J. Zhu, L. Dai, Q. Yang, L. Wang and Z. He, *Small*, 2024, **20**, 2307848.
183 T. Wang, Y. Zhu, Y. Li, K. Yang, W. Lu, K. Peng and Z. Tian, *Sustainable Energy Fuels*, 2022, **7**, 300–309.
184 X. Liu, J. Xue, J. Cao, Z. Wang and X. Li, *J. Energy Storage*, 2024, **87**, 111503.
185 M. Deng, D. Höche, S. V. Lamaka, D. Snihirova and M. L. Zheludkevich, *J. Power Sources*, 2018, **396**, 109–118.
186 S. K. Kaiser, Z. Chen, D. F. Akl, S. Mitchell and J. Perez-Ramirez, *Chem. Rev.*, 2020, **120**, 11703–11809.

187 Y. N. Jo, K. Prasanna, S. H. Kang, P. R. Ilango, H. S. Kim, S. W. Eom and C. W. Lee, *J. Ind. Eng. Chem.*, 2017, **53**, 247–252.
188 Y. Gouale, S. Khatbi and M. Essahli, *Port. Electrochim. Act.*, 2018, **36**, 89–99.
189 T. W. Cain, C. F. Glover and J. R. Scully, *Electrochim. Acta*, 2019, **297**, 564–575.
190 M. Esmaily, J. E. Svensson, S. Fajardo, N. Birbilis, G. S. Frankel, S. Virtanen, R. Arrabal, S. Thomas and L. G. Johansson, *Prog. Mater. Sci.*, 2017, **89**, 92–193.
191 I.-J. Park, S.-R. Choi and J.-G. Kim, *J. Power Sources*, 2017, **357**, 47–55.
192 L. Wang, R. Wang, Y. Feng, M. Deng and N. Wang, *J. Electrochem. Soc.*, 2017, **164**, A438–A446.
193 A. D. Südholz, N. T. Kirkland, R. G. Buchheit and N. Birbilis, *Electrochem. Solid-State Lett.*, 2011, **14**, C5–C7.
194 X. Xia, J. Nie, C. Davies, W. Tang and N. Birbilis, *Corrosion*, 2015, **71**, 1370–1386.
195 J. Ma, G. Wang, Y. Li, F. Ren and A. A. Volinsky, *Ionics*, 2018, **25**, 2201–2209.
196 R. L. Liu, J. R. Scully, G. Williams and N. Birbilis, *Electrochim. Acta*, 2018, **260**, 184–195.
197 G. Williams, H. A.-L. Dafydd, H. N. McMurray and N. Birbilis, *Electrochim. Acta*, 2016, **219**, 401–411.
198 B. Lenhart, M. Zuraw and W. Mustain, *J. Electrochem. Soc.*, 2023, **170**, 070501.
199 H. Zhang, L. Yang, H. Wang, B. Cui, J. Wang, X. Han and W. Hu, *Adv. Funct. Mater.*, 2024, **34**, 2312469.
200 Z. Yang, C. Hu, Q. Zhang, T. Wu, C. Xie, H. Wang, Y. Tang, X. Ji and H. Wang, *Angew. Chem., Int. Ed.*, 2023, **135**, e202308017.
201 Y. N. Jo, H. S. Kim, K. Prasanna, P. R. Ilango, W. J. Lee, S. W. Eom and C. W. Lee, *Ind. Eng. Chem. Res.*, 2014, **53**, 17370–17375.
202 H. S. Kim, Y. N. Jo, W. J. Lee, K. J. Kim and C. W. Lee, *Electroanal.*, 2015, **27**, 517–523.
203 H. Moghanni-Bavil-Olyaei and J. Arjomandi, *RSC Adv.*, 2015, **5**, 91273–91279.
204 H. Xiong, X. Yin, Y. Yan, Y. Dai, S. Fan, X. Qiao and K. Yu, *J. Mater. Eng. Perform.*, 2016, **25**, 3456–3464.
205 R. N. Mutlu and B. Yazıcı, *J. Solid State Electrochem*, 2018, **23**, 529–541.
206 J. Ma, G. Wang, Y. Li, C. Qin and F. Ren, *J. Mater. Eng. Perform.*, 2019, **28**, 2873–2880.
207 P. Wang, J. Li, Y. Guo, Z. Yang, F. Xia and J. Wang, *Rare Met.*, 2011, **30**, 639–643.
208 J. Xu, Q. Yang, C. Huang, M. S. Javed, M. K. Aslam and C. Chen, *J. Appl. Electrochem.*, 2017, **47**, 767–775.
209 M. A. Deyab, *J. Power Sources*, 2015, **280**, 190–194.
210 N. Wang, X. Chen, H. Wan, B. Zhang, K. Guan, J. Yao, J. Ji, J. Li, Y. Gan, L. Lv, L. Tao, G. Ma, H. Wang, J. Zhang and H. Wang, *Adv. Funct. Mater.*, 2023, **33**, 2300795.
211 M. A. Deyab, *J. Power Sources*, 2015, **292**, 66–71.
212 T. Wei, L. e Mo, Y. Ren, H. Zhang, M. Wang, Y. He, P. Tan, Z. Li, W. Chen and L. Hu, *Energy Storage Mater.*, 2024, **70**, 103525.
213 X. Shen, W. Chen, H. Wang, L. Zhang, B. Hao, C. Zhu, X. Yang, M. Sun, J. Zhou, X. Liu, C. Yan and T. Qian, *Chem. Sci.*, 2024, **15**, 10182–10192.
214 M. C. Han, J. H. Zhang, C. Y. Yu, J. C. Yu, Y. X. Wang, Z. G. Jiang, M. Yao, G. Xie, Z. Z. Yu and J. Qu, *Angew. Chem.*, 2024, **136**, e202403695.
215 J. Huang, Y. Zhong, H. Fu, Y. Zhao, S. Li, Y. Xie, H. Zhang, B. Lu, L. Chen and S. Liang, *Adv. Mater.*, 2024, **36**, 2406257.
216 W. Xie, K. Zhu, W. Jiang, H. Yang, M. Ma, L. Zhao and W. Yang, *Acs Nano*, 2024, **18**, 21184–21197.
217 Y. Qiang, S. Zhang, L. Guo, S. Xu, L. Feng, I. B. Obot and S. Chen, *J. Cleaner Prod.*, 2017, **152**, 17–25.
218 D. Gelman, H. Drezner, A. Kraytsberg, D. Starosvetsky and Y. Ein-Eli, *J. Solid State Electrochem.*, 2018, **22**, 2217–2226.
219 M. Abdallah, A. Y. El-Etre and M. F. Moustafa, *Port. Electrochim. Act.*, 2009, **27**, 615–630.
220 H. Zhou, Q. Huang, M. Liang, D. Lv, M. Xu, H. Li and W. Li, *Mater. Chem. Phys.*, 2011, **128**, 214–219.
221 Y. Li, Z. Hu and J. Kan, *Metals*, 2016, **6**, 176.
222 F. Yang, J. A. Yuwono, J. Hao, J. Long, L. Yuan, Y. Wang, S. Liu, Y. Fan, S. Zhao, K. Davey and Z. Guo, *Adv. Mater.*, 2022, **34**, e2206754.
223 M. Kim, S. J. Shin, J. Lee, Y. Park, Y. Kim, H. Kim and J. W. Choi, *Angew. Chem., Int. Ed.*, 2022, **134**, e202211589.
224 T. Xiao, J.-L. Yang, B. Zhang, J. Wu, J. Li, W. Mai and H. J. Fan, *Angew. Chem., Int. Ed.*, 2024, **63**, e202318470.
225 X. Wang, Y. Ying, S. Chen, Q. Meng, H. Huang and L. Ma, *Nano Energy*, 2024, **119**, 109099.
226 Z. Shi, M. Li, X. Fu, Y. Zhang, S. Jiao and Y. Zhao, *Adv. Funct. Mater.*, 2024, **34**, 2316427.
227 D. Li, Y. Zhong, X. Xu, D. Zhou, Y. Tang, L. Wang, S. Liang, B. Lu, Y. Liu and J. Zhou, *Energy Environ. Sci.*, 2024, **17**, 8855–8865.
228 T. Wu, C. Hu, Q. Zhang, Z. Yang, G. Jin, Y. Li, Y. Tang, H. Li and H. Wang, *Adv. Funct. Mater.*, 2024, 2315716.
229 X. Feng, P. Li, J. Yin, Z. Gan, Y. Gao, M. Li, Y. Cheng, X. Xu, Y. Su and S. Ding, *ACS Energy Lett.*, 2023, **8**, 1192–1200.
230 Y. Nie, J. Gao, E. Wang, L. Jiang, L. An and X. Wang, *Electrochim. Acta*, 2017, **248**, 478–485.
231 P. Ruan, X. Chen, L. Qin, Y. Tang, B. Lu, Z. Zeng, S. Liang and J. Zhou, *Adv. Mater.*, 2023, **35**, 2300577.
232 K. Liu, P. He, H. Bai, J. Chen, F. Dong, S. Wang, M. He and S. Yuan, *Mater. Chem. Phys.*, 2017, **199**, 73–78.
233 Z. Liu, Y. Zhao, G.-C. Han, J. Liu, Q. He and C. Chen, *Ionics*, 2016, **22**, 2391–2397.
234 Y. Ein-Eli, M. Auinat and D. Starosvetsky, *J. Power Sources*, 2003, **114**, 330–337.
235 M. Liang, H. Zhou, Q. Huang, S. Hu and W. Li, *J. Appl. Electrochem.*, 2011, **41**, 991–997.
236 M.-H. Lin, C.-J. Huang, P.-H. Cheng, J.-H. Cheng and C.-C. Wang, *J. Mater. Chem. A*, 2020, **8**, 20637–20649.
237 S. Hosseini, W. Lao-Atiman, S. J. Han, A. Arpornwichanop, T. Yonezawa and S. Kheawhom, *Sci. Rep.*, 2018, **8**, 14909.
238 Y. Xiao, J. Shi, F. Zhao, Z. Zhang and W. He, *J. Electrochem. Soc.*, 2018, **165**, A47–A54.
239 R. Sun, D. Han, C. Cui, Z. Han, X. Guo, B. Zhang, Y. Guo, Y. Liu, Z. Weng and Q.-H. Yang, *Angew. Chem., Int. Ed.*, 2023, **62**, e202303557.
240 Y. Shang, V. Kundi, I. Pal, H. N. Kim, H. Zhong, P. Kumar and D. Kundu, *Adv. Mater.*, 2024, **36**, 2309212.

241 C. Yang, Z. Zhang, Z. Tian, K. Zhang, J. Li and Y. Lai, *J. Electrochem. Soc.*, 2016, **163**, A1836–A1840.
242 H. Liu, Z. Xin, B. Cao, Z. Xu, B. Xu, Q. Zhu, J.-L. Yang, B. Zhang and H. J. Fan, *Adv. Funct. Mater.*, 2024, **34**, 2309840.
243 F. Wang, W. Liang, X. Liu, T. Yin, Z. Chen, Z. Yan, F. Li, W. Liu, J. Lu, C. Yang and Q.-H. Yang, *Adv. Energy Mater.*, 2024, **14**, 2400110.
244 Z. Liang, C. Li, D. Zuo, L. Zeng, T. Ling, J. Han and J. Wan, *Energy Storage Mater.*, 2023, **63**, 102980.
245 X. Gu, Y. Du, X. Ren, F. Ma, X. Zhang, M. Li, Q. Wang, L. Zhang, C. Lai and S. Zhang, *Adv. Funct. Mater.*, 2024, **34**, 2316541.
246 D.-Q. Cai, H. Cheng, J.-L. Yang, H. Liu, T. Xiao, X. Liu, M. Chen and H. J. Fan, *Energy Environ. Sci.*, 2024, **17**, 8349–8359.
247 S. Mehta, S. Kaur, M. Singh, M. Kumar, K. Kumar, S. K. Meena and T. C. Nagaiah, *Adv. Energy Mater.*, 2024, **14**, 2401515.
248 X. Xiao, X. Ye, Z. Wu, X. Wu, J. Yu, L. Gu and S. Liu, *Adv. Mater.*, 2024, **36**, 2408706.
249 R. Chen, W. Zhang, Q. Huang, C. Guan, W. Zong, Y. Dai, Z. Du, Z. Zhang, J. Li, F. Guo, X. Gao, H. Dong, J. Zhu, X. Wang and G. He, *Nano-Micro Lett.*, 2023, **15**, 81.
250 M. Kim, S.-J. Shin, J. Lee, Y. Park, Y. Kim, H. Kim and J. W. Choi, *Angew. Chem., Int. Ed.*, 2022, **61**, e202211589.
251 Y. Lin, Z. Mai, H. Liang, Y. Li, G. Yang and C. Wang, *Energy Environ. Sci.*, 2023, **16**, 687–697.
252 R. Han, T. Jiang, Z. Wang, R. Xue, X. Liu, Y. Tang, Z. Qi and Y. Ma, *Adv. Funct. Mater.*, 2024, 2412255.
253 J. Zhang, Y. Liu, Y. Wang, Z. Zhu and Z. Yang, *Adv. Funct. Mater.*, 2024, **34**, 2401889.
254 C. Hou, S. Chen, Z. Wang, G. Wang and G. Dong, *Mater. Corros.*, 2020, **71**, 1480–1487.
255 M. A. Deyab, *J. Power Sources*, 2019, **412**, 520–526.
256 M. A. Deyab, *Electrochim. Acta*, 2017, **244**, 178–183.
257 J. Ma, W. Li, G. Wang, Y. Li, F. Ren and Y. Xiong, *J. Electrochem. Soc.*, 2018, **165**, A266–A272.
258 D. Gelman, I. Lasman, S. Elfimchev, D. Starosvetsky and Y. Ein-Eli, *J. Power Sources*, 2015, **285**, 100–108.
259 E. Grishina, D. Gelman, S. Belopukhov, D. Starosvetsky, A. Groysman and Y. Ein-Eli, *ChemSusChem*, 2016, **9**, 2103–2111.
260 Y. Liu, H. Zhang, Y. Liu, J. Li and W. Li, *J. Power Sources*, 2019, **434**, 226723.
261 Q. X. Kang, Y. Wang and X. Y. Zhang, *J. Alloys Compd.*, 2019, **774**, 1069–1080.
262 C. Zhu, H. Yang, A. Wu, D. Zhang, L. Gao and T. Lin, *J. Power Sources*, 2019, **432**, 55–64.
263 M. A. Deyab, *J. Power Sources*, 2016, **325**, 98–103.
264 Y. Li, J. Ma, G. Wang, F. Ren, Y. Zhu and Y. Song, *J. Electrochem. Soc.*, 2018, **165**, A1713–A1717.
265 Y. Zhao, G. Huang, C. Zhang, C. Peng and F. Pan, *Mater. Chem. Phys.*, 2018, **218**, 256–261.
266 B. Liu, T. Lv, A. Zhou, X. Zhu, Z. Lin, T. Lin and L. Suo, *Nat. Commun.*, 2024, **15**, 2922.
267 S. Yang, Q. Wu, Y. Li, F. Luo, J. Zhang, K. Chen, Y. You, J. Huang, H. Xie and Y. Chen, *Angew. Chem., Int. Ed.*, 2024, **136**, e202409160.
268 X. Wang, B. Wang, P. Lei, X. Wang, L. Zhou, J. Zhang, J. Zhang and J. Cheng, *Energy Environ. Sci.*, 2024, **17**, 6640–6655.
269 Q. Fu, S. Hao, X. Zhang, H. Zhao, F. Xu and J. Yang, *Energy Environ. Sci.*, 2023, **16**, 1291–1311.
270 Y. Zhao, Z. Chen, X. Gao, H. Dong, X. Zhao, G. He and H. Yang, *Angew. Chem., Int. Ed.*, 2024, e202415251.
271 Y. Cui, W. Chen, W. Xin, H. Ling, Y. Hu, Z. Zhang, X. He, Y. Zhao, X.-Y. Kong, L. Wen and L. Jiang, *Adv. Mater.*, 2024, **36**, 2308639.
272 J.-L. Yang, T. Xiao, T. Xiao, J. Li, Z. Yu, K. Liu, P. Yang and H. J. Fan, *Adv. Mater.*, 2024, **36**, 2313610.
273 T. Qiu, T. Wang, W. Tang, Y. Li, Y. Li, X. Lang, Q. Jiang and H. Tan, *Angew. Chem.*, 2023, **135**, e202312020.
274 L. Ma, S. Chen, D. Wang, Q. Yang, F. Mo, G. Liang, N. Li, H. Zhang, J. A. Zapien and C. Zhi, *Adv. Energy Mater.*, 2019, **9**, 1803046.
275 F. Mo, G. Liang, D. Wang, Z. Tang and C. Zhi, *EcoMat*, 2019, **1**, e12008.
276 L. Han, H. L. Huang, J. F. Li, X. L. Zhang, Z. L. Yang, M. Xu and L. K. Pan, *J. Mater. Chem. A*, 2020, **8**, 15042–15050.
277 K. T. Leng, G. J. Li, J. J. Guo, X. Y. Zhang, A. X. Wang, X. J. Liu and J. Y. Luo, *Adv. Funct. Mater.*, 2020, **30**, 10.
278 Z. Liu, D. Wang, Z. Tang, G. Liang, Q. Yang, H. Li, L. Ma, F. Mo and C. Zhi, *Energy Storage Mater.*, 2019, **23**, 636–645.
279 H. Li, C. Han, Y. Huang, Y. Huang, M. Zhu, Z. Pei, Q. Xue, Z. Wang, Z. Liu, Z. Tang, Y. Wang, F. Kang, B. Li and C. Zhi, *Energy Environ. Sci.*, 2018, **11**, 941–951.
280 Z. Shen, Y. Liu, Z. Li, Z. Tang, J. Pu, L. Luo, Y. Ji, J. Xie, Z. Shu and Y. Yao, *Adv. Funct. Mater.*, 2024, DOI: **10.1002/adfm.202406620**.
281 F. Mo, Z. Chen, G. Liang, D. Wang, Y. Zhao, H. Li, B. Dong and C. Zhi, *Adv. Energy Mater.*, 2020, **10**, 2000035.
282 J. Zhao, K. K. Sonigara, J. Li, J. Zhang and L. Chen, *Angew. Chem., Int. Ed.*, 2017, **56**, 7979–7983.
283 Q. Han, X. Chi, S. Zhang, Y. Liu, B. Zhou, J. Yang and Y. Liu, *J. Mater. Chem. A*, 2018, **6**, 23046–23054.
284 Z. Yang, Q. Zhang, T. Wu, Q. Li, J. Shi, J. Gan, S. Xiang, H. Wang, C. Hu and Y. Tang, *Angew. Chem., Int. Ed.*, 2024, **63**, e202317457.
285 S. Zhang, N. Yu, S. Zeng, S. Zhou, M. Chen, J. Di and Q. Li, *J. Mater. Chem. A*, 2018, **6**, 12237–12243.
286 S. Wu, S. Hu, Q. Zhang, D. Sun, P. Wu, Y. Tang and H. Wang, *Energy Storage Mater.*, 2020, **31**, 310–317.
287 W. Xiong, T. K. A. Hoang, D. Yang, Y. Liu, M. Ahmed, J. Xu, X. Qiu and P. Chen, *J. Energy Storage*, 2019, **26**, 100920.
288 T. K. A. Hoang, M. Acton, H. T. H. Chen, Y. Huang, T. N. L. Doan and P. Chen, *Mater. Today Energy*, 2017, **4**, 34–40.
289 T. K. A. Hoang, T. N. L. Doan, J. H. Cho, J. Y. J. Su, C. Lee, C. Lu and P. Chen, *ChemSusChem*, 2017, **10**, 2816–2822.
290 N. Dubouis, P. Lemaire, B. Mirvaux, E. Salager, M. Deschamps and A. Grimaud, *Energy Environ. Sci.*, 2018, **11**, 3491–3499.
291 L. Suo, O. Borodin, T. Gao, M. Olguin, J. Ho, X. Fan, C. Luo, C. Wang and K. Xu, *Science*, 2015, **350**, 938–943.

292 M. R. Lukatskaya, J. I. Feldblyum, D. G. Mackanic, F. Lissel, D. L. Michels, Y. Cui and Z. Bao, *Energy Environ. Sci.*, 2018, **11**, 2876–2883.
293 S. Liu, H. Lin, Q. Song, J. Zhu and C. Zhu, *Energy Environ. Mater.*, 2023, **6**, e12405.
294 X. Zhou, B. Wen, Y. Cai, X. Chen, L. Li, Q. Zhao, S.-L. Chou and F. Li, *Angew. Chem., Int. Ed.*, 2024, **63**, e202402342.
295 L. Fan, H. Lu, J. Leng, Z. Sun and C. Chen, *J. Power Sources*, 2015, **299**, 66–69.
296 N. Wang, Y. Mu, W. Xiong, J. Zhang, Q. Li and Z. Shi, *Corros. Sci.*, 2018, **144**, 107–126.
297 B. J. Hopkins, Y. Shao-Horn and D. P. Hart, *Science*, 2018, **362**, 658–661.
298 P. Xie, M. Z. Rong and M. Q. Zhang, *Angew. Chem., Int. Ed.*, 2016, **55**, 1805–1809.
299 D. Raptis, A. K. Seferlis, V. Mylona, C. Politis and P. Lianos, *Int. J. Hydrogen Energy*, 2019, **44**, 1359–1365.
300 C. Kim, J. Kim, S. Joo, Y. Yang, J. Shin, M. Liu, J. Cho and G. Kim, *Angew. Chem., Int. Ed.*, 2019, **58**, 9506–9511.
301 A. Z. Zhuk, A. E. Sheindlin, B. V. Kleymenov, E. I. Shkolnikov and M. Y. Lopatin, *J. Power Sources*, 2006, **157**, 921–926.
302 T. Bellezze, G. Giuliani and G. Roventi, *Corros. Sci.*, 2018, **130**, 113–125.
303 S. Karimi, I. Taji, T. Hajilou, S. Palencsár, A. Dugstad, A. Barnoush, K. Verbeken, T. Depover and R. Johnsen, *Corros. Sci.*, 2023, **214**, 111031.
304 R. Meng, H. Li, Z. Lu, C. Zhang, Z. Wang, Y. Liu, W. Wang, G. Ling, F. Kang and Q. H. Yang, *Adv. Mater.*, 2022, **34**, e2200677.
305 H. Tian, J. L. Yang, Y. Deng, W. Tang, R. Liu, C. Xu, P. Han and H. J. Fan, *Adv. Energy Mater.*, 2023, **13**, 2202603.
306 M. P. Gomes, I. Costa, N. Pébère, J. L. Rossi, B. Tribollet and V. Vivier, *Electrochim. Acta*, 2019, **306**, 61–70.
307 G. L. de Gouveia, J. E. Spinelli and G. Y. Koga, *Corros. Sci.*, 2024, **237**, 112326.
308 R. De Motte, E. Basilico, R. Mingant, J. Kittel, F. Ropital, P. Combrade, S. Necib, V. Deydier, D. Crusset and S. Marcelin, *Corros. Sci.*, 2020, **172**, 108666.
309 M. Diaz-Ramos, V. Roche, R. Song, H. Fan, C. Bureau and J. C. Lepretre, *Corros. Sci.*, 2023, **213**, 110932.
310 J. M. Ferreira, Jr., M. Oliveira, G. F. Trindade, L. C. L. Santos, C. R. Tomachuk and M. A. Baker, *Corros. Sci.*, 2018, **137**, 13–32.
311 S. M. Hoseinieh, A. M. Homborg, T. Shahrabi, J. M. C. Mol and B. Ramezanzadeh, *Electrochim. Acta*, 2016, **217**, 226–241.
312 M. Sharifuzzaman, M. A. Zahed, M. S. Reza, M. Asaduzzaman, S. Jeong, H. Song, D. K. Kim, S. Zhang and J. Y. Park, *Adv. Funct. Mater.*, 2023, **33**, 2208894.
313 J. Chen, J. He and L. Li, *Corros. Sci.*, 2022, **205**, 110425.
314 J. H. Arellano-Perez, R. F. Escobar-Jimenez, D. Granados-Lieberma, J. F. Gomez-Aguilar, J. Uruchurtu-Chavarin and V. M. Alvarado-Martinez, *J. Electroanal. Chem.*, 2019, **848**, 113249.
315 C. Ma, S. Song, Z. Gao, J. Wang, W. Hu, Y. Behnamian and D.-H. Xia, *Corros. Eng. Sci. Technol.*, 2017, **52**, 432–440.
316 I. B. Obot, I. B. Onyeachu, A. Zeino and S. A. Umoren, *J. Adhes. Sci. Technol.*, 2019, **33**, 1453–1496.
317 O. Ramos-Negrón, R. Escobar-Jiménez, J. Arellano-Pérez, J. Uruchurtu-Chavarín, J. Gómez-Aguilar and M. Lucio-García, *J. Electroanal. Chem.*, 2019, **855**, 113597.
318 A. Legat and C. Zevnik, *Corros. Sci.*, 1993, **35**, 1661–1666.
319 C. Ma, Z. Wang, Y. Behnamian, Z. Gao, Z. Wu, Z. Qin and D.-H. Xia, *Measurement*, 2019, **138**, 54–79.
320 D. H. Xia, S. Z. Song and Y. Behnamian, *Corros. Eng. Sci. Technol.*, 2016, **51**, 527–544.
321 A. Rana, K. Roy, J. N. Heil, J. H. Nguyen, C. Renault, B. M. Tackett and J. E. Dick, *Adv. Energy Mater.*, 2024, **14**, 2402521.
322 M. Peng, X. Tang, K. Xiao, T. Hu, K. Yuan and Y. Chen, *Angew. Chem., Int. Ed.*, 2023, **62**, e202302701.
323 J. Fu, H. Wang, P. Xiao, C. Zeng, Q. Sun and H. Li, *Energy Storage Mater.*, 2022, **48**, 191–196.
324 I. Serebrennikova, S. Lee and H. S. White, *Faraday Discuss.*, 2002, **121**, 199–210.
325 H. Shi, Z. Tian, T. Hu, F. Liu, E.-H. Han, M. Taryba and S. V. Lamaka, *Corros. Sci.*, 2014, **88**, 178–186.
326 M. Li, Y. Wang, B. Blount, E. Gordon, J. A. Muñoz-Castañeda, Z. Ye and H. Ren, *Nano Lett.*, 2022, **22**, 6313–6319.
327 R. M. Souto, Y. González-García, J. Izquierdo and S. González, *Corros. Sci.*, 2010, **52**, 748–753.
328 N. Payne, L. Stephens and J. Mauzeroll, *Corrosion*, 2017, **73**, 759–780.
329 C. S. Santos, A. Botz, A. S. Bandarenka, E. Ventosa and W. Schuhmann, *Angew. Chem., Int. Ed.*, 2022, **61**, e202202744.
330 A. Mishra, M. Zorigt, D. O. Kim and J. Rodriguez-Lopez, *J. Am. Chem. Soc.*, 2024, **146**, 8847–8851.
331 I. Traxler, T. D. Singewald, G. Schimo-Aichhorn, S. Hild and M. Valtiner, *Corros. Rev.*, 2022, **40**, 515–542.
332 U. M. Tefashe, M. E. Snowden, P. D. Ducharme, M. Danaie, G. A. Botton and J. Mauzeroll, *J. Electroanal. Chem.*, 2014, **720**, 121–127.
333 P. Dauphin-Ducharme, R. Matthew Asmussen, U. M. Tefashe, M. Danaie, W. Jeffrey Binns, P. Jakupi, G. A. Botton, D. W. Shoesmith and J. Mauzeroll, *J. Electrochem. Soc.*, 2014, **161**, C557–C564.
334 A. Asserghine, M. Medvidović-Kosanović, A. Stanković, L. Nagy, R. M. Souto and G. Nagy, *Sens. Actuators, B*, 2020, **321**, 128610.
335 M. Zhang, H. Hua, P. Dai, Z. He, L. Han, P. Tang, J. Yang, P. Lin, Y. Zhang, D. Zhan, J. Chen, Y. Qiao, C. C. Li, J. Zhao and Y. Yang, *Adv. Mater.*, 2023, **35**, 2208630.
336 J. Izquierdo, L. Nagy, Á. Varga, J. J. Santana, G. Nagy and R. M. Souto, *Electrochim. Acta*, 2011, **56**, 8846–8850.
337 I. Liberman, R. Ifraemov, R. Shimoni and I. Hod, *Adv. Funct. Mater.*, 2022, **32**, 2112517.
338 A. Mishra, M. Zorigt, D. O. Kim and J. Rodríguez-López, *J. Am. Chem. Soc.*, 2024, **146**, 8847–8851.
339 Y. Gan, B. Tan, Q. Hu, S. Zhang and W. Li, *Corros. Sci.*, 2022, **208**, 110619.
340 X. Li, P. Ye, A. Dou, Z. Jiang, A. Naveed, Y. Zhou, M. Su, P. Zhang and Y. Liu, *J. Energy Storage*, 2024, **76**, 109874.

341 Y. Yu, Y. X. Zuo, Z. H. Zhang, L. Wu, C. L. Ning and C. C. Zuo, *Coatings*, 2019, **9**, 692.
342 X. Luo, R. Wang, L. Zhang, Z. Liu, H. Li, J. Mao, S. Zhang, J. Hao, T. Zhou and C. Zhang, *ACS Nano*, 2024, **18**, 12981–12993.
343 X. Zhang, R. Wang, Z. Liu, Q. Ma, H. Li, Y. Liu, J. Hao, S. Zhang, J. Mao and C. Zhang, *Adv. Energy Mater.*, 2024, **14**, 2400314.
344 Y. Meng, L. Liu, D. Zhang, C. Dong, Y. Yan, A. A. Volinsky and L. N. Wang, *Bioact. Mater.*, 2019, **4**, 87–96.
345 J. A. Yuwono, N. Birbilis, R. Liu, Q. Ou, Q. Bao and N. V. Medhekar, *J. Electrochem. Soc.*, 2017, **164**, C918–C929.
346 X. Ni, J. Zhou, H. Ji, Y. Chen, H. Yu, Y. Zheng, T. Qian, M. Wang, L. Chen and C. Yan, *Adv. Funct. Mater.*, 2023, **33**, 2302293.
347 F. Ling, L. Wang, F. Liu, M. Ma, S. Zhang, X. Rui, Y. Shao, Y. Yang, S. He, H. Pan, X. Wu, Y. Yao and Y. Yu, *Adv. Mater.*, 2023, **35**, 2208764.
348 S.-J. Zhang, J. Hao, H. Li, P.-F. Zhang, Z.-W. Yin, Y.-Y. Li, B. Zhang, Z. Lin and S.-Z. Qiao, *Adv. Mater.*, 2022, **34**, 2201716.
349 Q. Shi, L. J. Rendek, W.-B. Cai and D. A. Scherson, *Electrochem. Solid-State Lett.*, 2003, **6**, E35.
350 C. Pan, L. Liu, Y. Li and F. Wang, *Corros. Sci.*, 2013, **73**, 32–43.
351 J. Cheng, J. Pan, T. Wang and X. Lu, *Corros. Sci.*, 2018, **137**, 184–193.
352 F. Zhang, J. Pan and C. Lin, *Corros. Sci.*, 2009, **51**, 2130–2138.
353 A. Almalla, O. Ozcan and J. Witt, *Adv. Eng. Mater.*, 2022, **24**, 2101342.
354 L. Wei and W. Qin, *Corros. Sci.*, 2022, **206**, 110525.
355 F. A. Martin, C. Bataillon and J. Cousty, *Corros. Sci.*, 2008, **50**, 84–92.
356 P. Yi, C. Dong, K. Xiao and X. Li, *Corros. Sci.*, 2021, **181**, 109244.
357 S. Montecinos and S. N. Simison, *Appl. Surf. Sci.*, 2011, **257**, 7732–7738.
358 X. Zhou, Q. Zhang, Z. Hao, Y. Ma, O. A. Drozhzhin and F. Li, *ACS Appl. Mater. Inter.*, 2021, **13**, 53227–53234.
359 A. Kreta, M. Gaberšček and I. Muševič, *J. Mater. Res.*, 2021, **36**, 79–93.
360 H. Wang, B. Brown, S. Nesic and A. Pailleret, *NACE CORROSION*, 2021, D091S033R003.
361 Y. Shi, L. Collins, N. Balke, P. K. Liaw and B. Yang, *Appl. Surf. Sci.*, 2018, **439**, 533–544.
362 S. D. Zhang, Z. W. Liu, Z. M. Wang and J. Q. Wang, *Corros. Sci.*, 2014, **83**, 111–123.
363 Y.-J. Cho, I.-J. Park, H.-J. Lee and J.-G. Kim, *J. Power Sources*, 2015, **277**, 370–378.
364 Y. Zhong, Z. Cheng, H. Zhang, J. Li, D. Liu, Y. Liao, J. Meng, Y. Shen and Y. Huang, *Nano Energy*, 2022, **98**, 107220.
365 E. Faegh, S. Shrestha, X. Zhao and W. E. Mustain, *J. Appl. Electrochem.*, 2019, **49**, 895–907.
366 Y. Huang, Q. Gu, Z. Guo, W. Liu, Z. Chang, Y. Liu, F. Kang, L. Dong and C. Xu, *Energy Storage Mater.*, 2022, **46**, 243–251.
367 X. Wei, D. Desai, G. G. Yadav, D. E. Turney, A. Couzis and S. Banerjee, *Electrochim. Acta*, 2016, **212**, 603–613.
368 A. Rana, A. Thakare, N. Kumar, B. Mukherjee, A. Torris, B. Das, S. Ogale and A. Banerjee, *ACS Appl. Mater. Inter.*, 2023, **15**, 23093–23103.
369 J. Scharf, L. Yin, C. Redquest, R. Liu, X. L. Quinn, J. Ortega, X. Wei, J. Wang, J.-M. Doux and Y. S. Meng, *Adv. Energy Mater.*, 2021, **11**, 2101327.
370 J. Wang, J. Peng, W. Huang, H. Liang, Y. Hao, J. Li, H. Chu, H. Wei, Y. Zhang and J. Liu, *Adv. Funct. Mater.*, 2024, **34**, 2316083.

